UNIVERSIDADE FEDERAL DO ESPÍRITO SANTO

CENTRO TECNOLÓGICO

PROGRAMA DE PÓS-GRADUAÇÃO EM ENGENHARIA AMBIENTAL

IZABELE VENTUROTT FERREIRA TONIATO

Fluid flow features inside an enclosure device used for measuring volatile emissions from solid and liquid surfaces

Vitória

2020

Izabele Venturott Ferreira Toniato

Fluid flow features inside an enclosure device used for measuring volatile emissions from solid and liquid surfaces

Dissertation submitted to Programa de Pós-Graduação em Engenharia Ambiental, Centro Tecnológico, Universidade Federal do Espírito Santo, for the degree of Master of Science in Environmental Engineering. Supervisor: Prof. Jane Méri Santos. Co-supervisors: Prof. Richard M. Stuetz and Ramon Silva Martins.

Vitória

2020

Ficha catalográfica disponibilizada pelo Sistema Integrado de Bibliotecas - SIBI/UFES e elaborada pelo autor

---

Toniato, Izabele Venturott Ferreira, 1992-
T663f Fluid flow features inside an enclosure device used for measuring volatile emissions from solid and liquid surfaces / Izabele Venturott Ferreira Toniato. - 2020.
116 f. : il.

Orientadora: Jane Méri Santos.
Coorientadores: Richard M. Stuetz, Ramon Silva Martins.
Dissertação (Mestrado em Engenharia Ambiental) - Universidade Federal do Espírito Santo, Centro Tecnológico.

1. Ar - Poluição. 2. Controle de odor. 3. Fluidodinâmica computacional. 4. Modelagem computacional. I. Santos, Jane Méri. II. Stuetz, Richard M.. III. Martins, Ramon Silva. IV. Universidade Federal do Espírito Santo. Centro Tecnológico. V. Título.

CDU: 628

Acknowledgements

It has been a long road to get here and I would like to thank the people that has shared this path with me.

First, I would like to express my gratitude for my family, for all the support and encouragement. You were fundamental in my accomplishment.

I would like to thank my supervisor, Professor Jane Meri Santos, and my co-supervisors, Professor Richard M. Stuetz and Professor Ramon Silva Martins for the valuable guidance, the patience and for sharing their knowledge with me.

I also would like to thank Professor Bruno Furieri for always helping me with my endless doubts.

I am forever grateful for the friends that have shared the laboratory with me. Thank you for all the help and company.

I would like to acknowledge the Brazilian Government Agency CNPq for the funding support.

I would like to dedicate this work to Elvis, that has never left my side. Thank you for your love, understanding, unconditional support, encouragement and patience. I could not have done it without you.

Abstract

Odorous gases generated by domestic and industrial wastewater treatment plants and other industrial processes can cause discomfort in the population living nearby and may generate complaints to the local environmental agency. Some of the odorous sources in these facilities are characterized as passive areas sources and their emission rate can be measured by portable wind tunnels. It is a bottom opened devices positioned over an odor-emitting surface. However, there is not a universally adopted wind tunnel model yet. The objective of this work consists in analyzing the air flow patterns inside the tunnel positioned over different rough surfaces and to verify if it reproduces the friction velocity encountered in atmospheric flows. The fluid flow was modeled using the fundamental equations of mass and momentum conservation. These equations were solved by means of a numerical solution based on the finite volume method using an unstructured mesh formed by tetrahedral and prismatic volume elements.

The results showed that there are recirculation zones inside the tunnel and an acceleration after the inlet curve. The velocity vectors showed a deceleration in the flow for surfaces with higher roughness value and the turbulence intensity was lower for the same surfaces. The highest values of the friction velocity at the emitting surface were found at the entrance of the tunnel's main section and were decreasing as the flow develops in the main flow direction. The mean friction velocity varied between $0.14\ m\ s^{-1}$ (for the lowest roughness) and $0.23\ m\ s^{-1}$ (for the highest roughness). Different inlet velocities were also analyzed for smooth surface and the mean friction velocity varied between $0.06\ m\ s^{-1}$ (for the lowest inlet velocity) and $0.14\ m\ s^{-1}$ (for the highest inlet velocity). These values are in agreement with the friction velocity values found in atmospheric flows for some ranges of wind flow velocity.

Keywords: odor, portable wind tunnel, emission measurement, friction velocity, passive area sources.

Resumo

O odor gerado por estações de tratamento de esgoto doméstico e industrial, e outros processos industriais, podem causar desconforto na população que vive ao seu redor e reclamações à agência ambiental local. Algumas das fontes de odor nesses locais são caracterizadas como fontes de área passivas e suas taxas de emissão podem ser medidas por túneis de vento portáteis. É um equipamento com a parte inferior aberta que é posicionado sobre uma superfície emissora de odor. Entretanto, ainda não há um modelo de túnel de vento universalmente adotado. O objetivo desse trabalho consiste em analisar o padrão do escoamento do ar no interior do túnel posicionado sobre superfícies com diferentes rugosidades e verificar se ele reproduz a velocidade de fricção encontrada em escoamentos atmosféricos. O escoamento foi modelado usando as equações fundamentais de conservação de massa e momento. Essas equações foram resolvidas através de uma solução numérica baseada no método de volumes finitos usando uma malha não estruturada formada por elementos de volume tetraédricos e prismáticos.

Os resultados mostraram que existem zonas de recirculação dentro do túnel e uma aceleração após a curva de entrada. Os vetores de velocidade mostraram uma desaceleração no escoamento para superfícies com maiores valores de rugosidade e a intensidade turbulenta foi menor para as mesmas superfícies. Os maiores valores da velocidade de fricção na superfície emissora foram encontrados na entrada da seção principal do túnel e foram diminuindo à medida que o escoamento se desenvolve na direção principal do escoamento. A velocidade de fricção média variou entre $0.14\ m\ s^{-1}$ (para a menor rugosidade) e $0.23\ m\ s^{-1}$ (para a maior rugosidade). Diferentes velocidades de entrada no túnel também foram analisadas para a superfície lisa e a velocidade de fricção média variou entre $0.06\ m\ s^{-1}$ (para a menor velocidade de entrada) e $0.14\ m\ s^{-1}$ (para a maior velocidade de entrada). Esses valores estão de acordo com os valores de velocidade de fricção encontrados em escoamentos atmosféricos para alguns intervalos de velocidade do vento.

Palavras-chave: odor, túnel de vento portátil, monitoramento de emissões, velocidade de fricção, emissão em superfícies passivas.

List of Figures

List of Tables

List of Symbols

Acronyms

ABL	Atmospheric Boundary Layer
NQualiAr	Núcleo de Estudos da Qualidade do Ar
RANS	Reynolds Averaged Navier-Stokes
RMS	Root Mean Square
SST	Shear-Stress Transport
TKE	Turbulent Kinetic Energy
TREIM	Two Resistance Exchange Interface Model
UNSW	University of New South Wales

Roman symbols

C_μ	Empirical constant in the $K-\varepsilon$ model
C_A	Concentration of substance A ($kg\ m^{-3}$)
C_G	Concentration of the compound in the gaseous phase ($kg\ m^{-3}$)
$C_{G,0}$	Concentration of the compound in the interior of the gaseous phase ($kg\ m^{-3}$)
$C_{G,i}$	Concentration of the compound in the gaseous interface ($kg\ m^{-3}$)
$C_{G,\infty}$	Concentration of the compound distant from the interface for the gaseous phase ($kg\ m^{-3}$)
C_L	Concentration of the compound in the liquid phase ($kg\ m^{-3}$)
$C_{L,0}$	Concentration of the compound in the interior of the liquid phase ($kg\ m^{-3}$)
$C_{L,i}$	Concentration of the compound in the liquid interface ($kg\ m^{-3}$)
$C_{L,\infty}$	Concentration of the compound distant from the interface for the liquid phase ($kg\ m^{-3}$)
C_s	Roughness constant (dimensionless)
d	Distance to the nearest wall (m)
d_G	Thickness of the gaseous film (m)
d_L	Thickness of the liquid film (m)
D_{AB}	Diffusion coefficient of mass transfer ($m^2\ s^{-1}$)
D_G	Molecular diffusivity of the compound in the gaseous phase ($kg\ m^{-3}$)
D_L	Molecular diffusivity of the compound in the liquid phase ($kg\ m^{-3}$)

F	Equilibrium molar fraction of the gas in solution (dimensionless)
F_1, F_2	Blending functions of the $K-\omega\ SST$ model
H'	Henry's Law constant (dimensionless)
J	Total flow between the phases ($kg\ s^{-1}\ m^{-2}$)
J_A	Mass flow of substance A ($kg\ s^{-1}\ m^{-2}$)
J_G	Mass flow of substance A in the gaseous phase ($kg\ s^{-1}\ m^{-2}$)
J_L	Mass flow of substance A in the liquid phase ($kg\ s^{-1}\ m^{-2}$)
k_G	Mass transfer coefficient of the gaseous phase ($m\ s^{-1}$)
k_L	Mass transfer coefficient of the liquid phase ($m\ s^{-1}$)
$\mathbb{K}_G$	Global mass transfer coefficient of the gaseous phase ($m\ s^{-1}$)
$\mathbb{K}_L$	Global mass transfer coefficient of the liquid phase ($m\ s^{-1}$)
K	Turbulent kinetic energy ($m^2\ s^{-2}$)
K_s	Mean roughness elements height (m)
m_A	Mass fraction ($kg_A\ kg_{Mixture^{-1}}$)
p	Pressure (Pa)
p_A	Partial pressure of the gas adjacent to the interface (Pa)
P_k	Production of turbulent kinetic energy ($N\ m^{-2}\ s$)
Re_r	Roughness Reynolds number (dimensionless)
S	Deformation tensor (s^{-1})
u	Horizontal velocity ($m\ s^{-1}$)
u^+	Streamwise wind velocity (dimensionless)
u^*	Friction velocity ($m\ s^{-1}$)
u_i, u_j	Velocity in i and j directions ($m\ s^{-1}$)
U, V, W	Velocity components in directions x, y and z ($m\ s^{-1}$)
U_i	Velocity components in i direction ($m\ s^{-1}$)
x, y, z	Streamwise, vertical and spanwise coordinates (m)
x_i, x_j	Coordinate in i and j directions (m)
y^+	Wall distance (dimensionless)
z	Domain height (m)
z_0	Roughness length (m)

Greek symbols

α, β, σ_k, σ_ω	Constants in the $K-\omega\ SST$ model
σ_{ω_2}	Constant in the $K-\omega\ SST$ model from the $K-\varepsilon$ model
β^*	Empirical coefficient of the $K-\omega$ model
δ_{ij}	Kronecker delta (1, if $i=j$ and 0, if $i\neq j$)
ε	Turbulent kinetic energy dissipation rate ($m^2\ s^{-3}$)
κ	Von Kármán constant (dimensionless)

μ	Molecular viscosity ($kg\ m^{-1}\ s^{-1}$)
μ_t	Turbulent viscosity ($kg\ m^{-1}\ s^{-1}$)
ν	Kinematic viscosity ($m^2\ s^{-1}$)
ρ	Density ($kg\ m^{-3}$)
σ	Height of the boundary layer (m)
τ_0	Shear stress at the gaseous interface ($kg\ m^{-1}\ s^{-2}$)
τ_{ij}	Stress tensor ($N\ m^{-2}$)
τ_{ij}^{lam}	Viscous Stress tensor ($N\ m^{-2}$)
τ_{ij}^{turb}	Reynolds turbulent stress tensor ($N\ m^{-2}$)
ω	Specific dissipation rate (s^{-1})

Subscript

i, j, k	Indicial notation
a	Atmospheric flow
tv	Flow inside the wind tunnel

Superscript

$'$	Fluctuations
$-$	Average value
$+$	Dimensionless values using the variables y and u

Contents

1 Introduction

Complaints from the population living close to installations characterized by emissions of odorous compounds (e.g. landfills, coke production, wastewater treatment plants, chemical industries, food industries, cellulose and paper industries, agro-industries) are becoming increasingly more frequent (CAPELLI et al., 2008b). Odor emitted by these facilities causes complaints of annoyance, eye, nose and throat irritation, headache, nausea, diarrhea, hoarseness, changes in the respiratory system (for instance, sore throat, cough, nasal congestion), palpitations, shortness of breath, stress, somnolence and mood changes (SCHIFFMAN; WILLIAMS, 2005). It is important to differentiate odorants and odors. An odorant is a compound that transmits an odor, and an odor is the effect perceived if an odorant gas is detected and interpreted by the olfactory system (GOSTELOW; PARSONS; STUETZ, 2001).

Odorous compounds from landfills originate mainly from the release of gases that are formed during the biological and chemical processes of waste decomposition (EL-FADEL; FINDIKAKIS; LECKIE, 1997). The odorous compounds from landfills comprise more than 100 different chemical compounds (PARKER; DOTTRIDGE; KELLY, 2002) and the odorous compounds released by the wastewater treatment plants (WWTP) come from families of chemical compounds such as sulfur, nitrogen and other volatile organic compounds (ANDREÃO et al., 2019). These compounds can be emitted by passive area sources.

Passive area sources are surfaces with a low degree of disturbance (but they can be disturbed by wind/waves) and can be found in landfill sites and in some stages in WWTP (e.g., sedimentation tanks, anaerobic digesters, sludge storage tanks). The estimation of odorous gases emission presents certain difficulties in these area sources. In this situation, it is not easy to measure a representative odorous gas concentration as the gas flow rate is unknown. Therefore, special sampling methods are adopted to allow the estimation of odorous compounds emission rate in these types of sources (JIANG; KAYE, 1996).

In general, the estimation of odorous compounds emissions in area sources can be determined by adopting two different approaches: indirect sampling (using micrometeorological methods) and direct sampling (using devices that enclosure the gas) (CAPELLI et al., 2012). The micrometeorological measurement techniques require the collection of a substantial number of samples, generating a high cost, which makes them more difficult to execute (HUDSON; AYOKO, 2008b). The direct sampling method consists in enclosing small parts of the surface in a device in which the flow is controlled, and, thus, the emission rate is calculated as the product of concentration and the flow rate at the outlet of this device (JIANG; BLISS; SCHULZ, 1995). Direct methods are less costly compared to indirect methods and allow the quantification of the emission rate in specific regions of the odor source. The two main devices used in direct

measurements are the dynamic flux chamber (DFC) and the portable wind tunnel (PWT).

DFC and PWT are portable open-bottom devices that are placed over the emitting surface. In their operation, a part of the emitting surface is isolated and a neutral and odorless air is introduced into the device. The main difference regards the shape of the two devices. While the DFC has a spherical shape and assumes flow features that provides a well-mixed compartment, the PWT attempts to simulate the action of the wind on the surface (parallel flow without vertical mixing). The concentration of odor measured at the exit of the devices depends on its volatilization from the surface sampled and on the dilution that occurs inside the device. This phenomenon of mass transfer depends on several factors. While the principal force that determines the emission rate of a compound is the difference in the concentration between the two phases (liquid and gas), the magnitude of the Henry's constant (H') is also very important in determining the mass transfer rate of a compound. The turbulence in the liquid phase is significant for highly volatile materials (with high H' values), while air turbulence (i.e. wind velocity) is important for the mass transfer velocity in the liquid-gas surface for all compounds, in particular those with small H' values. Most odorants have small H' values (HUDSON; AYOKO, 2008b). For odor impact evaluation purposes, it is important to understand the mass transfer phenomenon (CAPELLI et al., 2012).

At passive liquid surfaces, the interaction between the liquid-phase and the sweeping wind directly interfere in the volatilization of compounds. In these situations, the volatilization can be described by a two-resistance mass transfer model and the concepts of liquid (k_L) and gas (k_G) mass transfer coefficients (PRATA JR. et al., 2018). The estimation of k_L and k_G involves at least one variable representing wind forcing and another for the compound molecular diffusion. Wind speed at a certain height and the friction velocity (u^*) are frequently used in the scaling of the mass transfer coefficients to represent wind forcing (PRATA JR. et al., 2017). Thus, the friction velocity is an important parameter to be considered when estimating emissions of odorous compounds with sampling devices.

Studies show that the results obtained using the flux chamber differ from those obtained by using the wind tunnel (HUDSON; AYOKO, 2008b; HUDSON; AYOKO, 2009a; HUDSON et al., 2009b). The main concern regarding the use of the flux chamber is the fact that odorous compounds can accumulate inside the equipment, raising its concentration in the gas-phase (HUDSON; AYOKO, 2008b). If the sweep flow rate is too low, the gas concentration will reach a point where gas-phase resistance will control the emission process (GHOLSON et al., 1991). This could suppress the emission rate of the compound, resulting in an incorrect measurement of the emission rate at the site, differing from the emission that would actually occur in the absence of the flux chamber (GOSTELOW et al., 2003). Sometimes, it is necessary to use a fan or impeller to promote the mixing inside the chamber. According to Andreão (2016), if no fan is used, the flow inside the chamber is not completely mixed, presenting non-homogeneous spots and very low friction velocity values (that does not represent the real condition).

The wind tunnel is recommended as an appropriate direct sampling method to evaluate the emission rate of odorous compounds from liquid-gas or solid-gas interface area sources (CAPELLI et al., 2008b; HUDSON; AYOKO, 2008b; LAOR; PARKER; PAGÉ, 2014). There is no universally consensual portable wind tunnel model yet. Variations in the tunnel include differences in the material used in the construction, in the length/width ratio, in the height and in the area of the surface sampled and, consequently, the effect on the dynamics of the flow on the surface (SMITH; WATTS, 1994a). It is important to take into account that any device used to sample odorous gas disturbs the emitting surface and interferes in the emission rate (HUDSON; AYOKO, 2008b).

Therefore, it is important to know that aspects related to the flow and mass transport established inside the direct measurement equipment influence the odor emission rate measurements (HUDSON; AYOKO, 2008a). As mentioned before, there are different odor passive area sources and so odorous gases can be emitted from liquid (lagoons in WWTP) and solid (such as landfill) surfaces which present different roughness for which case the friction velocity over the surface is different, causing different mass transfer coefficient for the same odorous compound. Thereby, it is necessary to investigate the dynamics of the flow and mass transfer inside these devices to assess the equipment reliability.

Therefore, this work proposes analyzing the air flow inside the wind tunnel positioned over surfaces with different roughness in order to simulate the air flow over idealized liquid surfaces of sewage treatment plants and solid landfill surfaces. The present work used a wind tunnel model designed by Jiang, Bliss and Schulz (1995) at the University of New South Wales (UNSW) in Australia. This wind tunnel was aerodynamically designed to create a well-developed boundary layer environment (WANG; JIANG; KAYE, 2001) in order to obtain reliable samples from the odor sources and it has been used in several odor measurements studies (SCHMIDT; BICUDO; JANNI, 1999; GALVIN et al., 2002; BALSARI et al., 2007; HUDSON; AYOKO, 2008b; HUDSON et al., 2009b; PRATA JR. et al., 2014; LIU et al., 2015; PERTA et al., 2016; MARTINS et al., 2018).

2 Objectives

2.1 General objective

To investigate the air flow inside the portable wind tunnel developed by Jiang, Bliss and Schulz (1995) to estimate odorous gases emission from quiescent liquid surface.

2.2 Specific objective

- To analyze the air flow patterns inside the portable wind tunnel;
- To evaluate the friction velocity distribution over the surface with no roughness inside the portable wind tunnel under standard operational conditions;
- To examine the influence of different surface roughness on the surface friction velocity.

3 Literature review

3.1 Background information on volatilization from quiescent surfaces

Volatilization is the mass transfer process of a compound dissolved in liquid or solid to an adjacent gaseous phase. In general, the mass of a compound is transferred from a region of higher concentration to a region of lower concentration.

The two films theory, developed by Lewis and Whitman (1924), suggest that, in the gas-liquid interface, there are two thin layers of fluid with no movement, one in the liquid phase and other in the gas phase (Figure 1). These films are practically free of convection streams and, consequently, any solute transfer through these films must occur by the diffusion process (LEWIS; WHITMAN, 1924).

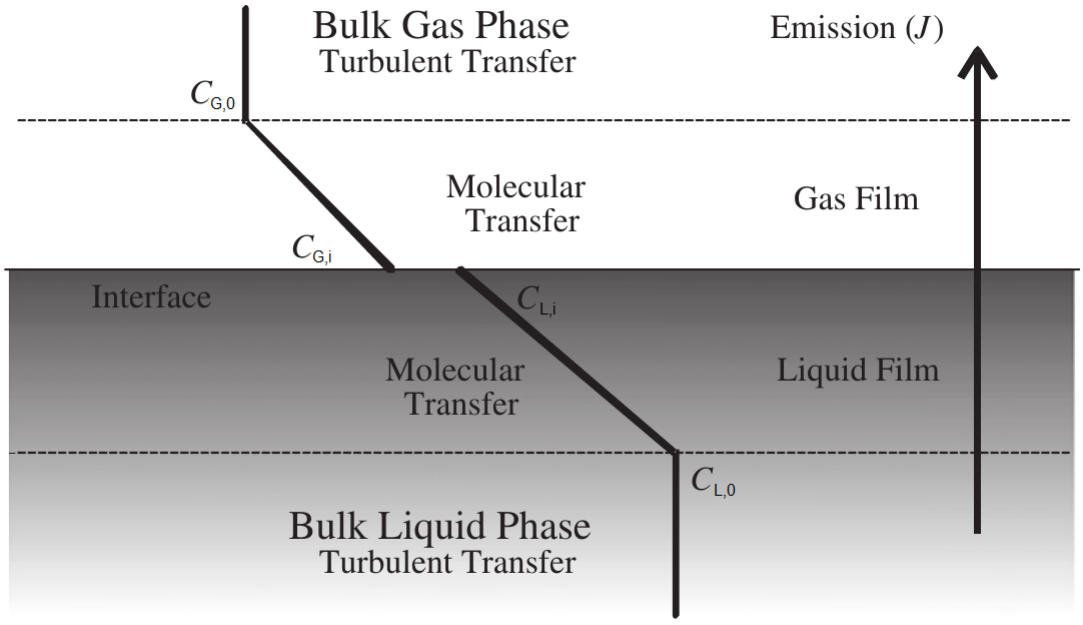

Figure 1: Gas-liquid film. From Santos et al. (2012).

In the quiescent liquid phase, molecular diffusion is the only transport mechanism of the substance from the liquid film to the liquid-gas interface. The volatilization process at the liquid-gas interface can be represented by Fick's Law of molecular diffusion represented in Equation 3.1:

$$J_A = -D_{AB}\frac{\partial \rho m_A}{\partial z} \tag{3.1}$$

where A indicates the substance that is diffused into substance B; J_A is the mass flux of substance A ($kg\ s^{-1}\ m^{-2}$); D_{AB} is the diffusion coefficient or diffusivity from A into B ($m^2\ s^{-1}$); ρ represents the mixture absolute density ($kg\ m^{-3}$); m_A is the mass fraction ($kg_A\ kg_{Mixture}^{-1}$). The negative signal indicates that the flux is in the opposite direction of the concentration gradient.

Equation 3.1 can be rewritten as a function of the vertical concentration gradient:

$$J_A = -D_{AB}\frac{\partial C_A}{\partial z} \tag{3.2}$$

A concentration gradient is considered in each film and within each phase outside the film there is sufficient turbulence to eliminate the concentration gradient. Therefore, the mass transfer resistance present in the films is the limiting factor of the mass transfer process between the phases.

According to the two films theory, the mass flux of substance A in the liquid (J_L) and gaseous (J_G) phases are represented, respectively, by:

$$J_L = -D_L\frac{\partial C_L}{\partial z} = -D_L\frac{C_{L,i} - C_{L,0}}{d_L} \tag{3.3}$$

and

$$J_G = -D_G\frac{\partial C_G}{\partial z} = -D_G\frac{C_{G,i} - C_{G,0}}{d_G} \tag{3.4}$$

where J_L and J_G are the mass flows of substance A ($kg\ s^{-1}\ m^{-2}$) in the liquid and gaseous phases, respectively; D_L and D_G are the molecular diffusivity of the compound in the liquid and gaseous phases ($kg\ m^{-3}$), respectively; $C_{L,i}$ and $C_{G,i}$ are the concentrations of the compound in the liquid/gas interfaces ($kg\ m^{-3}$), respectively; $C_{L,0}$ and $C_{G,0}$ are the concentrations of the compound in the liquid and gaseous phases' interior ($kg\ m^{-3}$), respectively, and d_L and d_G are the thickness of the liquid and gaseous films (m).

The Equations 3.3 and 3.4 can be rewritten as:

$$J_L = \mathsf{k}_L(C_{L,0} - C_{L,i}) \tag{3.5}$$

and

$$J_G = \mathsf{k}_G(C_{G,i} - C_{G,0}) \tag{3.6}$$

where $\mathsf{k}_L = D_L/d_L$ and $\mathsf{k}_G = D_G/d_G$.

Being k_L the mass transfer coefficient in the liquid phase ($m\ s^{-1}$) and k_G the mass transfer coefficient in the gaseous phase ($m\ s^{-1}$).

The distribution of a compound between the liquid and gaseous phases follows a defined proportion under ideal equilibrium conditions, mathematically described by Henry's Law:

$$H' = \frac{C_{G,i}}{C_{L,i}} \tag{3.7}$$

where H' is the non-dimensional Henry's Law coefficient.

Thus, a dynamic equilibrium is represented, where the mass flow in the liquid-gas direction compensates the mass flow in the opposite direction, so that the final balance becomes zero. If this equilibrium does not occur, an effective mass transfer between the phases is verified. This transfer may occur in the liquid-gas (volatilization) or gas-liquid (solubilization) direction. Even under these conditions in which there is an effective mass transfer between the phases, it is considered that the equilibrium at the liquid-gas interface is established instantaneously.

The mass transferred through the liquid film (J_L) is the same transferred through gaseous film (J_G), corresponding to the total flow between the phases (J).

So,

$$J = \mathsf{k}_G(C_{G,i} - C_{G,0}) = \mathsf{k}_L(C_{L,0} - C_{L,i}) \tag{3.8}$$

Substituting the Henry's constant (Equation 3.7):

$$C_{L,i} = \frac{\mathsf{k}_L C_{L,0} + \mathsf{k}_G C_{G,0}}{\mathsf{k}_G H' + \mathsf{k}_L} \tag{3.9}$$

Substituting Equation 3.9 in Equation 3.5:

$$J_L = \frac{\mathsf{k}_L \mathsf{k}_G H'}{\mathsf{k}_L + \mathsf{k}_G H'} \left(C_{L,0} - \frac{C_{G,0}}{H'} \right) \tag{3.10}$$

$$J_L = \mathbb{K}_L \left(C_{L,0} - \frac{C_{G,0}}{H'} \right) \tag{3.11}$$

where

$$\mathbb{K}_L = \frac{\mathsf{k}_L \mathsf{k}_G}{\mathsf{k}_G + \mathsf{k}_L / H'} \text{ or } \frac{1}{\mathbb{K}_L} = \frac{1}{\mathsf{k}_L} + \frac{1}{\mathsf{k}_G H'} \tag{3.12}$$

where $\mathbb{K}_L$ is the global mass transfer coefficient in the liquid phase ($m\ s^{-1}$). The terms $1/\mathsf{k}_L$ and $1/\mathsf{k}_G H'$ are the relative resistances to the liquid and gaseous films, respectively. Therefore, $\frac{1}{\mathbb{K}_L}$ represents the global resistance to the mass transfer between the phases. Thus, the global mass transfer coefficient is an important parameter that includes the effects of Henry's law, along with the individual mass transfer through the liquid and gaseous films.

Analogously to the gas phase, the following equation is obtained:

$$J_G = \frac{\mathsf{k}_L \mathsf{k}_G}{\mathsf{k}_L + \mathsf{k}_G H'} (C_{L,0} H' - C_{G,0}) \tag{3.13}$$

$$J_G = \mathbb{K}_G (C_{L,0} H' - C_{G,0}) \tag{3.14}$$

where

$$\mathbb{K}_G = \frac{\mathsf{k}_L \mathsf{k}_G}{\mathsf{k}_L + \mathsf{k}_G H'} \text{ or } \frac{1}{\mathbb{K}_G} = \left(\frac{H'}{\mathsf{k}_L} \right) + \frac{1}{\mathsf{k}_G} \tag{3.15}$$

where $\mathbb{K}_G$ is the global mass transfer coefficient in the gaseous phase ($m\ s^{-1}$).

To solve Equation 3.11, it is necessary to know the values of $C_{L,0}$, $C_{G,0}$, H' and $\mathbb{K}_L$. The mass transfer (liquid-gas or gas-liquid) direction is determined by the sign of the difference

between C_L and C_G/H' being the volatilization indicated by the positive sign of J and the solubilization by the negative sign, according to the reference adopted.

To less soluble compounds, with H' much higher than 10^{-3}, the term $1/\mathsf{k}_G H'$ becomes negligible ($\mathbb{K}_L \approx \mathsf{k}_L$), i. e. the overall mass transfer coefficient is limited by the transport conditions in the liquid film. To more soluble compounds, with H' significantly lower than 10^{-3}, it is possible to neglect the term $1/\mathsf{k}_L$, i. e. $\mathbb{K}_L \approx \mathsf{k}_G H'$. In this case, the overall mass transfer coefficient is limited by the transport conditions in the gaseous film. For those cases where the value of H' is about 10^{-3}, none of the terms can be neglected, so that both the conditions of the liquid film and those of the gaseous film are significant for the final value of the overall mass transfer coefficient.

The solid-gas mass transfer is a more complex process (CAPELLI et al., 2012). However, the transfer of a diffusing substance can be described by means of the same basic law used for a gas being transferred through a liquid, Fick's law. N_A, the rate of diffusion of substance A per unit of the cross section area of solid, is proportional to the concentration gradient in the direction of diffusion, $-\partial C_A/\partial z$:

$$N_A = -D_A \frac{\partial C_A}{\partial z} \tag{3.16}$$

where D_A is the diffusivity of A through the solid ($m^2\ s^{-1}$). If D_A is constant, integration of equation 3.16 for *diffusion through a thin flat slab* of thickness Δz results in:

$$N_A = \frac{D_A(C_{A1} - C_{A2})}{\Delta z} \tag{3.17}$$

where C_{A1} and C_{A2} are the concentrations at opposite sides of the slab. For other solid shapes, the rate is given by:

$$w = N_A S_{av} = \frac{D_A S_{av}(C_{A1} - C_{A2})}{\Delta z} \tag{3.18}$$

with appropriate values of the average cross section area, S_{av}, to be applied.

Diffusion can be spherical, as it might be from a microorganism colony in soil. The *radial diffusion through a spherical shell* of inner and outer radius a_1 and a_2 is:

$$S_{av} = 4\pi a_1 a_2 \tag{3.19}$$

$$\Delta z = a_2 - a_1 \tag{3.20}$$

3.2 Estimating emission rate of odorous compounds

According to Parker et al. (2013), the following measuring approaches are the principal ones for estimating the emission rate of area sources:

- Indirect methods (including micrometeorological techniques) where the ambient concentrations are measured and the sources emission rates are calculated using inverse dispersion models;

- Direct methods in which the flow is calculated from concentration and flow rate measurements using portable wind tunnels or flux chambers.

Besides measuring techniques, there are also algebraic mathematical models that allow the estimation of emission rate of odorous compounds in quiescent area sources. These models are of importance especially for environmental impact studies in which odor sources have not been installed yet. The model proposed by Gostelow, Parsons and Stuetz (2001) and the models of the computational programs WATER9 (U.S.EPA, 2001) and TOXCHEM+ (ENVIROMEGA, 2004) are analytical models used for mass transport through a quiescent surface exposed to the atmosphere. These models require empirical derivations of the mass transfer coefficients for the liquid (k_L) and gas (k_G) phases, and the volatilization is usually modeled based on Fick's law of molecular diffusion (SANTOS et al., 2012). Prata Jr. et al. (2018) analyzed the theoretical and empirical formulations of the gas-film and liquid-film mass transfer coefficients at passive liquid surfaces, focusing on the relevant aspects for the study of atmospheric emissions from wastewater treatment plants and similar facilities.

The indirect methods, where the mass flux is calculated from concentrations measured in the trail of the emitted material, present limitations since it is necessary to sample the gases in the environment in several locations downstream the source in order to obtain representative results (PARKER et al., 2013). Indirect techniques do not disturb the emission process because a sampling device is not used at the source. However, the large number of samples needed to determine the ambient concentration makes this method impractical for odor evaluations (HUDSON; AYOKO, 2008a). For this reason, the direct methods are the most used techniques for the evaluation of emission rates of quiescent area sources (CAPELLI; SIRONI; ROSSO, 2013b).

There are two different types of direct sampling methods: dynamic and static sampling. In the dynamic sampling, the air flow is actively passed through the device (blown by an external fan) at a measured rate, being conducted directly from the emitting source to the measuring device. The static sampling does not present an external air flow and involves the sample in an appropriate container, which is connected to the measuring device at a later stage (CAPELLI; SIRONI; ROSSO, 2013b). Flux chambers can be either static or dynamic and wind tunnels are always related to dynamic sampling.

Static chambers can be subdivided into cylindrical, rectangular and a combination of these two. According to Hudson and Ayoko (2008b), static chambers are more likely to be cylindrical than rectangular, however, the dynamic devices are more likely to be rectangular. This is probably due to the fact that is simpler to inject air from one side to the other in rectangular

devices than in cylindrical ones. According to the authors, rectangular devices provided more representative and less concentrated samples than cylindrical devices, and it is also unlikely to occur accumulation and, consequently, overestimation of the volatile compounds when using them. The authors also said that the cylindrical chambers should have a small sample period in order to avoid overestimation of the sample values, which may also alter the composition of the samples.

The design and the operational conditions of the dynamic flux chamber and the wind tunnel are quite different. The wind tunnel (Figure 2a) is an empty, open, rectangular unit through which a flow of odorless filtered air sweeps a liquid or solid surface emitting odors, and air samples are collected at the outlet. For the flux chamber (Figure 2b), odorless air is introduced into a space above the odor-emitting surface. Both devices use floats in order to be used over liquid surfaces. The air samples are assumed to be homogeneous and, therefore, representative of a uniformly distributed concentration throughout the flux chamber space (NAVARATNASAMY; EDEOGU; FEDDES, 2009).

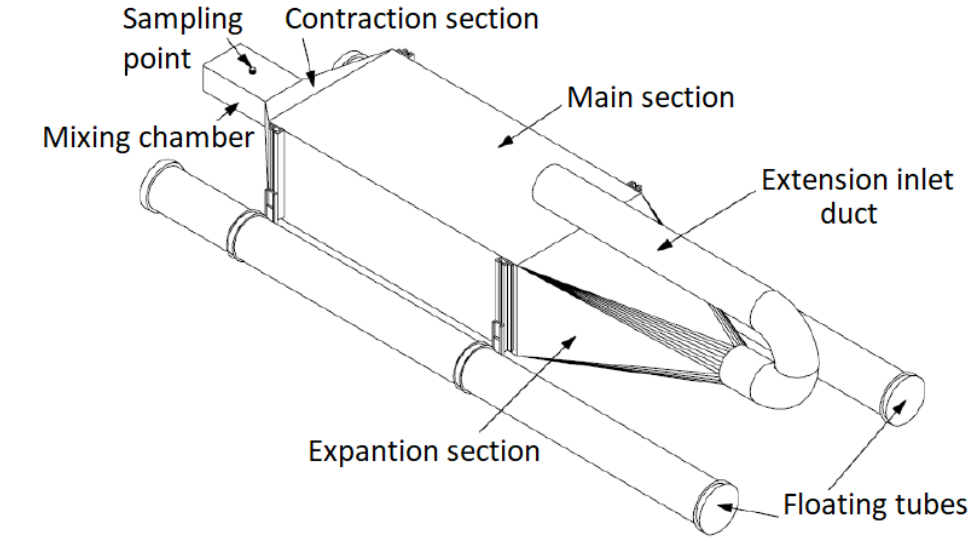

(a)

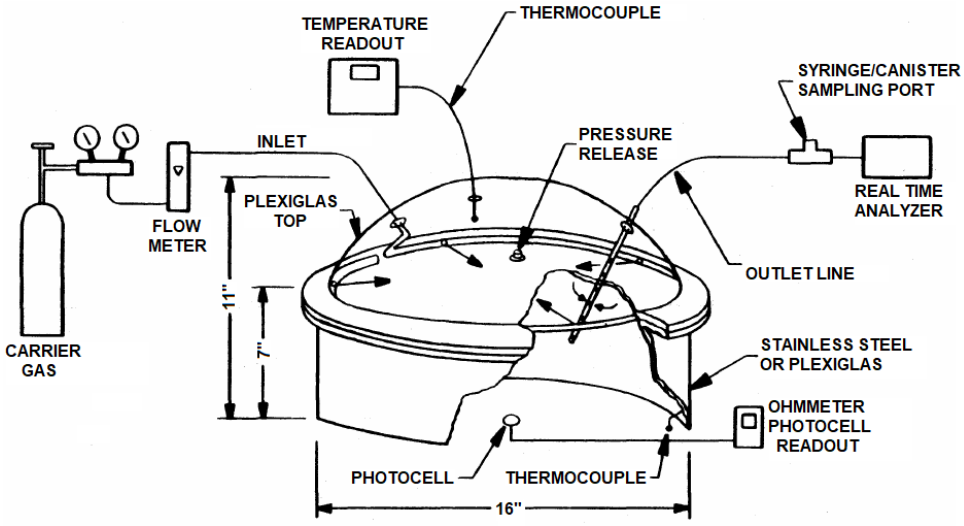

(b)

Figure 2: Devices used in the measurement of odorous compounds: (a) Wind tunnel (from Jiang, Bliss and Schulz (1995)) and (b) Flux chamber (from Eklund (1992)).

A wide range of devices configurations can be found in the literature for the direct quantification of the emission rate of odorous compounds, differing in terms of size, dimensions and operational conditions. In this context, the works of Hudson and Ayoko (2008a) and Hudson and Ayoko (2008b) can be highlighted. They carried out a literature review on the devices of different sizes and shapes and their measured emission rate.

Due to the fact that different odor sampling devices provide different emission rates, Hudson and Ayoko (2008a) studied the mass transfer processes emphasizing the properties of the odorous compounds and the physical conditions that exist within the odor sampling devices. They reviewed the mass transfer process, explaining the implication of Henry's law constant; the influence of water and air temperature, wind velocity, water velocity (turbulence), chemical reactions and surface contamination in the air-water exchange processes.

They emphasize that it is important to select a sampling device that reproduces as accurately as possible the natural conditions of the atmospheric flow, otherwise, a device with low air turbulence may favor the selection of odorants with high values of H' (less soluble compounds) and the selection of odorants with low H' values (more soluble compounds) may be artificially reduced. Compounds with high H' values have the liquid turbulence as an important factor, especially if the air turbulence is low. Thus, compounds with high H' values will have their emission potentialized by increasing the wind speed (turbulence) within the sampling device, as well as compounds with low H' values. Typically, relatively non-turbulent devices, such as the flux chamber, are used to sample odors at wastewater works. This may be an unfavorable situation on turbulent liquid surfaces as they favor the emission of compounds with high H' values while the low turbulence within the sampling device may suppress the emission of other odorants with low H' values. So, the emission rate obtained from devices similar to the flux chamber should be compensated using a factor to account for wind turbulence. They also provided Table 1, which shows the influence of aerodynamic conditions of the sampling device combined with the nature of the odorous compound.

Hudson and Ayoko (2008b) affirm that other studies have also shown that samples obtained from wind tunnels can be related to those obtained by micrometerological methods, what is important if the emission rates derived from these devices are going to be used as input on dispersion models. Thus, they came to the conclusion that wind tunnels are more likely to reproduce natural conditions and, therefore, should be preferred to estimate odor emission rates over the dynamic, chamber-type devices.

Differently from the flux chamber that is standardized by the United States Environmental Protection Agency (USEPA) (it establishes specifications and guidelines for assembly and use of a dynamic flux chamber), there is no universally wind tunnel model defined. Therefore, there are in the literature numerous studies concerning the development of wind tunnels for odor measurements.

Table 1 – Likely impact of aerodynamic conditions in the sampling of odorants and odor emission rates. From Hudson and Ayoko (2008a)

Odor sampling technique	Predominant aerodynamic condition	Likely influence on emission rate of various chemicals on basis of Henry's coefficient			Likely implications for emission rates of specific odorants	Likely observed impact on odor emission rate
		H' high	H' intermediate	H' low		
Device-independent	Still conditions (low turbulence)	Relative increase	Relative increase for low H'	Relative decrease	Hydrogen sulfide, mercaptans and thiols over-represented relative to more polar odorants	Relatively low odor emission rate
	Windy conditions (high turbulence)	Increase	Increase	Increase with wind speed, increase relative to compounds with high H'	Emission rates for all odorants increased, but more so for polar compounds e.g. volatile fatty acids and phenols	Relatively high odor emission rate
Flux chamber	Low turbulence	Relative increase (vs wind tunnel)	Relative increase (vs wind tunnel)	Relative decrease (vs wind tunnel)	Hydrogen sulphide, mercaptans and thiols over-represented relative to more polar odorants	Low emission rate relative to wind tunnel and device-independent techniques
Wind tunnel	Moderate turbulence	Relative increase (vs flux chamber)	Relative increase for low H' (vs flux chamber)	Marked increase (vs wind tunnel)	More polar odorants such as phenols and volatile fatty acids increasingly represented in odorant composition relative to hydrogen sulfide, mercaptans and thiols	High emission rate relative to flux chamber, comparable to emission rate derived from device-independent techniques

The study developed by Jiang, Bliss and Schulz (1995) was the basis for several other wind tunnel studies. They evaluated the aerodynamic performance of a wind tunnel (Figure 3a) made to measure the emission rate of area sources based on the Lindvall (1970) hood. The device is put on a liquid surface and an air flow, filtered by an activated carbon, is supplied to the sampling hood by a fan. With the execution of preliminary tests to measure the velocity distribution by anemometer, smoke tests and dry ice tests, they observed some problems with the design of Lindvall's hood. The flexible duct at the inlet changed the velocity profile inside the hood, what made the flow pattern variable during different tests. The expansion section of the hood ejected the air into the main section, creating a rotation inside it and a dead zone near the corners. They observed, during smoke tests, that the air flow generated rotation about a vertical axis, that could be solved by increasing the length of the hood or by providing flow distribution devices, according to the authors. The sensitivity of the anemometer used in this study limited the minimum air velocity to about 0.33 $m\ s^{-1}$. The experiments were performed at velocities of 0.33, 0.43, 0.54 and 0.78 $m\ s^{-1}$. Modifications in the original design were made. An extension of the inlet duct was designed to allow the flow to enter the expansion section in a consistent way. Three vertical flat vanes were placed in the expansion section (shown in Figure 3b with measurements in mm) with the objective to eliminate the jet effect, however, the tests indicated that the rotation still existed. This rotation was stopped by adding a perforated baffle into the tunnel. They concluded that the modifications established the necessary steady and repeatable flow inside the hood.

With the objective to validate the design of the wind tunnel developed by Jiang, Bliss and Schulz (1995); Bliss, Jiang and Schulz (1995) carried out an ammonia simulation in laboratory to test the relationship between air velocity and chemical emissions. In this experiment, ammonia solution was dissolved in a swimming pool that was filled with water. The water temperature and pH were checked during the tests and a sample was collected in the middle of every run.

Bliss, Jiang and Schulz (1995) calculated the concentration of ammonia in water and air, the ammonia emission rate inside the odor sampling hood and the convective mass transfer coefficient. The ammonia mass transfer depends on the ammonia concentration in the water, the pressure, the air velocity and the temperature of water and air. According to the measurements made, a velocity of 0.6 $m\ s^{-1}$ is the maximum that should be used in field for this device. Comparing the mass transfer coefficient inside the hood with the one calculated from the boundary layer equation for a laminar boundary layer, it was concluded that the first one is 10% smaller. Ammonia concentration in the water, temperature, and pressure on convective mass transfer coefficient probably did not contribute to this error. The 10% error is more likely to be the result of the combination of ammonia trapping and measurement techniques, according to the authors.

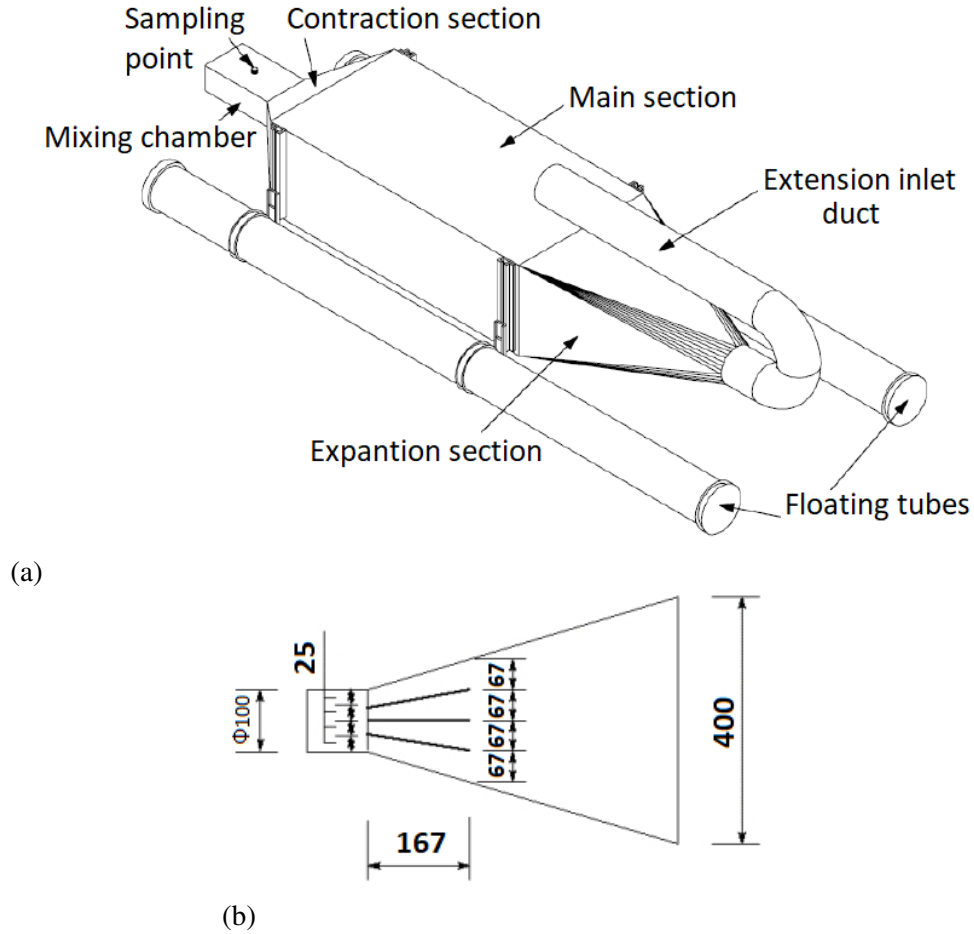

Figure 3: Figures: (a) An isometric drawing of the wind tunnel and (b) flat vanes added to the expansion section. From Jiang, Bliss and Schulz (1995).

Also based on the work of Jiang, Bliss and Schulz (1995), Wang, Jiang and Kaye (2001) carried out a series of experiments to investigate recovery rates for the wind tunnel system. They proposed some modifications in the original tunnel and tested both standard and modified wind tunnel (Figure 4). They first analyzed the standard wind tunnel sampling system using carbon monoxide (CO) as a tracer gas and, then, modifications were made to improve sample recovery. The air velocity used inside the tunnel was 0.3 $m\ s^{-1}$, based on the work of Jiang (1993). At first, they increased the length of the mixing chamber from 200 mm to 500 mm. After that, an extension was added to the end of the wind tunnel. A rotameter, a pump and a CO sensor were added to the system to collect the sample of CO from the outlet of the wind tunnel. Using the standard wind tunnel, the recovery rates for the CO tracer gas ranged between 37% and 48%, and using the modified wind tunnel, the tracer gas recovery rates ranged between 83% and 100%.

Although the tunnel of Jiang, Bliss and Schulz (1995) was studied by several authors, there was still no universal model defined for odor measurements, which has motivated other researchers to develop new wind tunnel models. Capelli et al. (2009b) developed and validated an experimental wind tunnel system for sampling odorous gases. The wind tunnel was constructed with the purpose of making the turbulent flow (medium) as uniform as possible. For this

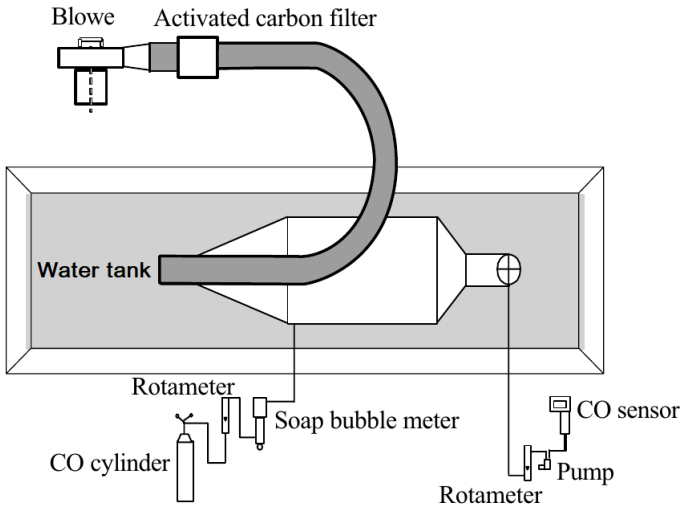

Figure 4: Ilustration of the modified wind tunnel system. From Wang, Jiang and Kaye (2001).

purpose, they proposed a model of wind tunnel completely horizontal, without any curve, with a perforated grid at the wind tunnel inlet and with three flow deflection vanes (Figure 5). Results of velocity measurements inside the tunnel showed that uniform and homogeneous flow was achieved throughout the test section. Experiments in laboratory (with n-butanol) and on field in sewage treatment plants were also performed and the samples collected were analyzed by dynamic olfactometry. Both the experimental and laboratory tests showed a good agreement with theoretical mass transfer coefficients (derived from the application of the volatilization model based on the Prandtl's boundary layer theory), demonstrating the suitability of the studied wind tunnel for the simulation of specific odor emission rates from liquid area sources.

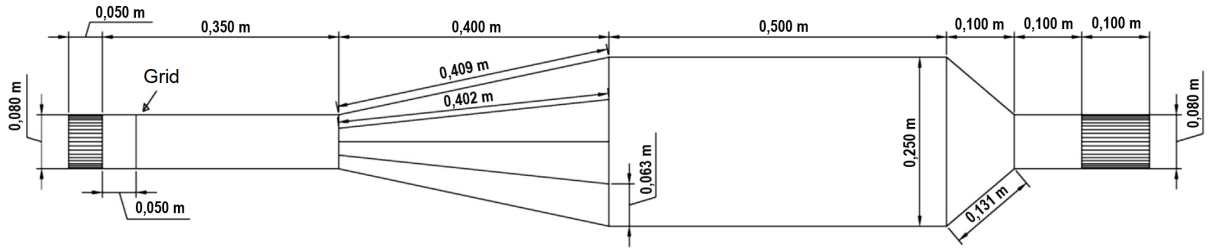

Figure 5: Wind tunnel's scheme. From Capelli et al. (2009b).

Based on the tunnel of Jiang, Bliss and Schulz (1995), Liu et al. (2015) developed a wind tunnel system (Figure 6) to measure volatile compounds (VOCs) emission rates on the working face of a landfill site in China. The system contains a nitrogen cylinder that supplies gas (N_2) flow, a vortex flow meter, the wind tunnel and a gas sampler. They decided to use nitrogen as the carrier gas through the tunnel, instead of using ambient air filtered by activated carbon, because the filter might not absorb all the VOCs in the air. They also added a buffer room made of dense iron mesh in the inlet duct with the objective to make the airflow as uniform as possible, and a horizontal baffle at the edge of the main chamber to keep the contact area

of the wind tunnel in a horizontal position. A gas-chromatograph (mass-spectrometer) was used for the qualitative and quantitative analysis of VOCs in gas samples. Eight different flow rates were tested in order to measure the relationship between the sweeping velocity and VOC emission rate. After the tests, a nitrogen flushing flow rate of $19\ m^3\ h^{-1}$ ($u = 0.28\ m\ s^{-1}$) was chosen to perform the study. Results from the odor measurements showed that the emission rate increased with sweeping velocity. The sampling campaign was performed in a 24h period and it was noticed that the highest average emission rates of VOCs were observed from midnight to dawn, and oxygenated compounds appeared to be the most abundant ones. They also noticed that hydrocarbons, aromatics, and halogenated compounds composed significant percentages of the total emission. The emission of reduced sulfur compounds were relatively low in comparison with the total VOC emission, and sulfur compounds are commonly related as odor compounds.

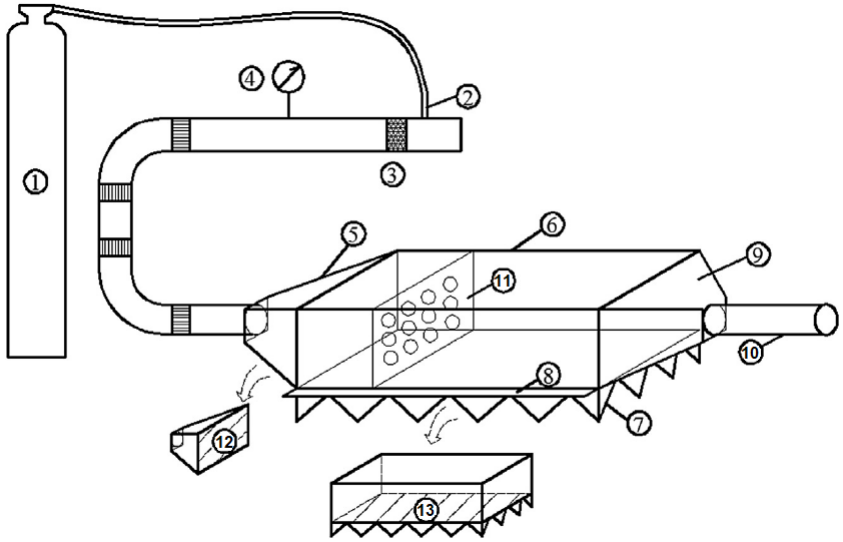

Figure 6: Scheme of the wind tunnel system: 1 - cylinder; 2 - inlet; 3 - Buffer room; 4 - Vortex flow meter 5 - Expansion chamber; 6 - Main chamber; 7 - Jagged edge; 8 - Horizontal baffle; 9 - Contraction chamber; 10 - Gas outlet; 11 - Perforated plate; 12 - Cross-section; 13 - Contact section. From Liu et al. (2015).

Capelli et al. (2012) developed a wind tunnel to be used over solid area sources and they adopted a theoretical model for the volatilization of odorous compounds from solids into the atmosphere. The tunnel is a rectangular chamber made of stainless steel (Figure 7). The experiments were performed in a laboratory and, to simulate the emission of odorants from the soil, an odorant was dissolved into a liquid phase located below of a layer of a chemically inert porous solid. The odorant is diffused through the pores of the solid to the upper air stream flow, where it is measured. In order to validate the results, preliminary tests were run on a liquid surface without any solid material. The experimental results were compared with a volatilization model. Although the results of the solid surface describing the dependence of the concentration on the air velocity do not show a constant exponent, there was a good agreement between theoretical

and experimental values. According to the authors, these results prove the applicability of this wind tunnel for sampling on solid area sources.

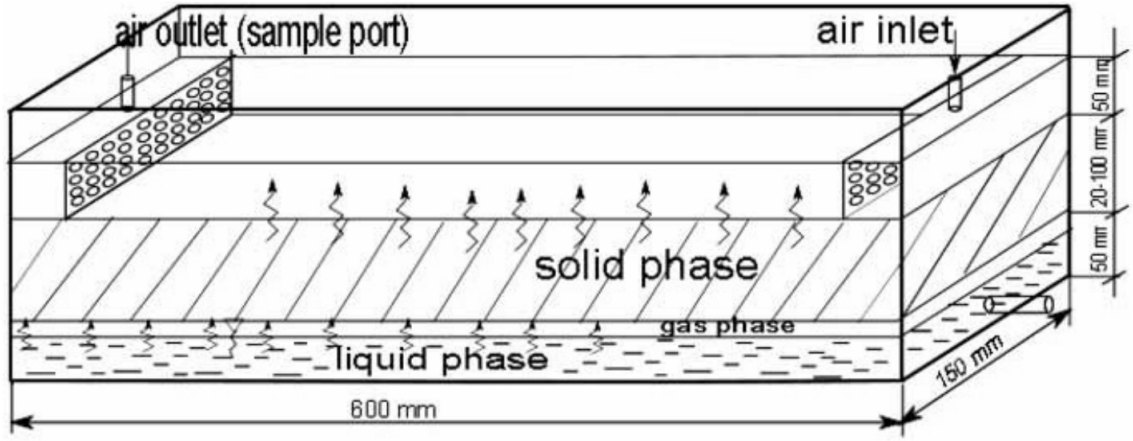

Figure 7: Scheme of the wind tunnel. From Capelli et al. (2012).

The *University of New South Wales* (UNSW) developed a wind tunnel for odor measurement on quiescent surfaces based on the recommendations of Jiang, Bliss and Schulz (1995) and Wang, Jiang and Kaye (2001). This tunnel has been studied over the years (SCHMIDT; BICUDO; JANNI, 1999; GALVIN et al., 2002; BALSARI et al., 2007; HUDSON; AYOKO, 2008b; HUDSON et al., 2009b; PRATA JR. et al., 2014; LIU et al., 2015; PERTA et al., 2016; MARTINS et al., 2018), but not all of its characteristics were investigated, motivating this study.

Jiang, Bliss and Schulz (1995) found that the original tunnel first described by Lindvall (1970) had a number of disadvantages, which could result in different odor emission rates being measured under the same operating conditions. Jiang, Bliss and Schulz (1995) added modifications to this tunnel (an extension duct, flat vanes and a perforated baffle) in order to establish a steady and repeatable flow inside the hood. The authors also defined the practical operating air velocity inside the tunnel as $0.33\ m\ s^{-1}$. However, the study was performed over smooth surface and the friction velocity (an important parameter that can be correlated with the mass transfer coefficient) was not analyzed. For this reason, the present study investigated the air flow pattern inside the tunnel, performed simulations over smooth and rough surfaces, and analyzed the friction velocity and the turbulent kinetic energy of the main flow.

3.3 The friction velocity on the atmospheric surface layer

The atmospheric boundary layer (ABL) is the region of the atmosphere that is affected by the exchanges of energy, momentum and mass between air and Earth's surface on time periods of hours. The flow at the ABL is predominantly turbulent, composed by eddies of a wide range of length and time scales; and the turbulence is generated by wind shear and thermal/buoyancy

effects. The friction velocity, u^*, characterizes the surface shear effects on the flow and is commonly used to normalize parameters close to the wall.

Coppin, Bradley and Finnigan (1994) carried out a field study of different types of flow over an isolated elongated ridge of uniform low surface roughness. The measurements were taken in the field, over grass of different heights. These experimental results of Coppin, Bradley and Finnigan (1994) were compared with the results of numerical simulation performed by Argaín, Miranda and Teixeira (2009). Argaín, Miranda and Teixeira (2009) evaluated the performance of a theoretical model in the description of the ABL over complex terrain. They observed that the friction velocity decreases significantly with increasing stability in the ABL and they found values of friction velocity varying from 0.11 $m\ s^{-1}$ to 0.19 $m\ s^{-1}$.

The friction velocity is a parameter that can be correlated with the mass transfer coefficients, since it is directly related to the turbulent transport and the shear caused by the wind on the surface (GOSTELOW, 2002). VIERS-1 Delft experiment (VAN HALSEMA et al., 1989) performed experiments with wind-wave tanks and found friction velocity values varying between 0.05 $m\ s^{-1}$ and 0.7 $m\ s^{-1}$ for wind speed (U_{10}) measured at the height Z = 10 m varying between 2.0 $m\ s^{-1}$ and 18.0 $m\ s^{-1}$. These friction velocity values presented by Argaín, Miranda and Teixeira (2009) and VIERS-1 Delft experiment (VAN HALSEMA et al., 1989) could be considered as the mean values found over rough and liquid surfaces in atmospheric flows.

The friction velocity, u^*, is an important variable for modeling emissions on quiescent surfaces at wastewater treatment plants and landfills. It can be calculated as:

$$u^* = \sqrt{\frac{\tau_0}{\rho}} \tag{3.21}$$

where τ_0 is the shear stress at the air side of the interface ($kg\ m^{-1}\ s^{-2}$), normal to the surface, and ρ is the air density.

According to Prata Jr. et al. (2017), this formulation is reasonable for most cases of interest in the current context. In the surface layer, but outside the region where the viscous dissipation effects are important, a dimensional analysis associated with physical intuitive reasoning produces the adiabatic wind speed profile as shown below:

$$\frac{u}{u^*} = \frac{1}{\kappa} \ln\left(\frac{z}{z_0}\right) \tag{3.22}$$

where z is the vertical coordinate (m) with its origin at the mean surface level, u is the mean horizontal velocity ($m\ s^{-1}$) of the flow at z height; $\kappa = 0,4$ is the Von Kármán constant (dimensionless) and z_0 is the roughness length (m).

The roughness length generally depends on the surface characteristics. A good parameter to determine whether a surface is considered rough or smooth is the roughness Reynolds number:

$$Re_r = \frac{u^* K_s}{\nu} \tag{3.23}$$

where K_s is a characteristic height of the roughness elements.

Nikuradse (1933) established a criteria that classifies the flow in three regimes: hydraulic smooth regime ($Re_r < 5$), fully rough regime ($Re_r > 70$) and transitional regime (for intermediate values of Re_r).

In the surface layer, for a smooth or a rough surface, the profile of mean wind obeys the logarithmic law (Figure 8). In an approximation used for near-wall treatment in CFD, the logarithmic profile matches the linear profile at the upper part of the viscous layer for a smooth surface. For a rough surface, there is a roughness layer formed close to the wall. The relationship between z_0 and the physical size of the roughness elements is not simple. z_0 represents the capacity of the surface in absorbing momentum, which depends on the interferences of the turbulent wakes generated by the roughness elements.

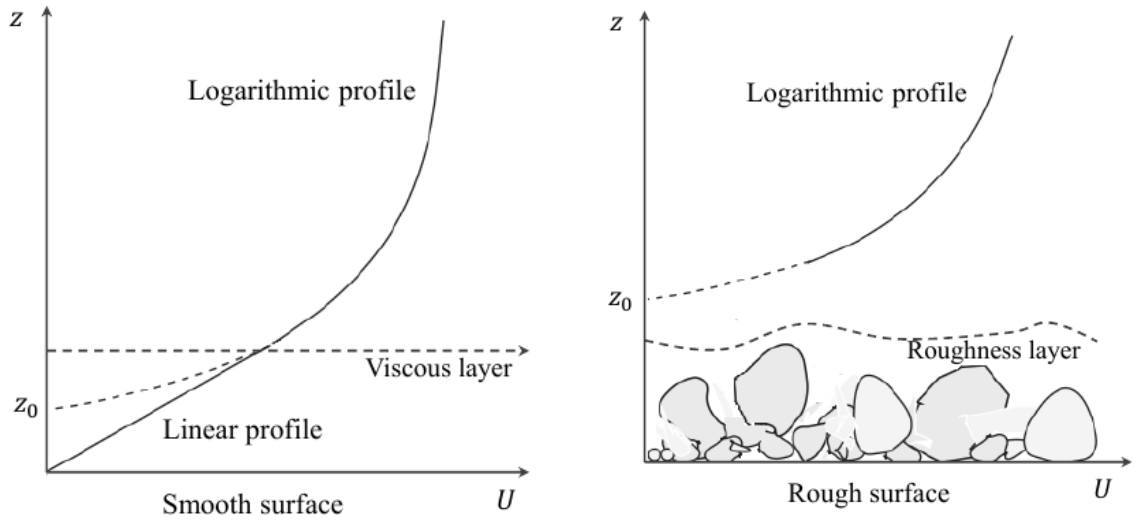

(a) (b)

Figure 8: Velocity profiles of mean wind in the surface layer over (a) a smooth surface and (b) a rough surface. From Shao (2008).

Equation 3.22 can be rewritten as:

$$\frac{u}{u^*} = \frac{1}{\kappa} \ln\left(\frac{z}{K_s}\right) + B \tag{3.24}$$

where B is the roughness function (SCHLICHTING, 1979):

$$\begin{cases} B = 5.5 + \frac{1}{\kappa} \ln \frac{k_s u^*}{\nu} & \text{for hydraulically smooth flow ,} \\ B = 8.5 & \text{for fully rough flow .} \end{cases} \tag{3.25}$$

Using equations 3.22 and 3.24, we have:

$$z_0 = \frac{K_s}{e^{B\kappa}} \, . \tag{3.26}$$

Seinfeld and Pandis (2006) present a calculation for the roughness length as a function of a characteristic height of the roughness elements, K_s, based on experimental results for atmospheric flows, according to the following ratio:

$$z_0 \approx \frac{K_s}{30} \tag{3.27}$$

For a smooth flow, z_0 is independent of the roughness element geometry and is determined only by the flow characteristics:

$$z_0 \approx \frac{\nu}{9u^*} \, . \tag{3.28}$$

4 Methodology

4.1 Configuration of interest

The configuration of the investigated portable wind tunnel is based on the wind tunnel belonging to the Núcleo de Estudos da Qualidade do Ar (NQualiAr) at the Federal University of Espírito Santo (UFES) in Brazil, and the wind tunnel of the UNSW, which were built inspired on the tunnel developed by Jiang, Bliss and Schulz (1995) and modified by Wang, Jiang and Kaye (2001). The domain is represented in Figure 9: the inlet, the extension of the air inlet duct, the expansion section, the main section, the contraction section and the outlet. The configuration investigated here does not have the flat vanes, the baffle and the outlet extension presented by Jiang, Bliss and Schulz (1995).

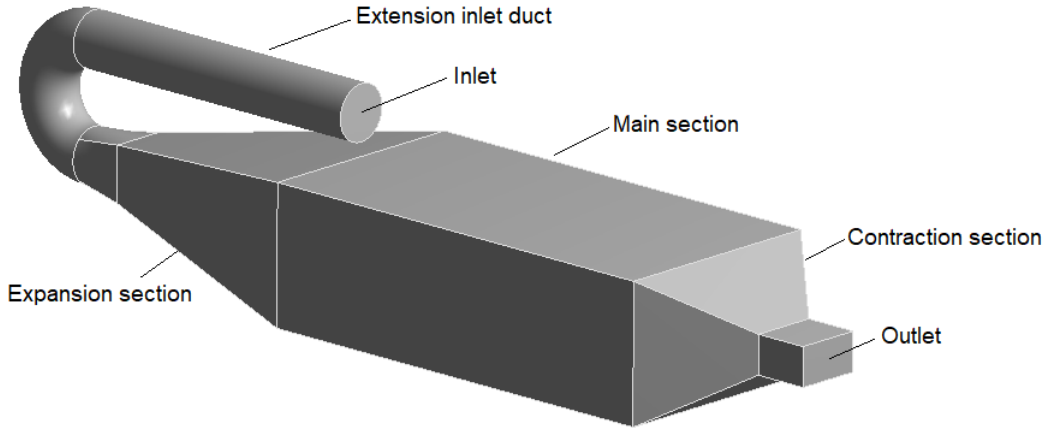

Figure 9: A 3D image of the wind tunnel.

Figure 10 shows the wind tunnel dimensions. The main section of the wind tunnel is a rectangular container with the bottom open and is $400\ mm$ wide, $800\ mm$ long and $250\ mm$ high. The air flow velocities considered at the inlet of the tunnel were $1.27\ m\ s^{-1}$, $2.55\ m\ s^{-1}$ and $3.82\ m\ s^{-1}$; that correspond to the mean velocities of $0.1\ m\ s^{-1}$, $0.2\ m\ s^{-1}$ and $0.3\ m\ s^{-1}$, respectively, in the main section of the tunnel.

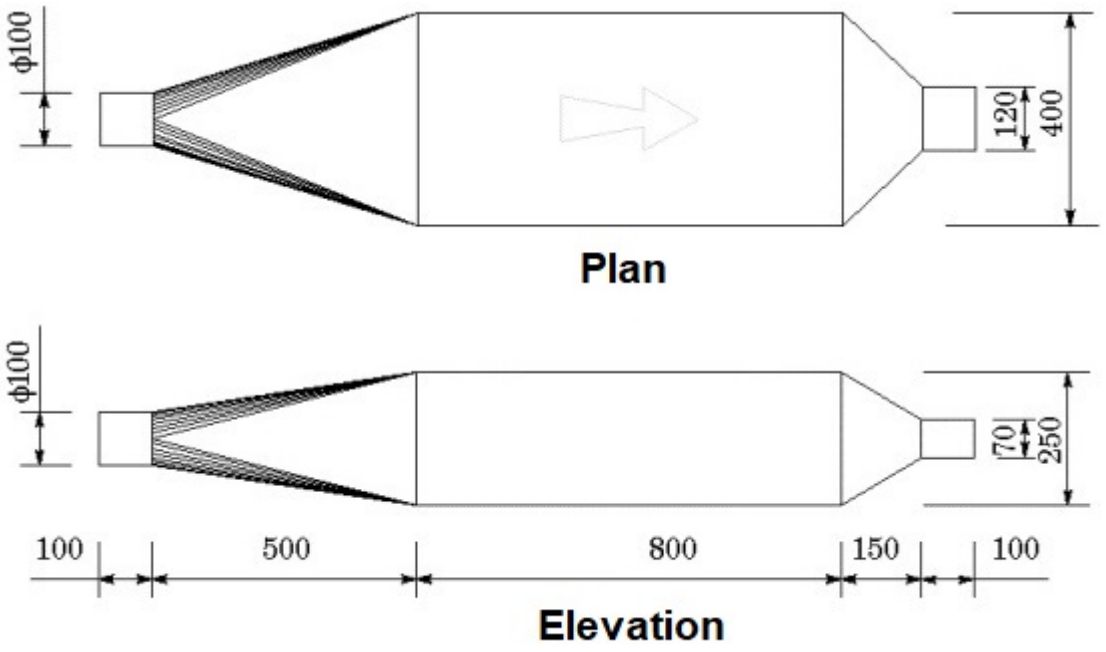

Figure 10: Wind tunnel dimensions. Image kindly provided by Dr Xinguang Wang.

The simulations were performed with four different values of roughness at the bottom surface of the tunnel with the objective to represent solid surfaces, as the ones found in landfill sites, and quiescent liquid surfaces, as the ones found in wastewater treatment plants. The roughness values were chosen according to Seinfeld and Pandis (2006), that presents roughness lengths values (z_0) for various surfaces. Applying these z_0 values to the Equation 3.27, we found the K_s values presented in Table 2.

Table 2 – Roughness height values for different surfaces.

Surface	**Roughness height (m)**
Smooth surface	K_s = 0.0
Smooth water	K_s = 0.0003
Sand	K_s = 0.003
Lawn	K_s = 0.03

4.2 Mathematical modeling

The fluid flow inside the portable wind tunnel is turbulent. Turbulence is characterized by the irregularity of the flow, the high diffusivity, the three-dimensional fluctuations of vorticity and by being a phenomenon highly dissipative. The turbulent motions range in size from the largest scales to much smaller scales as the Reynolds number increases.

Kolmogorov's theory (1941) is based on the hypothesis that kinetic energy enters the system producing large scales of motion, the so-called eddies. This energy is transferred to

smaller and smaller eddies. This transference occurs in the form of a cascade, from the largest to the smallest, until the energy is dissipated by the viscous action in the smallest eddies. The energy cascade causes turbulent flows, despite occurring at high Reynolds numbers, to have considerable energy dissipation.

Figure 11 shows the spectrum of Turbulent Kinetic Energy (TKE) as a function of the wave number, which is inversely proportional to the wavelength. The largest eddies represent about 20% of the TKE, are anisotropic and have a longer life. The inertial zone represents the largest portion of TKE in the energy spectrum. The viscous effects predominate among the smaller eddies: the smaller the wavelength, the larger the dissipation by viscous effects.

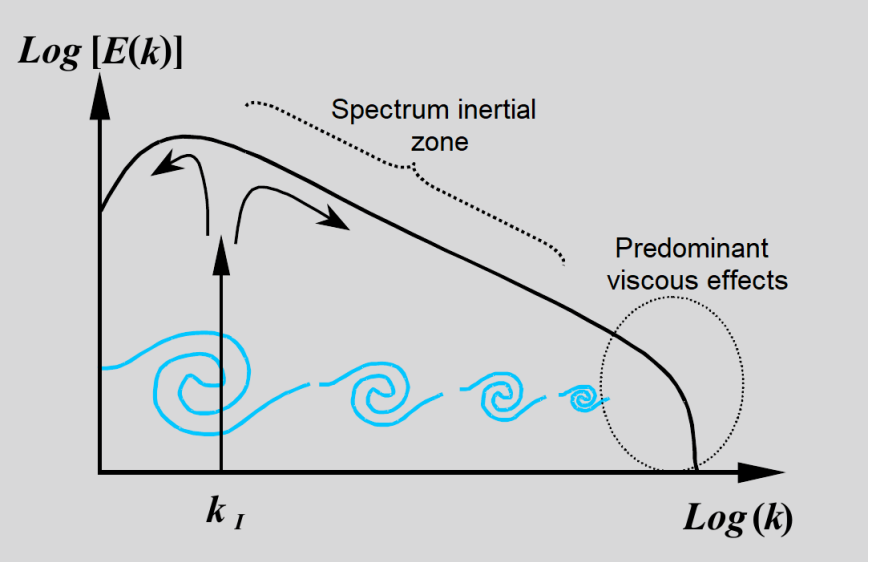

Figure 11: Turbulent kinetic energy spectrum as a function of the wave number, where E(k) is the spectral density and k is a wavenumber (m^{-1}) or a frequency (Hz) whether turbulence is considered in space or in time.

The governing laws for fluid flows, being them laminar or turbulent, are embodied in the Navier-Stokes equations. Applying the concept of Reynolds decomposition to the Navier-Stokes equations gives the equations for the mean flow variables. This decomposition proposes that the instantaneous values of the variables of the turbulent flows behave like a random variation around the average values. Thus, the average momentum conservation equation for a incompressible flow is:

$$\rho\frac{\partial\overline{u}_j}{\partial t}+\rho\overline{u}_i\frac{\partial\overline{u}_j}{\partial x_i}=-\frac{\partial\overline{p}}{\partial x_j}+\frac{\partial}{\partial x_i}(\tau_{ij}^{lam}+\tau_{ij}^{turb}) \tag{4.1}$$

where ρ is the specific mass ($kg\ m^{-3}$), $\overline{p}$ is the pressure (Pa); τ_{ij}^{lam} and τ_{ij}^{turb} are, respectively, the stresses, in Pa, due to molecular viscosity and turbulence (Reynolds stress), which are given by:

$$\tau_{ij}^{lam}=\mu\left(\frac{\partial\overline{u}_j}{\partial x_i}+\frac{\partial\overline{u}_i}{\partial x_j}\right)-\frac{2}{3}\mu\frac{\partial\overline{u}_K}{\partial x_K}\delta_{ij} \tag{4.2}$$

and

$$\tau_{ij}^{turb} = \mu_t \left(\frac{\partial \overline{u}_j}{\partial x_i} + \frac{\partial \overline{u}_i}{\partial x_j} \right) - \frac{2}{3}\mu_t \frac{\partial \overline{u}_K}{\partial x_K}\delta_{ij} - \frac{2}{3}\rho K \tag{4.3}$$

where μ is the molecular viscosity ($kg\ m^{-1}\ s^{-1}$); K is the turbulent kinetic energy ($m^2\ s^{-2}$); δ_{ij} is the Kronecker delta; and μ_t is the turbulent viscosity ($kg\ m^{-1}\ s^{-1}$), *i*, *j* and *k* are the direction index of Einstein's notation.

In addition, applying the decomposition in the continuity equation, it can be expressed as:

$$\frac{\partial \overline{u}_i}{\partial x_i} = 0 \tag{4.4}$$

where $\overline{u}_i$ is the velocity ($m\ s^{-1}$).

These are known as the Reynolds Average Navier-Stokes equations (RANS). The RANS equations are defined by a set of averages of the Navier-Stokes and the continuity equations in which the statistical quantities of interest are mean values over all length scales. The intend of these equations is to know the average flow and the effects of turbulence on the properties of the average flow.

The decomposition of the Navier-Stokes equations causes the appearance of terms of second order or more, which involves fluctuations. After the decomposition, there are more variables than equations, which is called the closure problem. Consequently, the equations cannot be solved. So, it is necessary to develop turbulence models to estimate Reynolds stress and close the system of equations.

A common way to model Reynolds stress is using the Boussinesq's analogy. Boussinesq, in 1877, proposed that the transport of momentum in the molecular and the turbulent levels occur in an analogous way. The turbulent stress would be related to the mean velocity gradient through a viscosity associated with the fluid, the flow characteristics and the geometry of the problem. This implies that the normal components of the Reynolds stress are isotropic. Thus, the turbulent viscosity (μ_t) should be calculated instead of the Reynolds stress components. To determine μ_t, there are several models with different numbers of transport equations, besides the RANS equations.

These are first order models based in the analogy between the laminar and the turbulent flow, also called models of turbulent viscosity. There are also second order models, which use directly the governing equations to the second-order terms instead of using Boussinesq's hypothesis. These models are used in computational programs to solve the closure problem. And, therefore, in the present work, a first order closure model is used.

4.3 Turbulence treatment

Most current engineering approaches, even for the prediction of unsteady flows, are based on the solution of RANS equations. The turbulence models used to solve the RANS equations

define the whole spectrum of turbulent motions (KAPADIA et al., 2004). The attention is focused on the mean values of the variables in the RANS turbulence models. The extra terms that appear in the equations for the mean flow are modeled by the Boussinesq analogy and the turbulent viscosity by means of turbulence classical models: among the best known are the $K-\varepsilon$ and the $K-\omega$ models (VERSTEEG; MALALASEKERA, 2007).

The standard $K-\varepsilon$ model presents two equations: one for K (turbulent kinetic energy) and one for ε (turbulent kinetic energy dissipation rate). The $K-\varepsilon$ model presents many limitations in the region close to the wall, leading to the representation of flows subject to adverse pressure gradients, resulting in an overestimation of the shear stress. The not good treatment near the wall make it necessary to use wall functions. The ε is not the only possible determinant variable of the length scale. Another alternative is the $K-\omega$ model proposed by Wilcox (1988, 1993a, b, 1994), which uses the turbulence frequency $\omega = \varepsilon/K$ (dimension s^{-1}) as the second variable (VERSTEEG; MALALASEKERA, 2007).

The $K-\omega$ model is attractive because the integration with the wall does not require specific functions in low Reynolds number applications. The value of the turbulent kinetic energy on the wall is considered zero. The frequency, ω, tends to infinite on the wall, but it is possible to specify a very high value for it (VERSTEEG; MALALASEKERA, 2007). As Wilcox (1993b) described in details, the $K-\omega$ model is superior in the treatment of the viscous near-wall region for boundary-layer flows, but presents a poor performance in the free flow.

Menter (1992) proposed a hybrid model using $K-\varepsilon$ and $K-\omega$, the $K-\omega$ SST (*Shear Stress Transport*) model. In the regions close to the wall, the $K-\omega$ model is used, and in the regions far from the wall (regions of free flow), the $K-\varepsilon$ is inserted into the specific dissipation rate equation. The $K-\omega$ SST model was designed to give greater precision to the predictions of flow separation under adverse pressure gradients, including the introduced turbulent viscosity transport effects.

The turbulent viscosity is expressed as:

$$\mu_t = \frac{a_1 K}{\max(a_1\omega, SF_2)} \tag{4.5}$$

The turbulent kinetic energy, K, and the specific dissipation rate, ω, are obtained from the following transport equations:

$$\frac{\partial K}{\partial t} + \overline{u}_j \frac{\partial K}{\partial x_j} = P_K - \beta^* K\omega Y_K + \frac{\partial}{\partial x_j}\left[(\nu + \sigma_k \mu_t)\frac{\partial K}{\partial x_j}\right] \tag{4.6}$$

and

$$\frac{\partial(\omega)}{\partial t} + \overline{u}_j \frac{\partial \omega}{\partial x_j} = \alpha S^2 - \beta\omega^2 + \frac{\partial}{\partial x_j}\left[(\nu + \sigma_\omega \mu_t)\frac{\partial \omega}{\partial x_j}\right] + 2(1-F_1)\sigma_{\omega 2}\frac{1}{\omega}\frac{\partial K}{\partial x_i}\frac{\partial \omega}{\partial x_i} \tag{4.7}$$

where P_k is the production of turbulent kinetic energy due to shear stress ($N\ m^{-2}\ s$); ν is the kinematic viscosity of the fluid ($m^2\ s^{-2}$); *S* is the deformation tensor (s^{-1}); α, β^* e β are empirical constants.

And the coefficients and auxiliary relations are given by:

$$F_2 = \tanh\left[\left[\max\left(\frac{2\sqrt{K}}{\beta^*\omega y}, \frac{500\nu}{y^2\omega}\right)\right]^2\right] \tag{4.8}$$

$$P_K = \min\left(\tau_{ij}\frac{\delta U_i}{\partial x_j}, 10\beta^* K y\right) \tag{4.9}$$

$$F_1 = \tanh\left\{\left\{\min\left[\max\left(\frac{2\sqrt{K}}{\beta^*\omega y}, \frac{500\nu}{y^2\omega}\right), \frac{4\sigma_{\omega 2}K}{CD_{K\omega}y^2}\right]\right\}^4\right\} \tag{4.10}$$

In this model, ω can be defined as:

$$\omega = \frac{K^{\frac{1}{2}}}{C_\mu{}^{\frac{1}{4}}\kappa z} \tag{4.11}$$

where C_μ is a constant, κ is the Von Kármán constant (dimensionless) and z is the domain height.

Therefore, the $K-\omega$ SST model was chosen to simulate the flow inside the wind tunnel. As $K-\omega$ SST does not present wall functions, it is necessary to have a very good treatment near the wall when performing the simulations. It requires accurate results of the flow field calculated over the near wall region. The distance from the wall measured in viscous lengths is denoted by:

$$y^+ = \frac{u^* d}{\nu} \tag{4.12}$$

where u^* is the friction velocity ($m\ s^{-1}$) at the nearest wall and d is the distance (m) to the nearest wall.

y^+ can be correlated with u^+, that is:

$$u^+ = \frac{u}{u^*} \tag{4.13}$$

The y^+ is expected to determine the relative importance of viscous and turbulent processes (POPE, 2000). Figure 12 presents the chart correlating the wall variables u^+ and y^+. As y^+ increases, the u^+ profile presents different regions, or layers, in the near-wall flow. In the region $y^+ < 5$ the flow is partially, but not completely, laminar. This region is called the *viscous sublayer* and the Reynolds shear stress is negligible compared with the viscous stress. The relation between u^+ and y^+ has a form of a linear law $u^+ = y^+$ in the *viscous sublayer*. The adjoining region, $5 < y^+ < 40$, is called the *buffer layer* (DAVIDSON, 2009). In the *buffer layer*, there is a direct effect of molecular viscosity on the shear stress; whereas, conversely, in the *outer layer* and the *log-law of the wall region* the direct effect of viscosity is negligible (POPE, 2000).

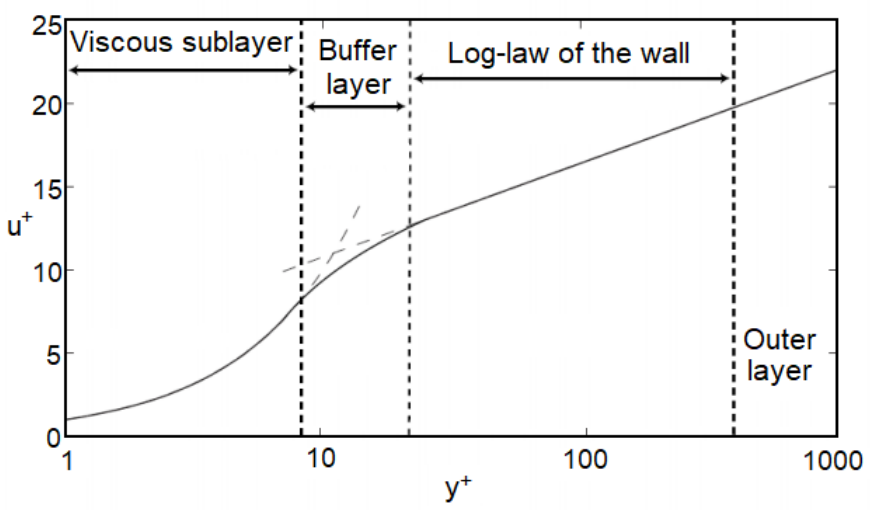

Figure 12: Chart correlating u^+ and y^+. Adapted from Davidson (2009).

4.4 Boundary conditions

A uniform air velocity profile with values of 1.27 $m\ s^{-1}$, 2.55 $m\ s^{-1}$ and 3.82 $m\ s^{-1}$ was set at the inlet, which corresponds to the mean velocities (over the cross section area) of 0.1 $m\ s^{-1}$, 0.2 $m\ s^{-1}$ and 0.3 $m\ s^{-1}$ in the main section of the tunnel. The air entering the domain was considered completely clean. Also at the tunnel's inlet, boundary conditions for the turbulent kinetic energy (K) and the specific dissipation rate (ω) were set. The turbulent kinetic energy was calculated based on the mean flow velocity ($\overline{u}$) and the turbulence intensity (I). The turbulence intensity considered in the simulations was 5%, which is the Fluent's default. The specific dissipation rate was calculated as showed before in Equation 4.11.

Simulations were performed with three rough surfaces and one surface completely smooth (using the velocity of 3.82 $m\ s^{-1}$ at the inlet) with the objective to represent the different surfaces encountered on wastewater treatment plants and landfills. The values are (in meters): 0.03, 0.003, 0.0003 and 0.0. The roughness value was inserted into *Fluent* as a condition that changes the wall function to the liquid/solid-gas interface (bottom surface of the main section of the wind tunnel).

Wall boundary conditions are used to bound fluid and solid regions. In *Fluent*, the no slip boundary condition is applied at walls by default in viscous flows. The no slip condition indicates that the fluid attaches to the wall and moves with the same velocity as the wall, if it is moving. For this study, it was considered a stationary wall, with no slip condition and different values for roughness.

On the wall boundary condition set up on *Fluent*, roughness is treated as sand-grain roughness. Figure 13 shows the equivalent sand-grain roughness using a wall with a layer of close spheres, which have an average roughness height representing a technical roughness with

peaks and valleys of different shapes and sizes (ANSYS, 2019).

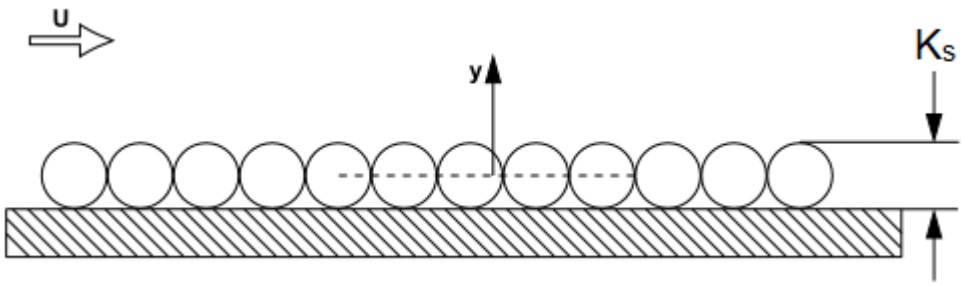

Figure 13: Illustration of equivalent sand-grain roughness, with U being the flow velocity and K_s being the roughness height.

To model the wall roughness effects, it is necessary to define two roughness parameters on *Fluent*: the Roughness Height, K_s, and the Roughness Constant, C_s. The default for roughness height is zero, which corresponds to smooth walls. It is necessary to specify a nonzero value for K_s for the roughness to take effect. For a uniform sand-grain roughness, the height of the sand-grain can simply be taken for K_s (ANSYS, 2019).

The value of the roughness constant depends on the type of the given roughness. The default for roughness constant is $C_s = 0.5$, which represents a uniform sand-grain roughness. The default value of the roughness constant was chosen when running the simulations.

On the wind tunnel walls, conditions of impermeability (null normal velocity) and no slip (null tangential velocity) were adopted. For the liquid/solid-gas interface, the conditions of impermeability (there is no air flow through the interface) and no slip (as an approximation of the resistance that the rough surface imposes on the air flow) were also adopted. A gauge pressure of 0 Pa at the exit of the wind tunnel was considered, since it is open to the atmosphere. Table 3 summarizes the boundary conditions adopted.

Table 3 – Boundary conditions.

Location	**Boundary condition**
Entry	$\overline{u}$ = 1.27 $m\ s^{-1}$
	$\overline{u}$ = 2.55 $m\ s^{-1}$
	$\overline{u}$ = 3.82 $m\ s^{-1}$
	$K = \frac{1}{2}\ (\overline{u}\ I)^2$
	$\omega = \frac{K^{\frac{1}{2}}}{C_\mu{}^{\frac{1}{4}} \kappa z}$
Exit	P = 0 Pa
Wall tunnels	$\overline{u}_1 = \overline{u}_2 = \overline{u}_3 = 0$
Liquid-gas interface	$\overline{u}_1 = \overline{u}_2 = \overline{u}_3 = 0$
Solid-gas interface	$\overline{u}_1 = \overline{u}_2 = \overline{u}_3 = 0$

Notes: P is the gauge pressure; 1, 2 and 3, indicate the directions of the coordinated axes X, Y and Z, respectively; $\overline{u}$ represents the inlet air velocity in the domain.

4.5 Numerical solution

The program *Ansys Fluent*, version 19.1, was used for the computational numerical solution of the conservation equations, which is based on the finite volume method. The finite volume method is used mainly for the numerical solution of problems in fluid mechanics (SCHÄFER, 2006).

According to Schäfer (2006), in general, the volume finite method involves the following steps:

- Decomposition of the domain problem in control volumes;
- Formulation of integral equilibrium equations for each control volume;
- Approximation of integrals by numerical integration;
- Approximation of function values and derivatives by interpolation with nodal values;
- Assembly and solution of the discrete algebraic system.

The objective of any discretization practice is to transform one or more partial differential equations into a corresponding system of algebraic equations. The solution of this system produces a set of values that correspond to the solution of the original equations in some

predetermined places in space and time, as long as certain conditions are satisfied (JASAK, 1996).

In the finite volume method the space is divided into a finite number of discrete regions, called control volumes or cells. The discretization determines the positions of points in space and time in which the solution is found (JASAK, 1996). There is a computational node at the center of each control volume in which the values of the variables must be calculated. Interpolation is used to express the variables values on the surface of the control volume in terms of the nodal values. Surface and volume integrals are approximated using suitable quadrature formulas. As consequence, an algebraic equation is obtained for each control volume, in which a number of neighboring nodal values appear (FERZIGER; PERIC, 2001).

The continuity, momentum and turbulence equations were solved considering the air as isothermal Newtonian fluid (temperature of 25º C) and considering transient regime, where a period of 60 seconds was simulated. Many attempts to simulate a steady state were performed, but none of them achieved the convergence criteria adopted. On the contrary, the transient simulation achieved the convergence criteria efficiently. The configuration of time step adaptive was used to determine the size of the time interval. With this option, there is no specification of a time step, but a range in which it must be contained (0.0025 to 0.01 s). Thus, the initial time step ($0.0025\ s$) adapts so that the simulation remains stable. The value of 10^{-6} was adopted as the solution convergence limit for the square root of the average of the squares of the residuals in each cell of the domain (root mean square – RMS).

The pressure-velocity coupling method used was the SIMPLE. In relation to the spacial discretization, the second order upwind scheme was used for interpolations of the convective terms of the equations of momentum, turbulent kinetic energy and specific dissipation rate of the turbulent kinetic energy. Gradients were calculated with the least squares cell-based method and the pressure terms were calculated with second-order approximation. The temporal interpolation scheme used was the first order implicit. The solution methods used are listed in Table 4.

Table 4 – Solution methods.

Pressure-velocity coupling	**Spacial discretization**	
Scheme SIMPLE	Gradient	Least squares cell-based
	Pressure	Second order
	Momentum	Second order upwind
	Turbulent Kinetic energy	Second order upwind
	Specific dissipation rate	Second order upwind

4.6 Meshing sensitivity test

The domain must be discretized to solve the set of equations that represent the problem. Such discretization results in a mesh that stores the address of each point at which the equations are solved. For these purposes, the program *Meshing* of the package *Ansys* 19.1 was used. The domain was discretized into a non structured and non uniform mesh, with tetrahedral and prismatic volume elements. Appendix A presents the meshing sensitivity test that verified the independence of the results to the size of the computational coarse, medium and fine meshes. The results are presented with the coarse mesh (approximately 1.7 million elements) because it requires less computational effort.

On the wall region, the mesh was refined using an option on *Meshing* called *inflation*. The volume elements are generated by a succession of straight lines parallel to the chosen face, having certain thickness and amount until they join the tetrahedral mesh. The construction of this portion of prisms allows the generated elements to have their faces perpendicular and/or parallel to the main direction of the flow, thus, a greater number of nodes is observed in regions where large gradients are observed. The option *Face Sizing* was also used in order to control the mesh growth and distribution. With this option, it is possible to make the mesh more refined on the walls (region of interest) and less refined on the center of the tunnel. Figure 14 shows details of the mesh.

In order to obtain more accurate results, it is important that $y^+ < 5$ in the near wall region. At the tunnel's bottom surface, the mean values of y^+ are; for coarse, medium and fine meshes, respectively; 4.12, 4.13 and 4.14.

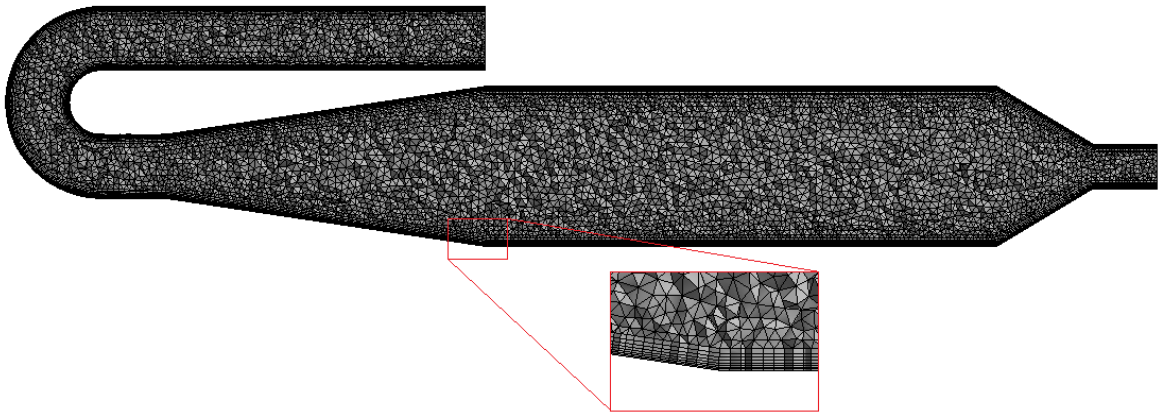

Figure 14: A closer view of the coarse mesh.

4.7 Experimental validation

In order to make sure that the phenomena are correctly described, model validation is necessary before further investigating the influence of the roughness length on the fluid flow

patterns. The experimental data published by Jiang, Bliss and Schulz (1995) and Wu (2007) were used for the model validation in this work. These authors performed experimental tests using the same tunnel. However, Wu (2007) used a baffle in the beginning of the main section, while Jiang, Bliss and Schulz (1995) did not. Jiang, Bliss and Schulz (1995) considered the mean velocity of $0.33\ m\ s^{-1}$ to perform the experiments. Although Jiang, Bliss and Schulz (1995) did not make it clear where this velocity was estimated, it was assumed as the mean velocity passing through the center point of the main section of the tunnel. Wu (2007) considered an inlet velocity of $3.81\ m\ s^{-1}$, which corresponds to the mean velocity of $0.3\ m\ s^{-1}$ in the main section of the tunnel. They both used hot wire anemometers to measure the air velocity inside the tunnel and performed the sampling following the same methodology. Neither of them was clear about the amount of tests that were done.

The measurements were conducted at the positions $x = 0.2\ m$, $x = 0.4\ m$ and $x = 0.6\ m$ in the tunnel's length in order to measure the velocity values with an anemometer. Each cross-section had 8 sampling ports 50 mm apart (Figure 15a). At each sampling port, the velocity was measured at 5 vertical positions. Therefore, each cross-section was divided in 40 sampling points equally distributed: 5 vertical and 8 horizontal positions (Figure 15b).

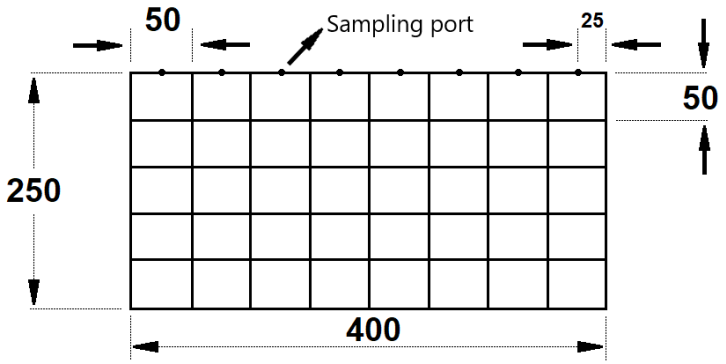

(a) Frontal view of the cross-section (with measurements in mm).

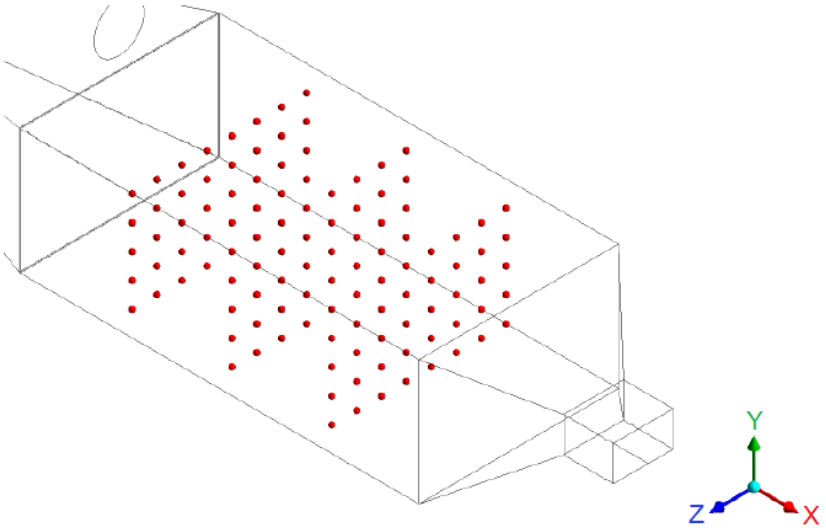

(b) The sampling points in the three cross-sections.

Figure 15: Schematic view of the sampling points.

Both Jiang, Bliss and Schulz (1995) and Wu (2007) presented two velocity distributions: horizontal and vertical. It is important to notice that the hot wire anemometer only measures the air velocity at one direction, then, it only gives positive values. Considering the position the authors sampled using the sampling ports, it's possible to conclude they obtained positive values of the velocity component u. They distributed these data in horizontal and vertical profiles. The horizontal distribution was produced by averaging the measured velocities at the 5 different heights for each horizontal position. Then, for the vertical distribution, the velocities at the 8 horizontal positions were averaged for each height. The numerical results obtained in the present work were presented in the same manner.

5 Results

5.1 Validation of the numerical simulations

In order to validate the numerical simulations, the results obtained were compared to the experimental data of Jiang, Bliss and Schulz (1995) and Wu (2007). The velocity profiles were sampled according to the methodology presented in section 4.7. Figures 16 and 17 present the numerical results compared to the experimental data. The numerical simulations presented here were performed with no-slip condition and uniform inlet velocity of 3.82 $m\ s^{-1}$, which corresponds to the mean velocity of 0.3 $m\ s^{-1}$ in the main section of the tunnel. As previously stated in section 4.7, it is possible to conclude that the experimental tests obtained only positive values of the velocity component *u*. The numerical data presented negative velocity values due to the recirculation zone on the main section of the tunnel. Because of this, the modulus of the velocity component *u* was chosen to be the most appropriate to be compared to the experimental data.

First of all, to perform the numerical simulations, the bottom surface of the tunnel was considered to be quiescent, therefore, the smooth surface ($K_s = 0\ m$) was used. The comparison of these results to the experimental data showed a poor agreement. Given that, a new hypothesis was considered. Since air is blown into the tunnel and passes over the liquid surface, it might have caused the formation of waves on the experimental tests. Once waves exist on the liquid surface, it cannot be considered a quiescent surface anymore. Therefore, the surface become a rough surface instead of smooth. Based on this consideration, the experimental data were then compared to the simulations with different values of roughness in the bottom surface of the main section of the tunnel. The values of roughness considered were $K_s = 0.03\ m$, $K_s = 0.003\ m$ and $K_s = 0.0003\ m$. Yet, a good agreement was also not observed.

Possibly, the reason for this difference between numerical and experimental values is due to the inlet boundary condition adopted (uniform inlet velocity). The uniform velocity profile adopted may not completely represent the velocity distribution entering the tunnel in the experiments. The fan and the tunnel are connected by a flexible duct. Probably, the air velocity profile suffers an influence of this flexible conduction tube (which is not represented in the present simulation) before entering the tunnel. The asymmetric profiles seen in the experimental results (which are not expected given that geometry is symmetrical) might be the result of a non-uniform velocity distribution arriving at the main section. Therefore, the uniform velocity profile is an idealized condition, which may not occur in real situations.

The objective of the validation is to indicate if the numerical results and the modelling process are capable of reproducing a practical situation of the studied problem. However, experimental validation of CFD studies concerning enclosure sampling devices faces a problem as the number of works found in the literature detailing experimental results that could be used for validation is reduced. In order to obtain numerical results as close to reality as possible, it would be necessary to obtain more experimental details not revealed by Jiang, Bliss and Schulz (1995) and Wu (2007). Essential information like the number of samples taken, the measured velocity arriving at the inlet of the tunnel, the detailed sampling process and the inlet conditions were not reported. Above all, it is believed that the type of anemometer used in Jiang, Bliss and Schulz (1995) and Wu (2007) experimental work was not suitable for the flow inside the main section of the wind tunnel as it presents recirculation in all its extension and, therefore, the flow is never aligned with the hot wire causing a possible mismeasurement higher than the actual values of the component u of velocity. Nevertheless, no other references were found in the literature presenting suitable experimental data for the comparison, and therefore, it was decided to present the comparison with Jiang, Bliss and Schulz (1995) and Wu (2007) data regardless the poor agreement. It is believed that these results can help promote the idea that is it necessary to carry out experimental work concerning the measurements of the flow structure inside the wind tunnel. It is also important to state here that grid sensitivity tests were performed as described in section 4.6 and presented in Appendix A, which proves that the numerical solution was performed correctly. Also, the convergence criteria for all equations were reached by using the transient simulation technique as described in section 4.5. It leaves open questions on the mathematical modelling mainly about the adopted boundary conditions as it is believed based on evidences from the literature that the turbulence model chosen to represent the turbulence effects on the flow ($K-\omega$ SST) is suitable for the type of flow investigated in the present work. However, the idea of using a more sophisticated turbulence model such as Large Eddy Simulation is promoted in this work as a recommendation for future investigation.

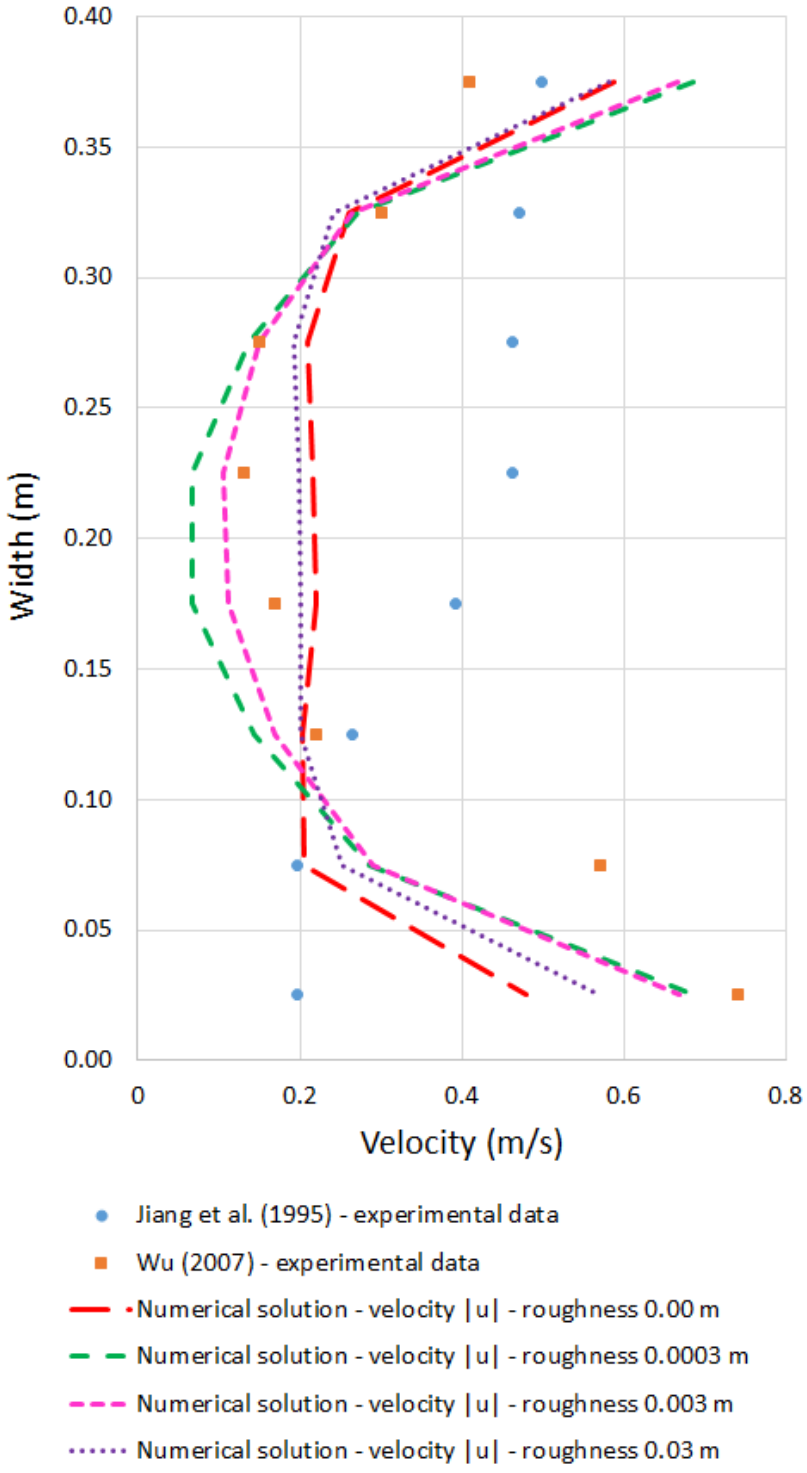
0.40
0.35
0.30
0.25
0.20
0.15
0.10
0.05
0.00
Width (m)
0
0.2
0.4
0.6
0.8
Velocity (m/s)
Jiang et al. (1995) - experimental data
Wu (2007) - experimental data
Numerical solution - velocity |u| - roughness 0.00 m
Numerical solution - velocity |u| - roughness 0.0003 m
Numerical solution - velocity |u| - roughness 0.003 m
Numerical solution - velocity |u| - roughness 0.03 m

(a) x = 0.2 m

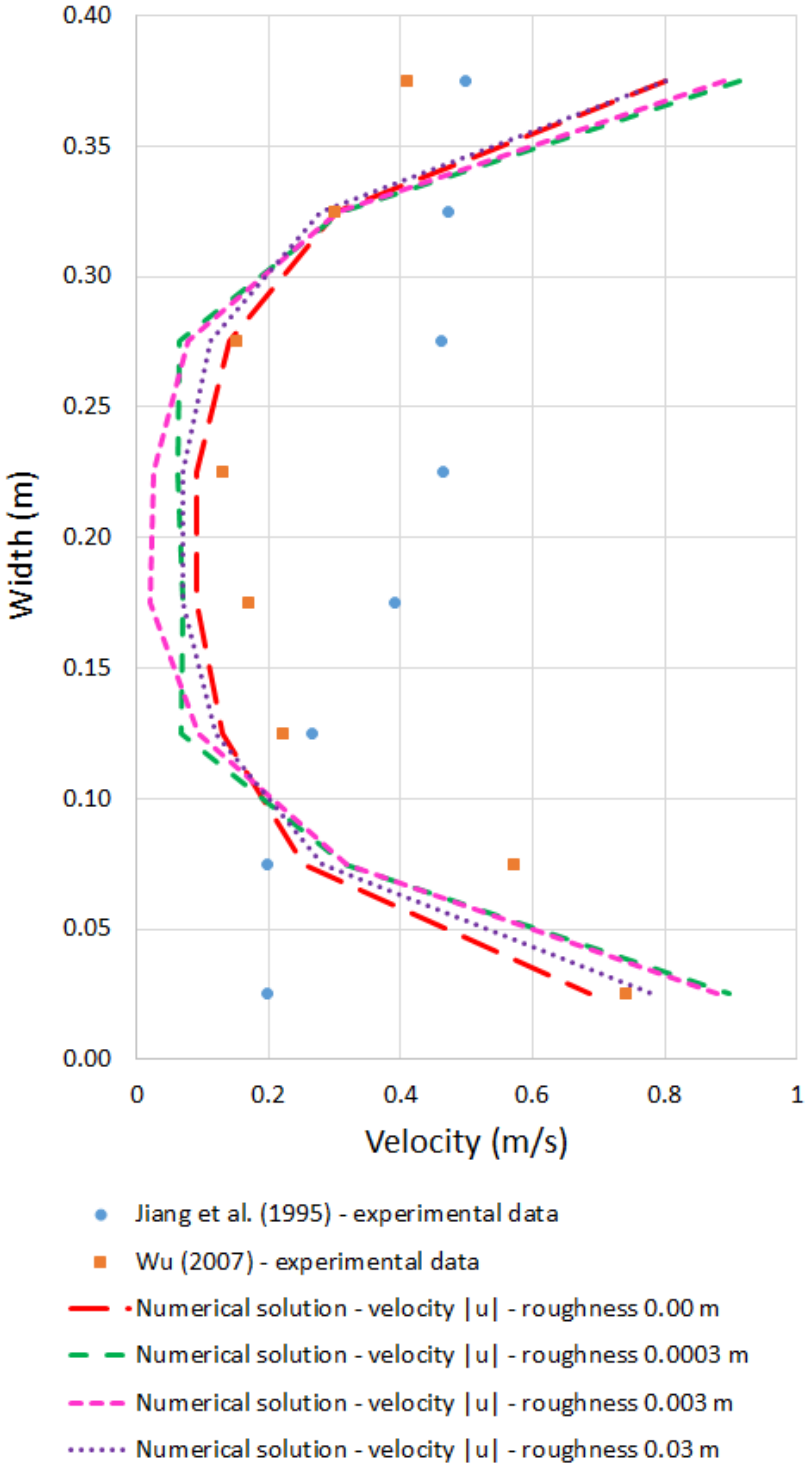
0.40
0.35
0.30
0.25
0.20
0.15
0.10
0.05
0.00
Width (m)
0
0.2
0.4
0.6
0.8
1
Velocity (m/s)
Jiang et al. (1995) - experimental data
Wu (2007) - experimental data
Numerical solution - velocity |u| - roughness 0.00 m
Numerical solution - velocity |u| - roughness 0.0003 m
Numerical solution - velocity |u| - roughness 0.003 m
Numerical solution - velocity |u| - roughness 0.03 m

(b) x = 0.4 m

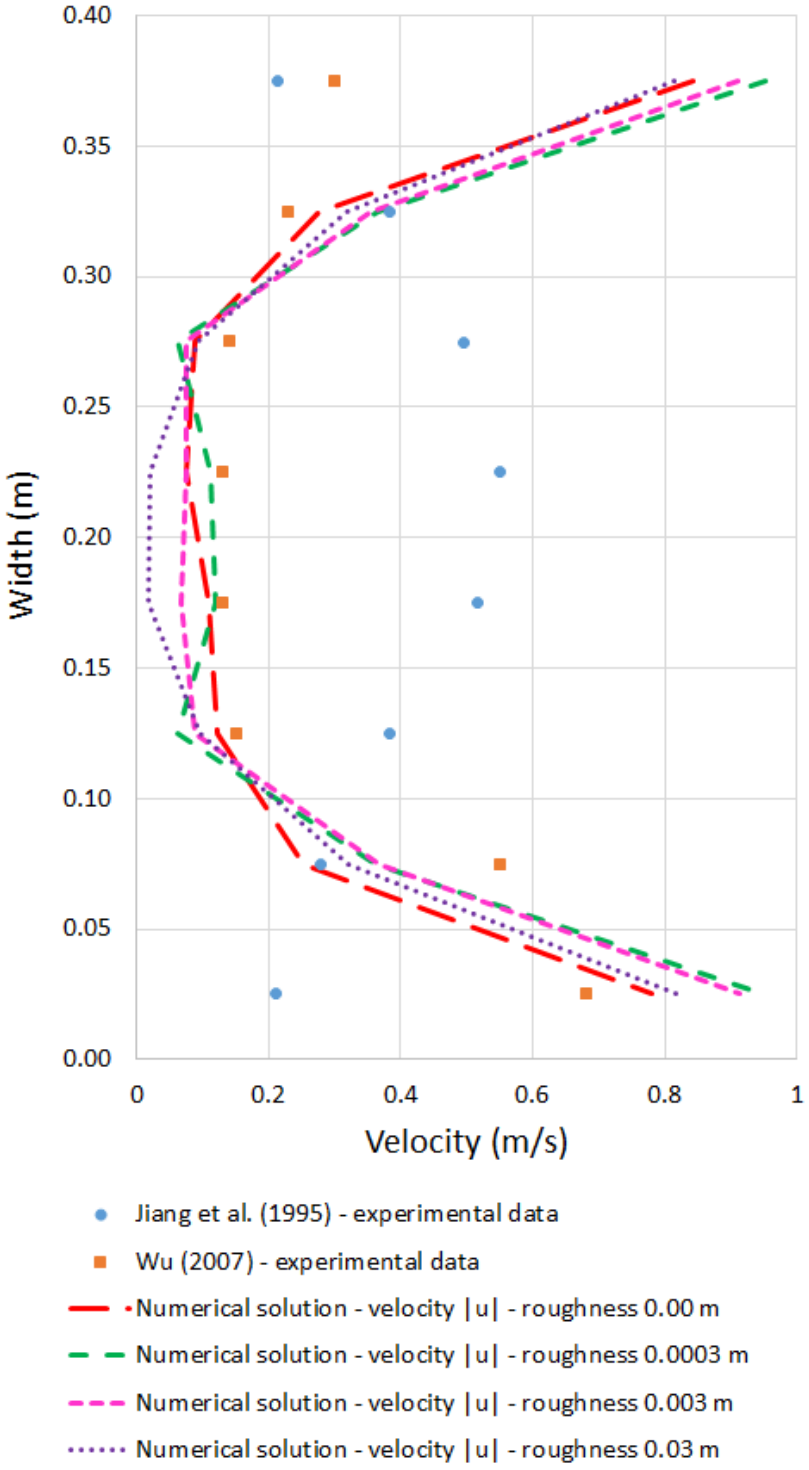

(c) x = 0.6 m

Figure 16: Horizontal velocity distribution at positions (a) x = 0.2 m, (b) x = 0.4 m and (c) x = 0.6 m.

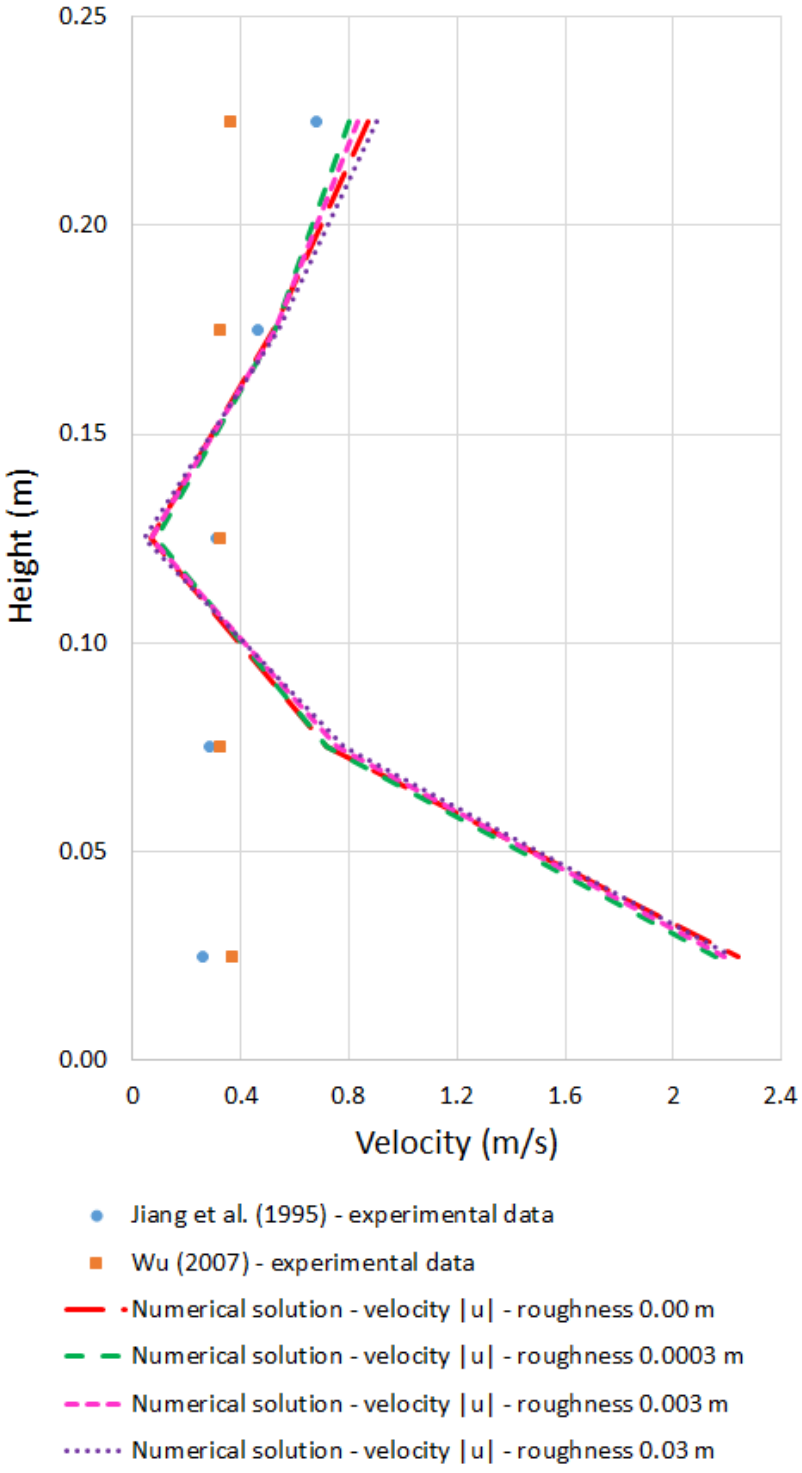
0.25
0.20
0.15
0.10
0.05
0.00
Height (m)
0
0.4
0.8
1.2
1.6
2
2.4
Velocity (m/s)
Jiang et al. (1995) - experimental data
Wu (2007) - experimental data
Numerical solution - velocity |u| - roughness 0.00 m
Numerical solution - velocity |u| - roughness 0.0003 m
Numerical solution - velocity |u| - roughness 0.003 m
Numerical solution - velocity |u| - roughness 0.03 m

(a) x = 0.2 m

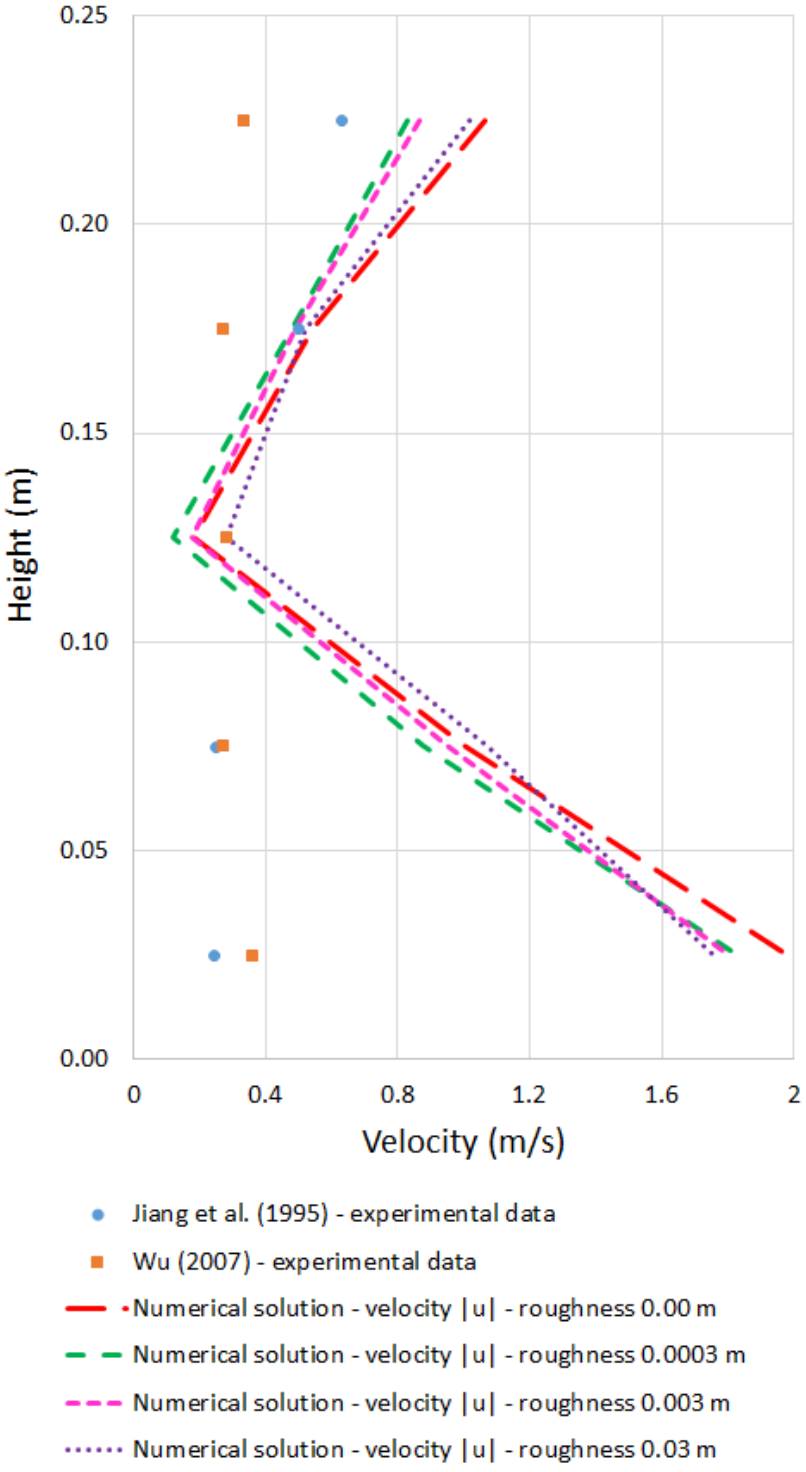
0.25
0.20
0.15
0.10
0.05
0.00
Height (m)
0
0.4
0.8
1.2
1.6
2
Velocity (m/s)
Jiang et al. (1995) - experimental data
Wu (2007) - experimental data
Numerical solution - velocity |u| - roughness 0.00 m
Numerical solution - velocity |u| - roughness 0.0003 m
Numerical solution - velocity |u| - roughness 0.003 m
Numerical solution - velocity |u| - roughness 0.03 m

(b) x = 0.4 m

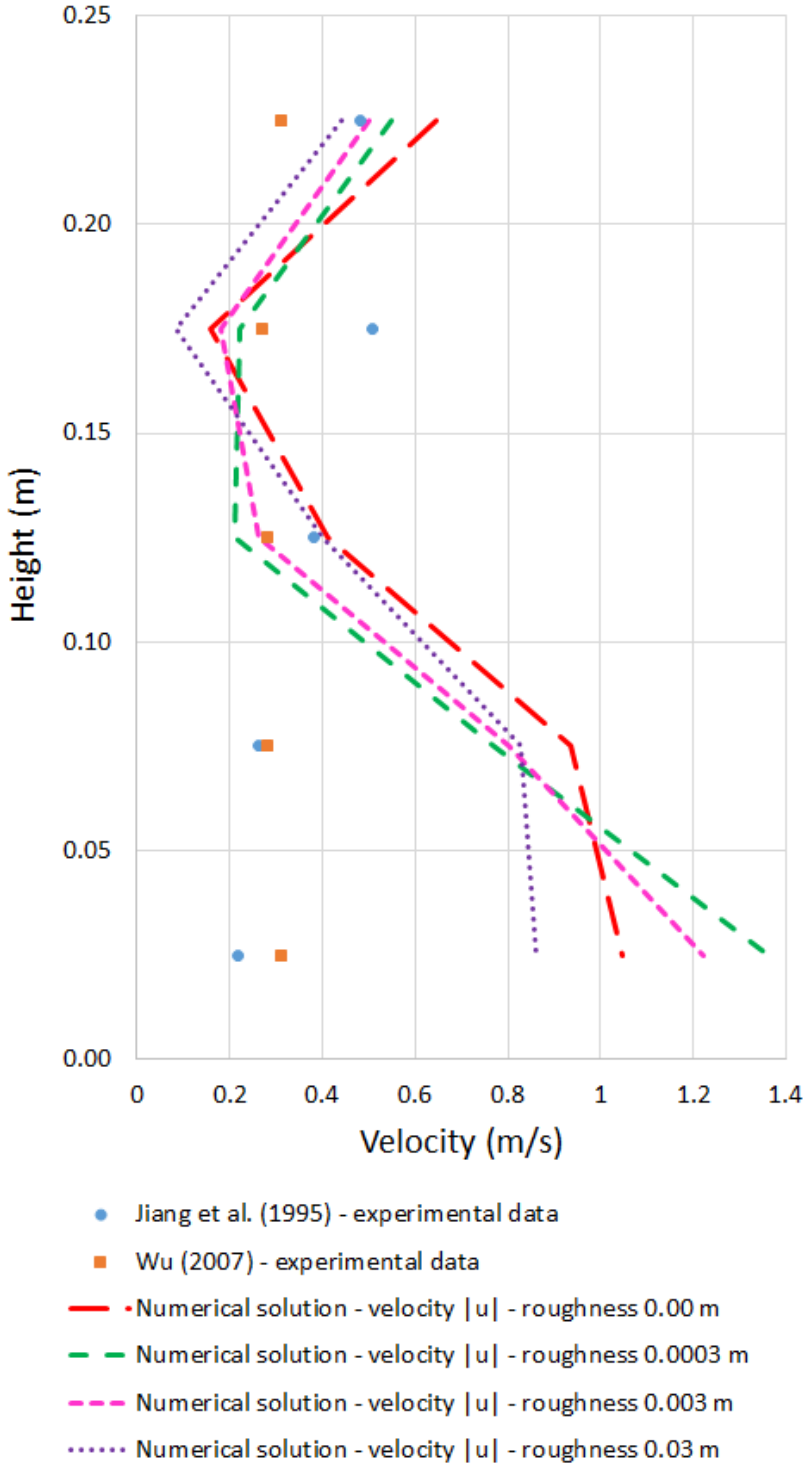

(c) x = 0.6 m

Figure 17: Vertical velocity distribution at positions (a) x = 0.2 m, (b) x = 0.4 m and (c) x = 0.6 m.

5.2 Analysis of the flow patterns inside the tunnel

A numerical simulation was performed with the objective to analyze the flow behavior inside the tunnel. The velocity profiles and vectors exhibited here correspond to a simulation with smooth surface ($K_s = 0\ m$), no-slip condition and uniform inlet velocity of $3.82\ m\ s^{-1}$, which corresponds to the average velocity of $0.3\ m\ s^{-1}$ in the center of the tunnel. The data was analyzed based on profiles of the velocity components (*u*, *v* and *w*), sampled on seven vertical lines inside the tunnel's main section, with 150 sampling points at each line. Figure 18 shows the seven positions sampled: 1 ($x = 0.2\ m$, $z = 0.1\ m$), 2 ($x = 0.2\ m$, $z = 0.3\ m$), 3 ($x = 0.4\ m$, $z = 0.1\ m$), 4 ($x = 0.4\ m$, $z = 0.2\ m$), 5 ($x = 0.4\ m$, $z = 0.3\ m$), 6 ($x = 0.6\ m$, $z = 0.1\ m$) and 7 ($x = 0.6\ m$, $z = 0.3\ m$). Figure 19 shows the velocity profiles inside the wind tunnel.

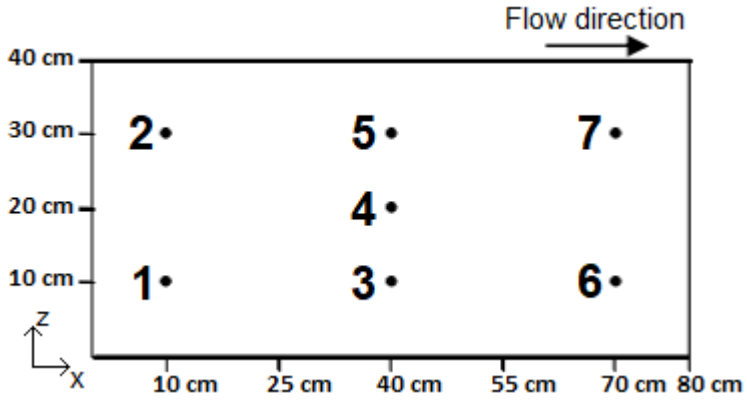

Figure 18: The upper view of the tunnel's main section showing the positions where the velocity was sampled.

For all the sampled positions, there is a non-uniformity on the profile of velocity component *u*. There are negative values at the top of the profile, indicating recirculation zone, and there are high values at the bottom, as a result of the acceleration that occurs in the curve of the tunnel's inlet. This acceleration is certainly affecting the distribution of the friction velocity in the bottom surface, as we will see in section 5.3. Figure 19b shows the profiles of velocity component *v*. For positions 1 and 2, negative values are observed. For positions 3, 4 and 5, the values are very close to zero. For positions 6 and 7, there are positive values, indicating a small vertical acceleration in these positions. This behavior can be noticed at Figure 22, where it is possible to see a big recirculation zone in the center of the tunnel. The profiles for velocity component *w* present values very close to zero in the center of the tunnel. However, it is possible to see small values of velocity on the top and at the bottom of the tunnel. This behavior probably occurs as an effect of the expansion section at the beginning of the tunnel, where the air comes from a narrow tube and gets into a bigger section, which makes it expand to the sides of the tunnel.

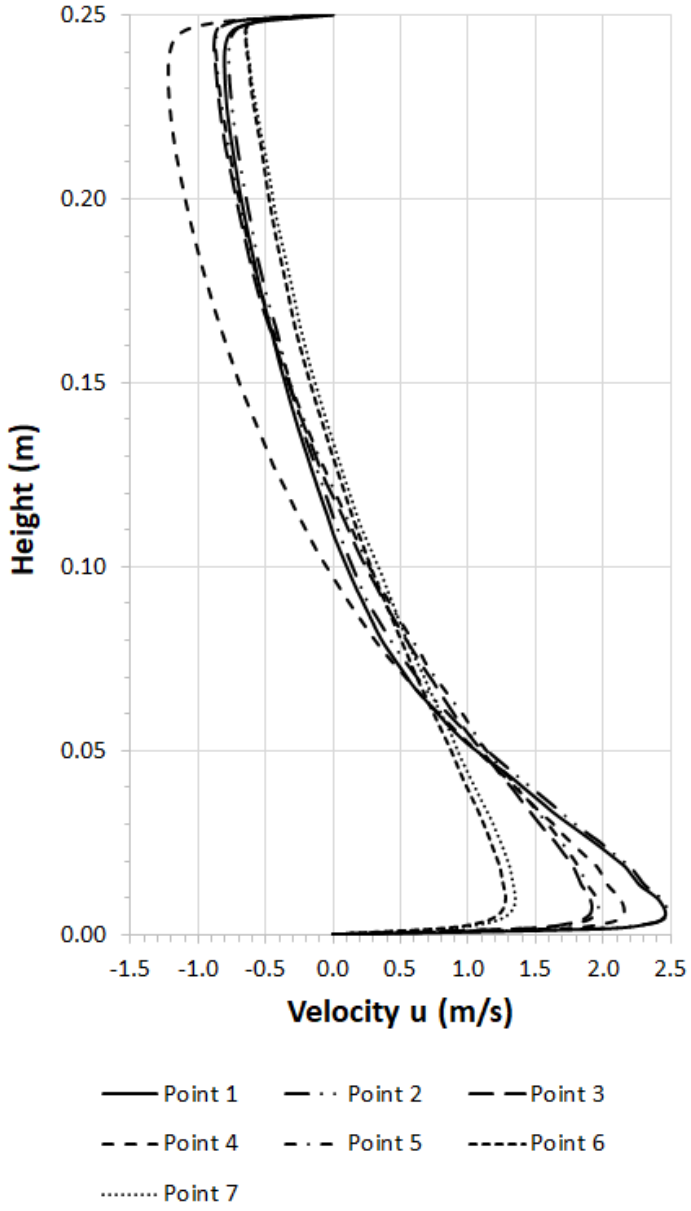

(a) Velocity profile for velocity component u

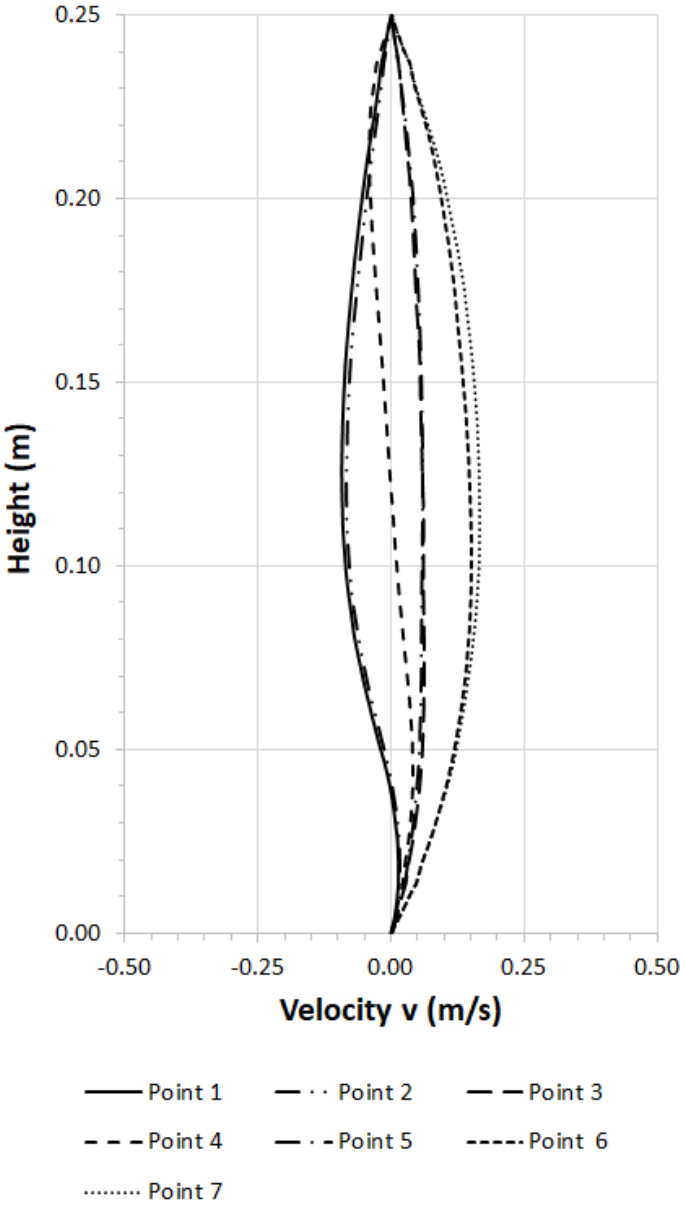

(b) Velocity profile for velocity component v

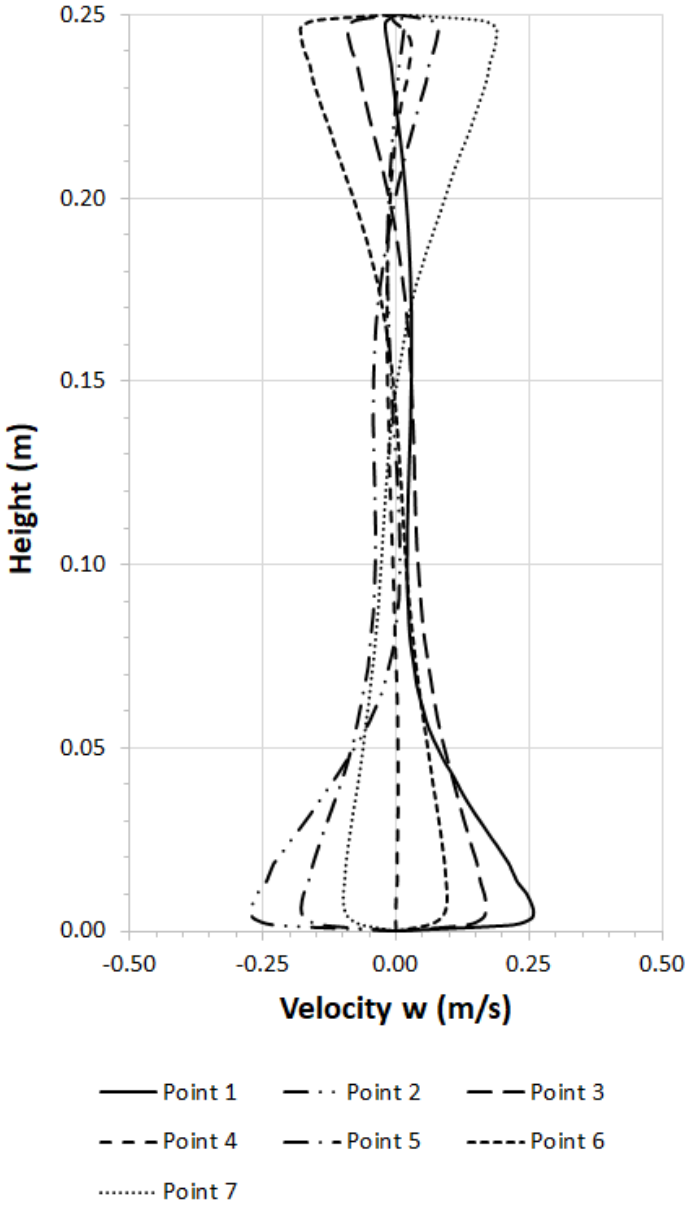

(c) Velocity profile for velocity component w

Figure 19: Velocity profiles in the main section of the tunnel.

Figures 20, 21 and 22 show the vectors of the flow in upper and side view planes of the tunnel, respectively. Figure 20 shows the bottom surface of the tunnel, where it is possible to see that the flow arrives at the bottom accelerated and uniform. Figure 21 is a plane view at the medium height of the tunnel that shows recirculation zones as the flow enters the expansion section and a symmetric behavior of the flow can be seen among the vectors in the center of the tunnel. Figure 22 is a plane of the side of the tunnel that shows an acceleration after the inlet curve, resulting in a big recirculation zone that occupies the whole main section of the tunnel. Probably, this long recirculation zone is a result of the small resistance the flow encounters in the bottom surface of the tunnel. At the end of the tunnel, the flow tends to the vertical direction, a behavior that was noticed in the velocity profiles in Figure 19.

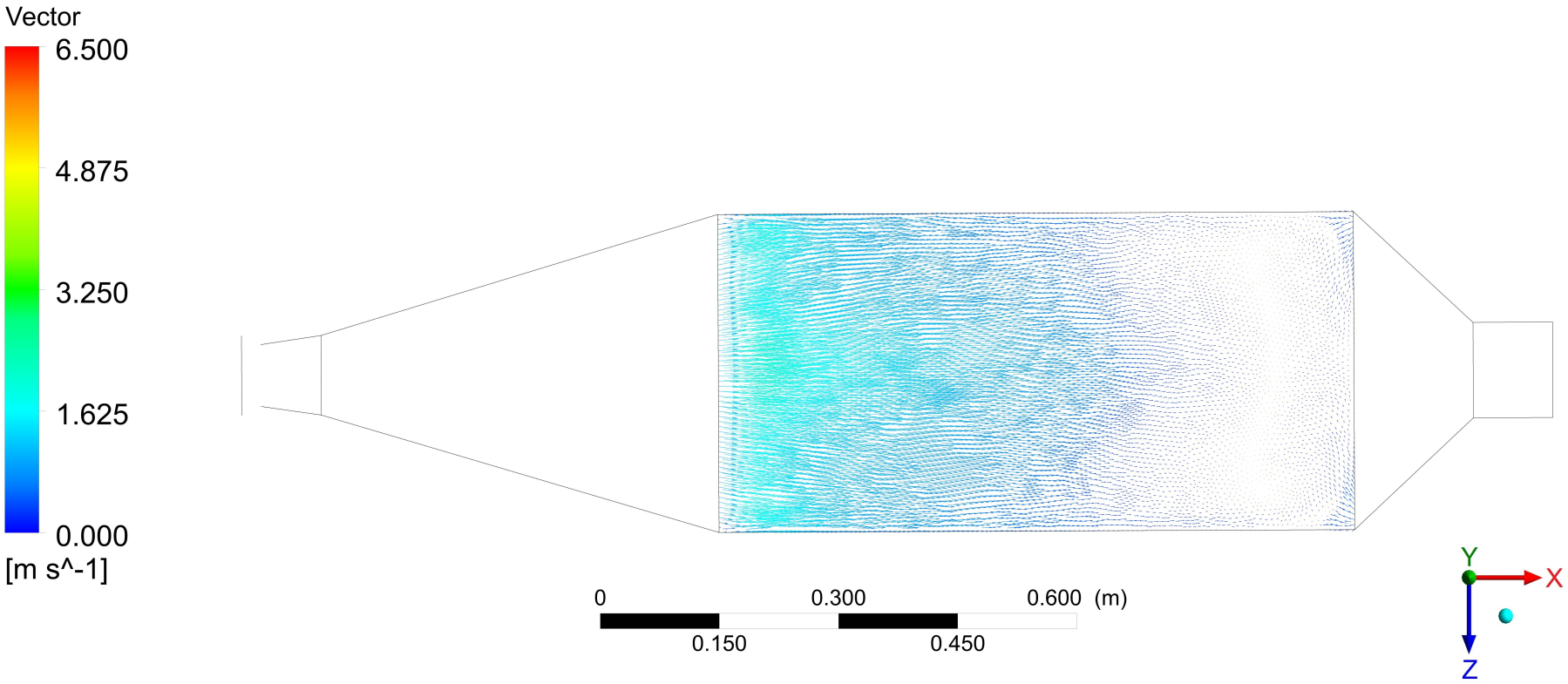

Figure 20: Tunnel's upper view of vectors for $K_s = 0\ m$.

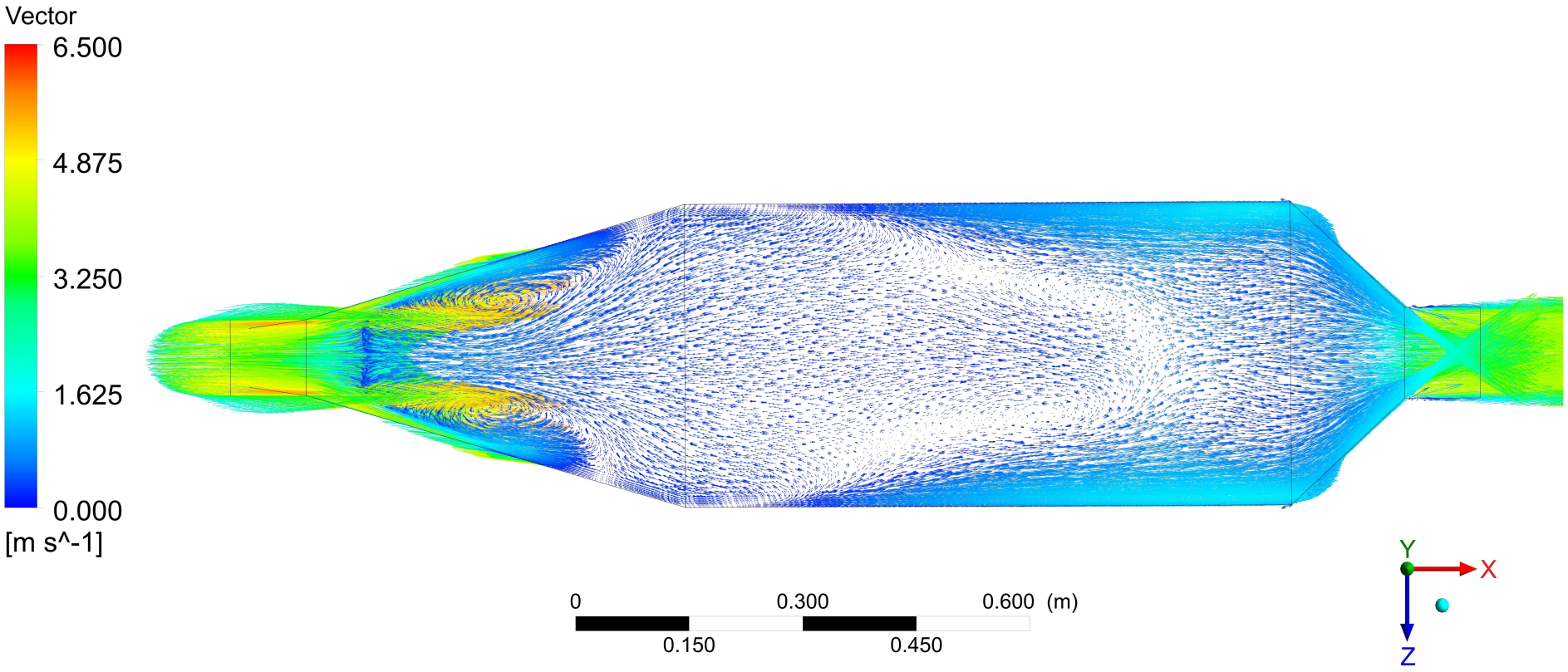

Figure 21: Tunnel's upper view of vectors for $K_s = 0\ m$.

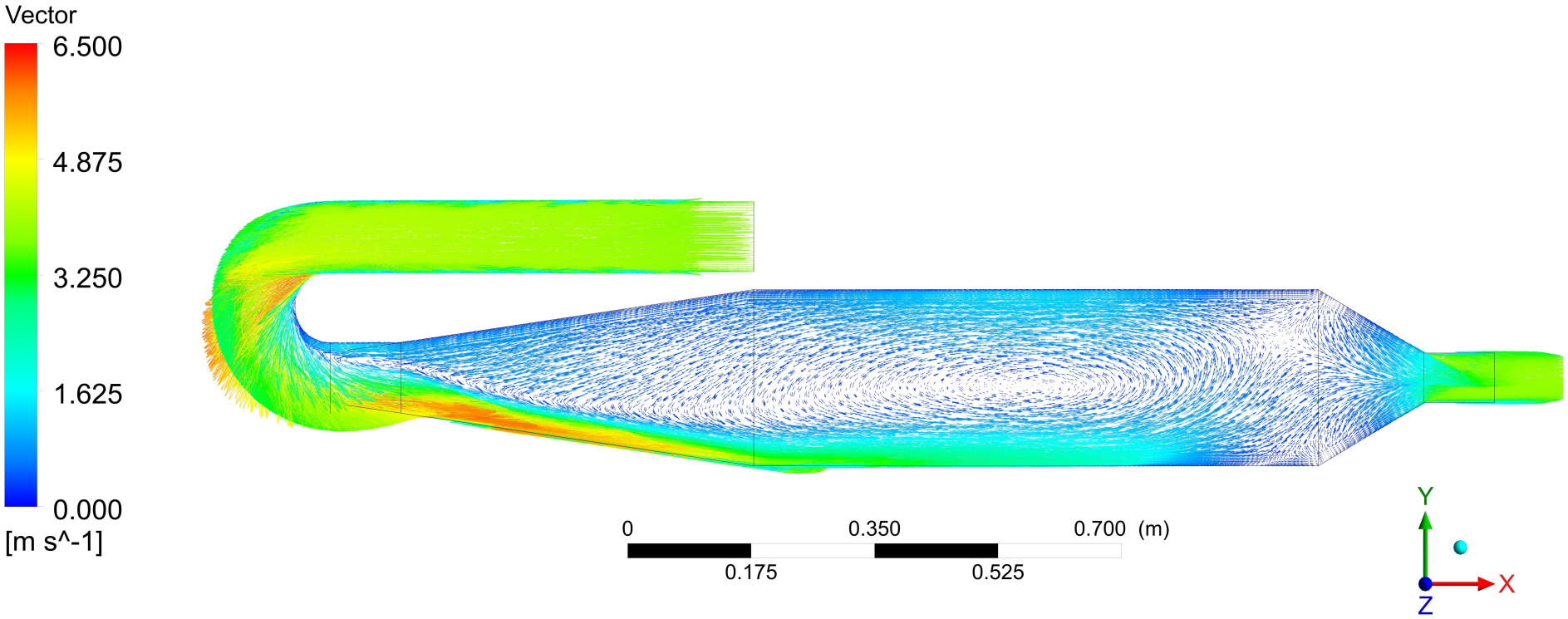

Figure 22: Tunnel's side view of vectors for $K_s = 0\ m$.

5.3 Influence of the roughness of the surface on the flow inside the tunnel

This wind tunnel was designed to determine odor emission rates from areal surfaces. Therefore, it is important to know if this model is suitable to be used over both liquid and rough surfaces, like the ones found in wastewater treatment plants and landfill sites. For this reason, numerical simulations were performed aiming to understand the flow behavior over smooth and rough surfaces. The simulations were carried out with no-slip condition, the uniform inlet velocity of $3.82\ m\ s^{-1}$, which corresponds to the average velocity of $0.3\ m\ s^{-1}$ in the center of the tunnel and the values of roughness considered were $K_s = 0.03\ m$, $K_s = 0.003\ m$, $K_s = 0.0003\ m$ and $K_s = 0.00\ m$.

The results of the numerical simulations show that the flow inside the tunnel describes a symmetrical pattern (which was expected since the geometry is symmetrical), and the development of vortices can be observed, as shown in Figures 23, 24 and 25. These figures present vectors of the flow on planes. Figure 23 shows that the flow enters the main section uniformly distributed. For all roughness values, it is possible to see two predominant vortices at the expansion area (Figure 24). This occurs due to the expansion section located at the beginning of the tunnel, where the flow comes from a strait tube and goes into a bigger area, creating these recirculation zones close to the side walls. It was also noticed that, for all the cases, there is a big recirculation zone in the center of the tunnel (Figure 25). This recirculation gets longer as the bottom surface gets smother. The bigger the value of the roughness parameter, the greater the resistance it causes on the flow, making the recirculation zone shorter as the roughness increases. Figure 25a shows that the highest roughness ($K_s = 0.03\ m$) causes a more intense recirculation zone in the center of the main section.

It was noticed that, as a function of the curve in the wind tunnel's inlet duct (Figure 25), there is an acceleration of the flow in the subsequent region for all roughness values. Due to the physical configuration of the tunnel, the air enters the expansion section and is ejected into the main section. This effect creates a rotation inside the main section and the "dead zones" that are observed near the corners in the expansion section. This is called the "jet effect" and becomes more intense if the inlet velocity is increased. This effect may not be desired, because it can cause an incorrect measurement of the odor concentrations. The mass transfer is directly related to the friction velocity on the emitting surface. High velocities of the flow cause a low resistance to the mass transfer at the emitting surface, then, if the flow passing over the emitting surface has a higher velocity than the flow found in natural conditions, it can cause an overestimation of the odor concentrations measured. This effect is even more pronounced inside the tunnel, since its boundary layer is much thinner than the one found in the field.

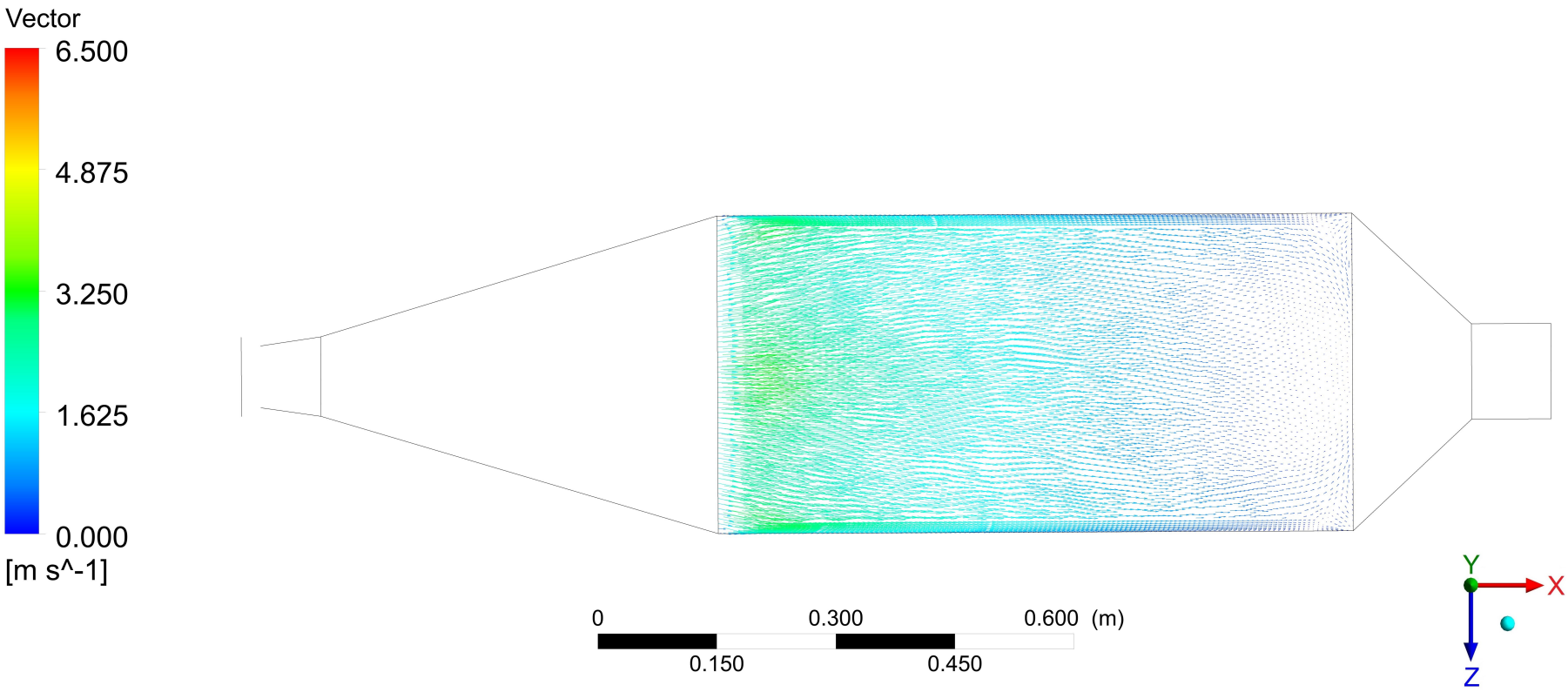
Vector
6.500
4.875
3.250
1.625
0.000
[m s^-1]
0
0.300
0.600 (m)
0.150
0.450
Y
X
Z

(a) $K_s = 0.03\ m$

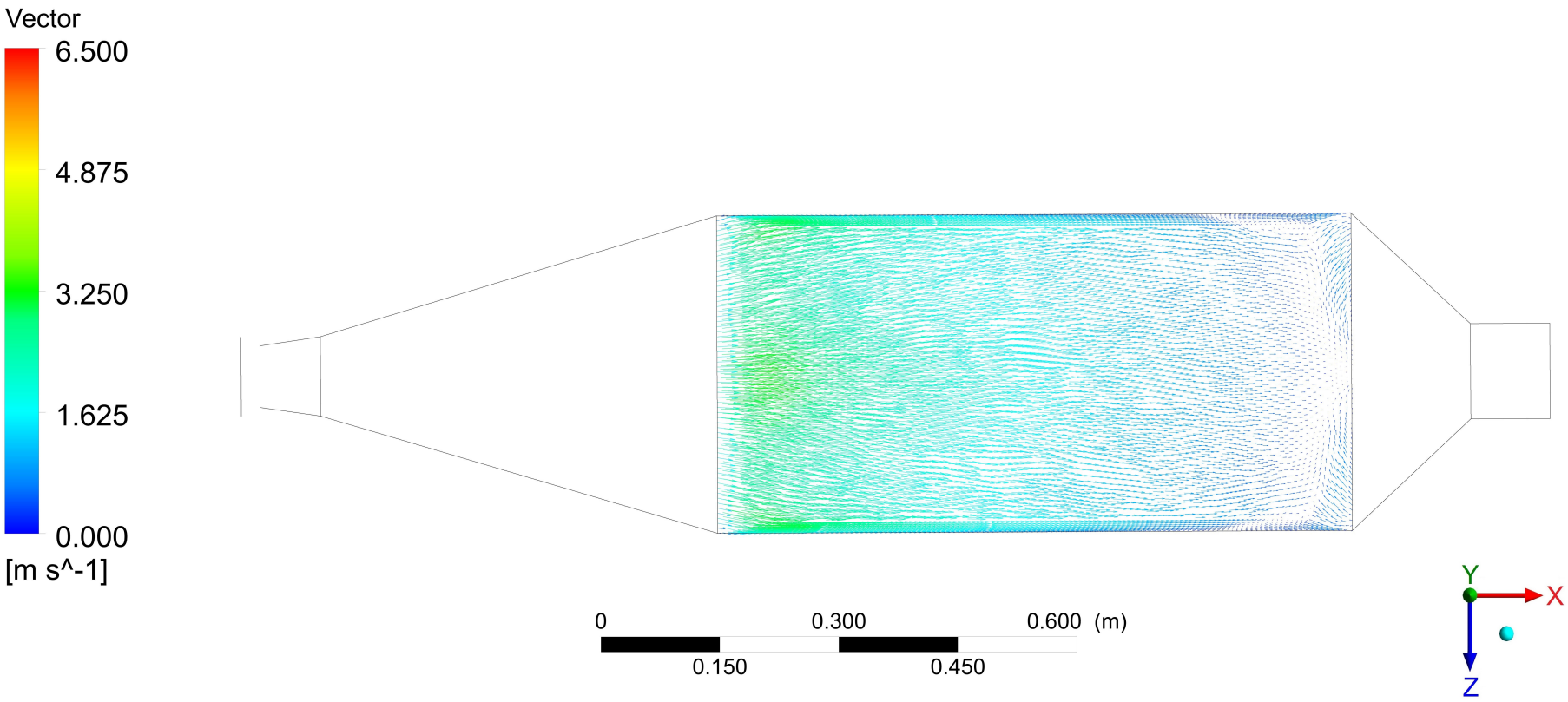
Vector
6.500
4.875
3.250
1.625
0.000
[m s^-1]
0
0.300
0.600 (m)
0.150
0.450
Y
X
Z

(b) $K_s = 0.003\,m$

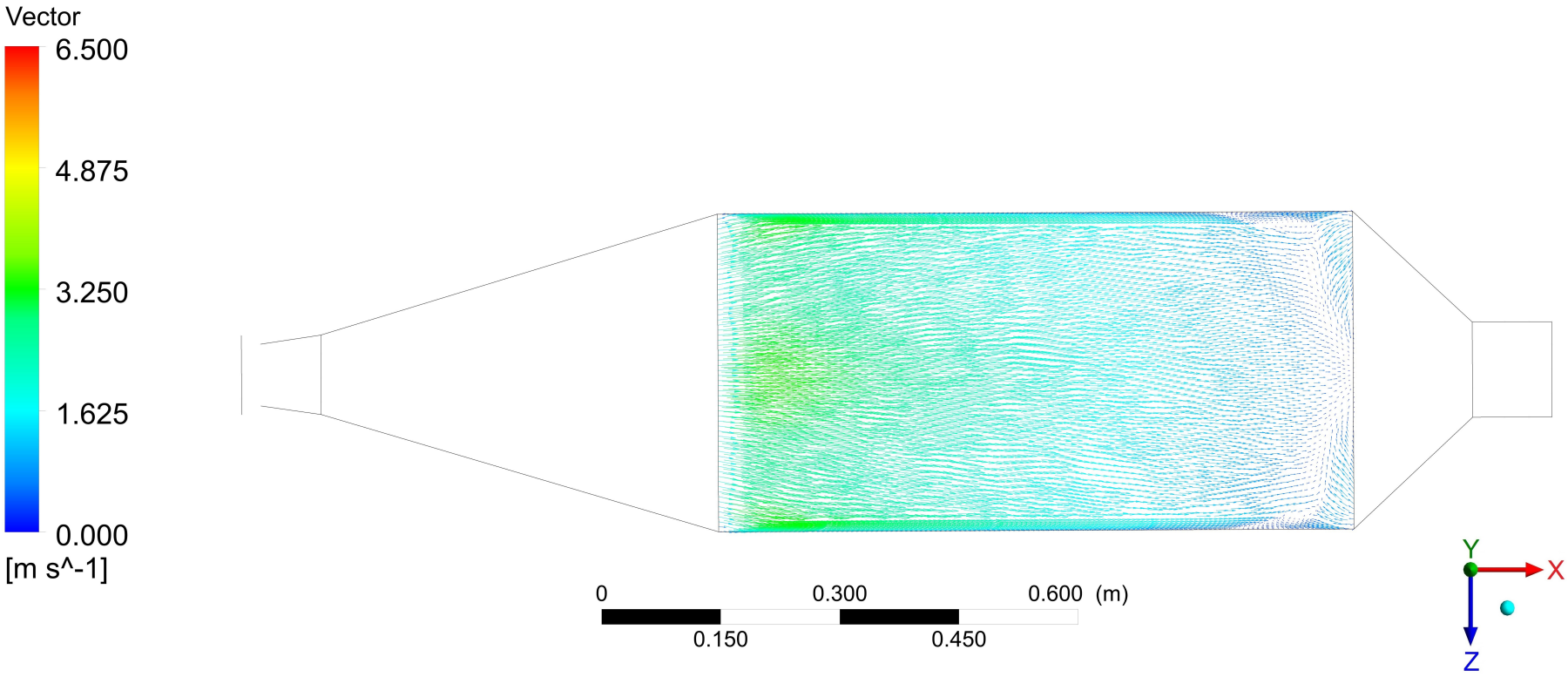
Vector
6.500
4.875
3.250
1.625
0.000
[m s^-1]
0
0.300
0.600 (m)
0.150
0.450
Y
X
Z

(c) $K_s = 0.0003\,m$

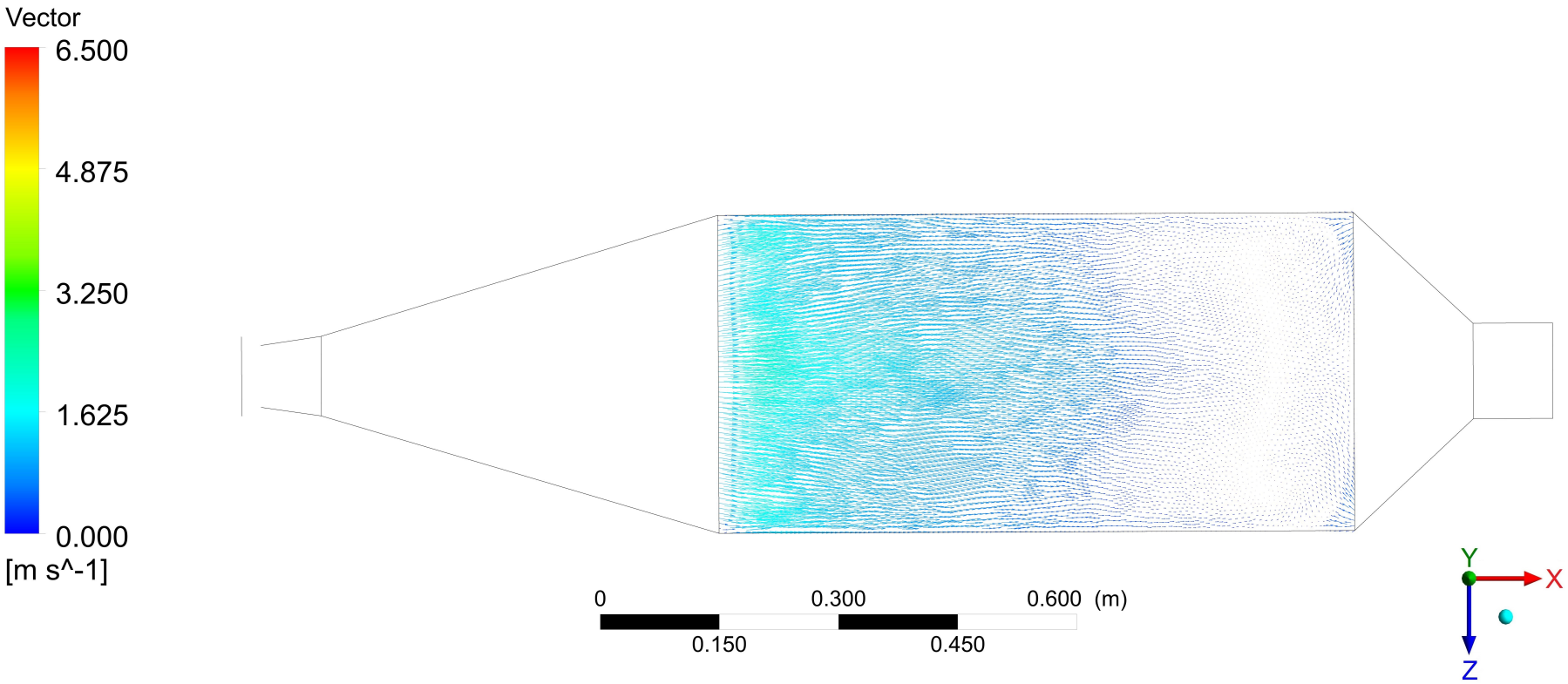

(d) $K_s = 0.0\,m$

Figure 23: Tunnel's upper view of vectors for (a) $K_s = 0.03\,m$, (b) $K_s = 0.003\,m$, (c) $K_s = 0.0003\,m$ and (d) $K_s = 0.0\,m$.

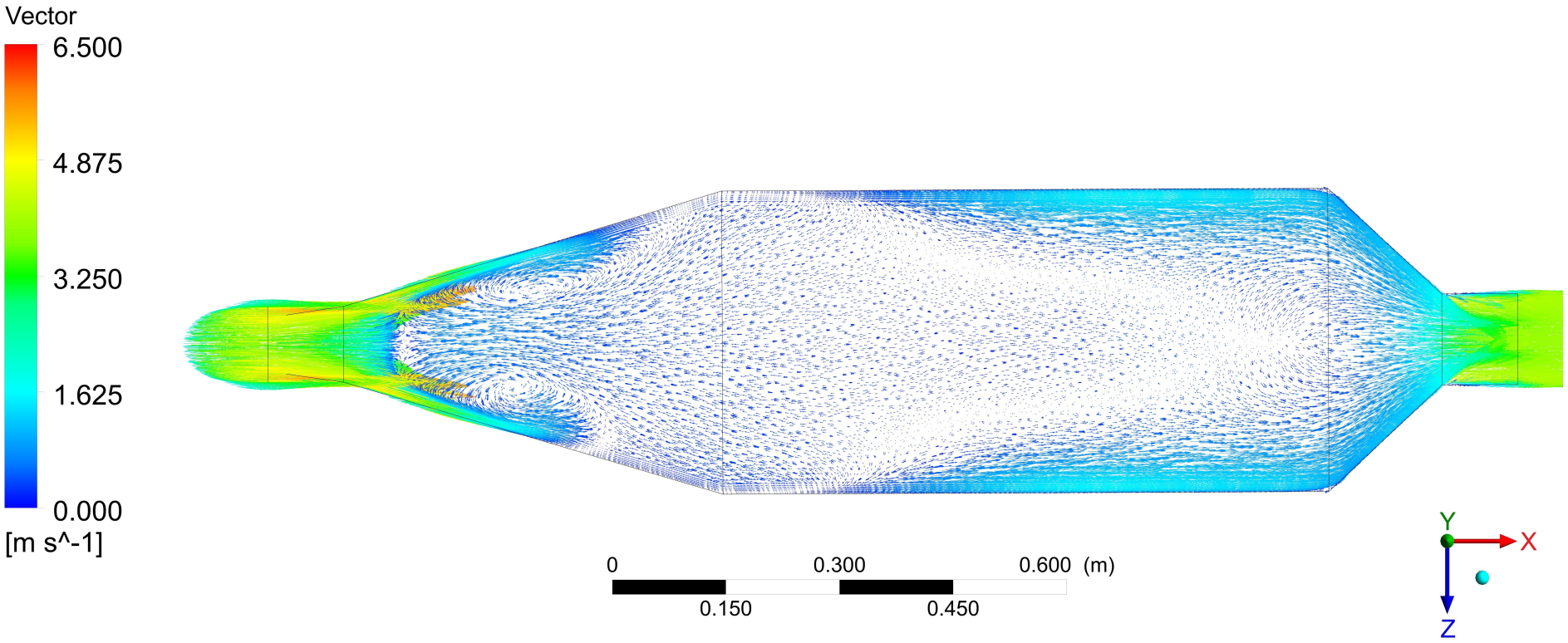
Vector
6.500
4.875
3.250
1.625
0.000
[m s^-1]
0
0.300
0.600 (m)
0.150
0.450
Y
X
Z

(a) $K_s = 0.03\ m$

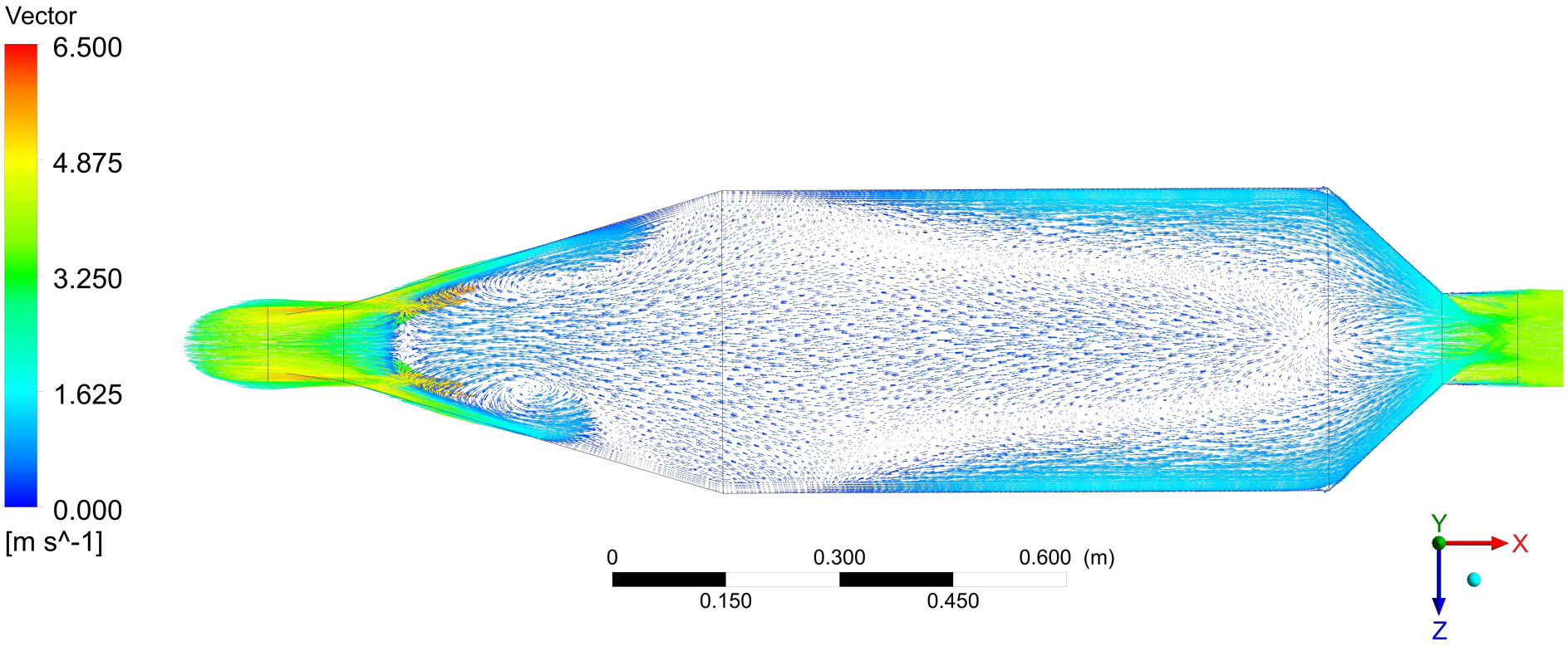
Vector
6.500
4.875
3.250
1.625
0.000
[m s^-1]
0
0.300
0.600 (m)
0.150
0.450
Y
X
Z

(b) $K_s = 0.003\,m$

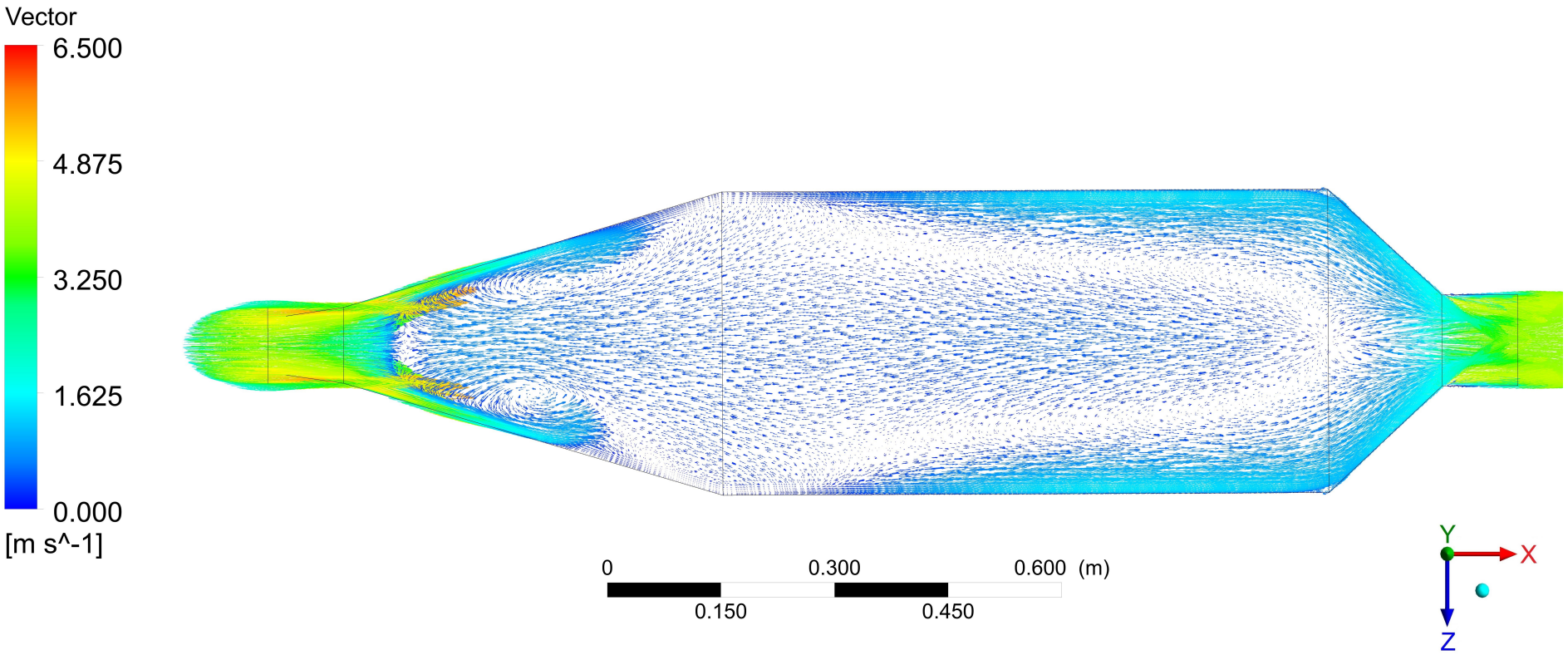
Vector
6.500
4.875
3.250
1.625
0.000
[m s^-1]
0
0.300
0.600 (m)
0.150
0.450
Y
X
Z

(c) $K_s = 0.0003\,m$

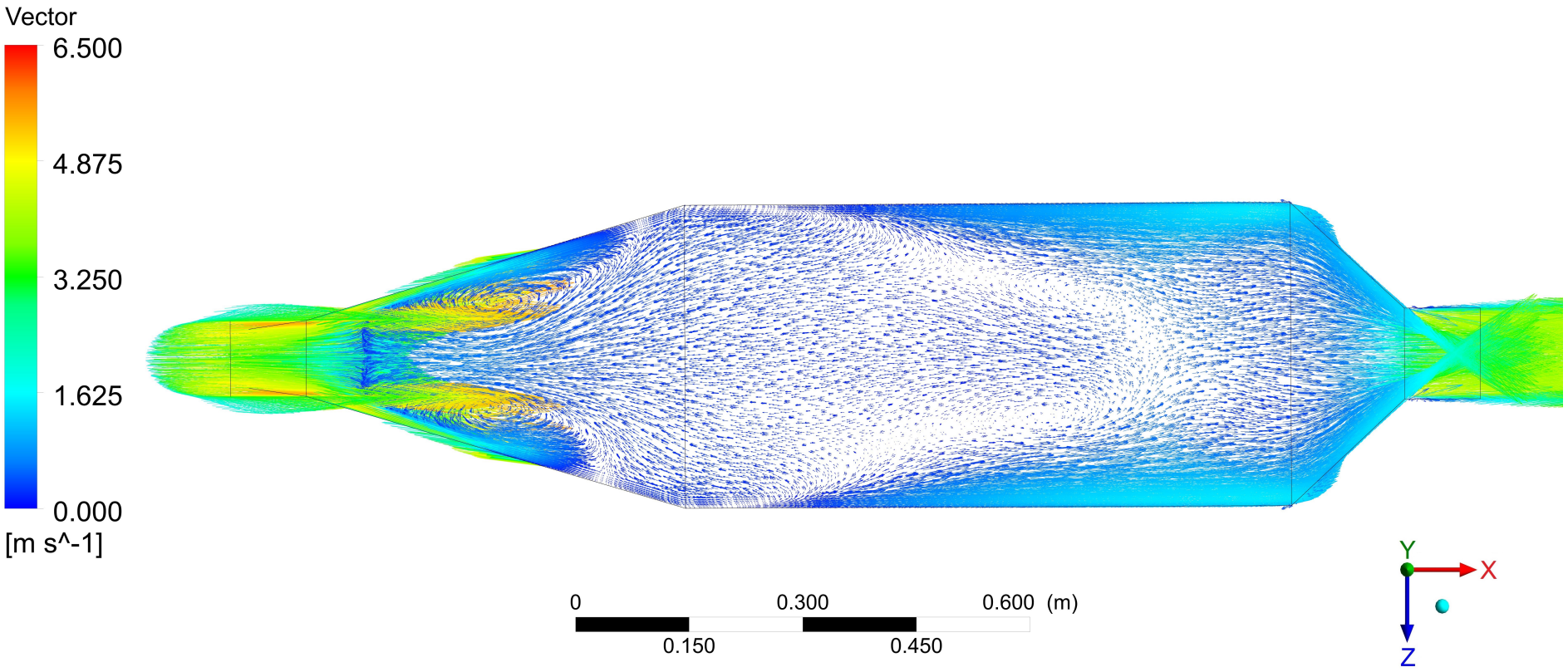

(d) $K_s = 0.0\,m$

Figure 24: Tunnel's upper view of vectors for (a) $K_s = 0.03\,m$, (b) $K_s = 0.003\,m$, (c) $K_s = 0.0003\,m$ and (d) $K_s = 0.0\,m$.

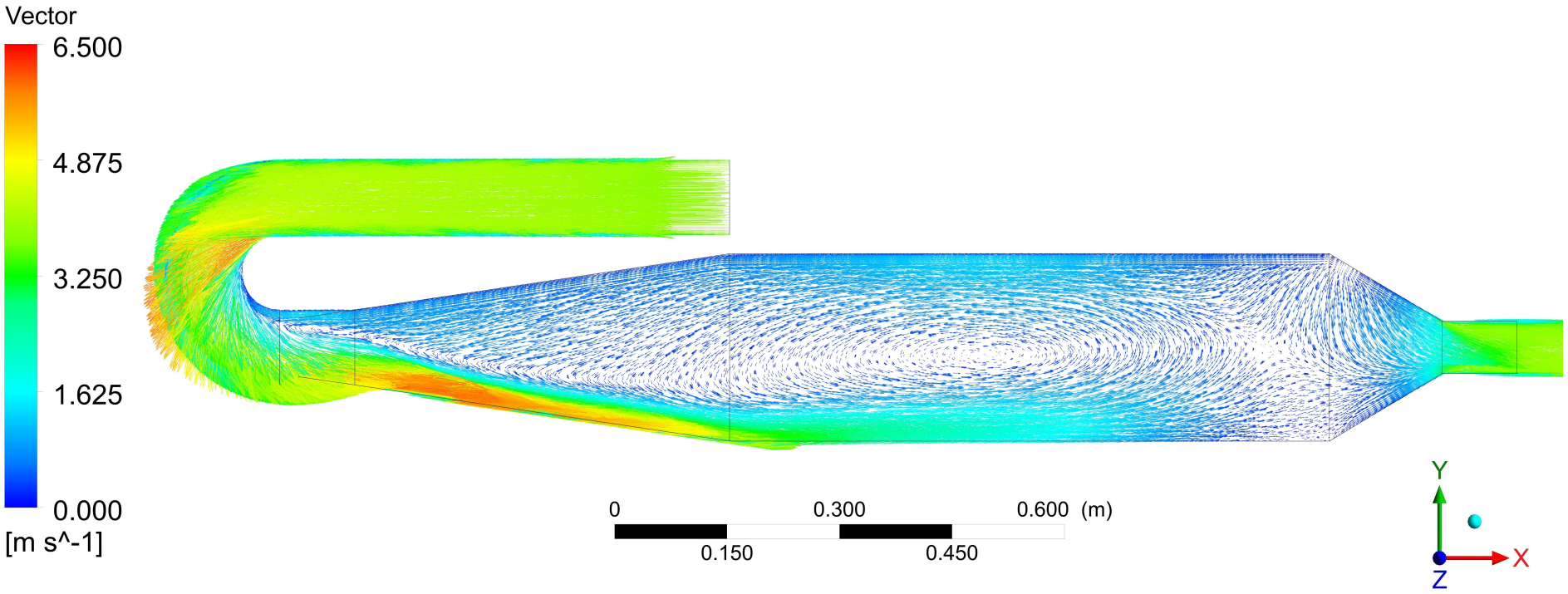
Vector
6.500
4.875
3.250
1.625
0.000
[m s^-1]
0
0.300
0.600 (m)
0.150
0.450
Y
X
Z

(a) $K_s = 0.03\ m$

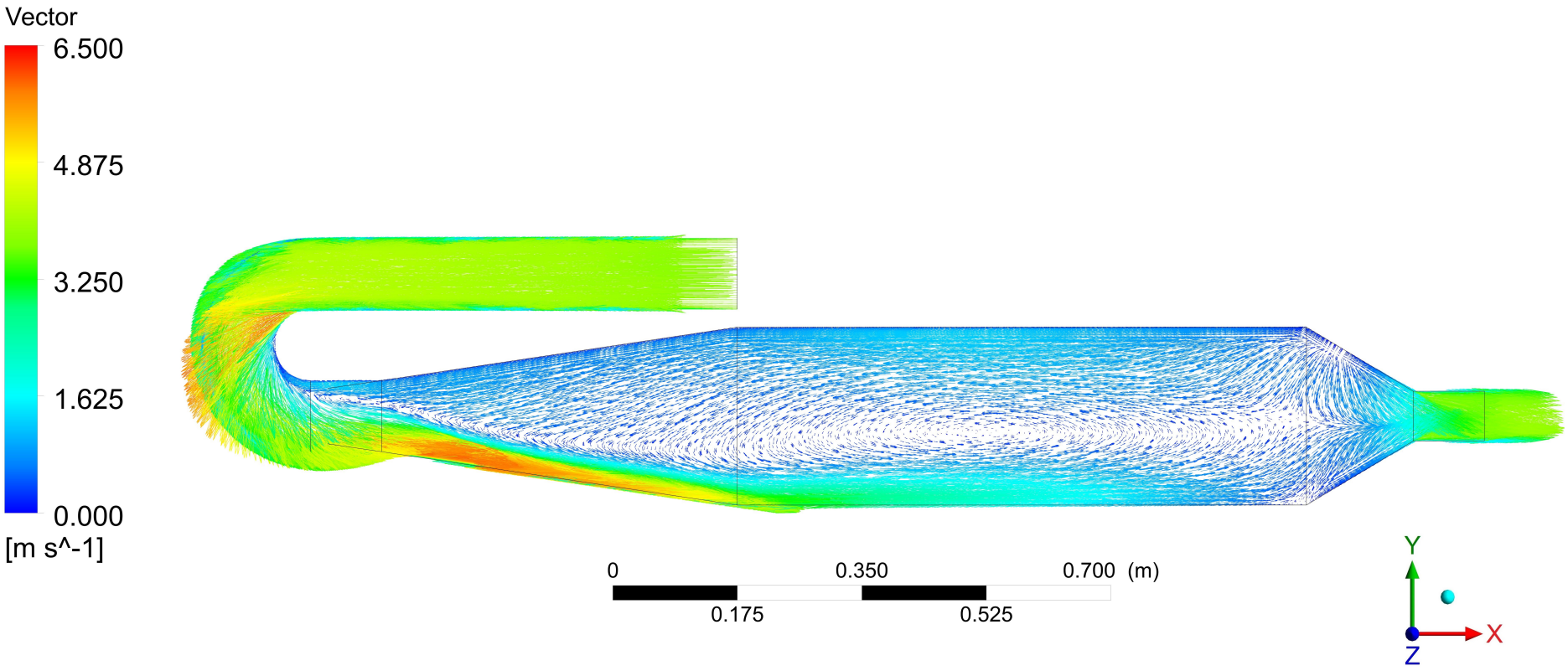
Vector
6.500
4.875
3.250
1.625
0.000
[m s^-1]
0
0.350
0.700 (m)
0.175
0.525
Y
X
Z

(b) $K_s = 0.003\,m$

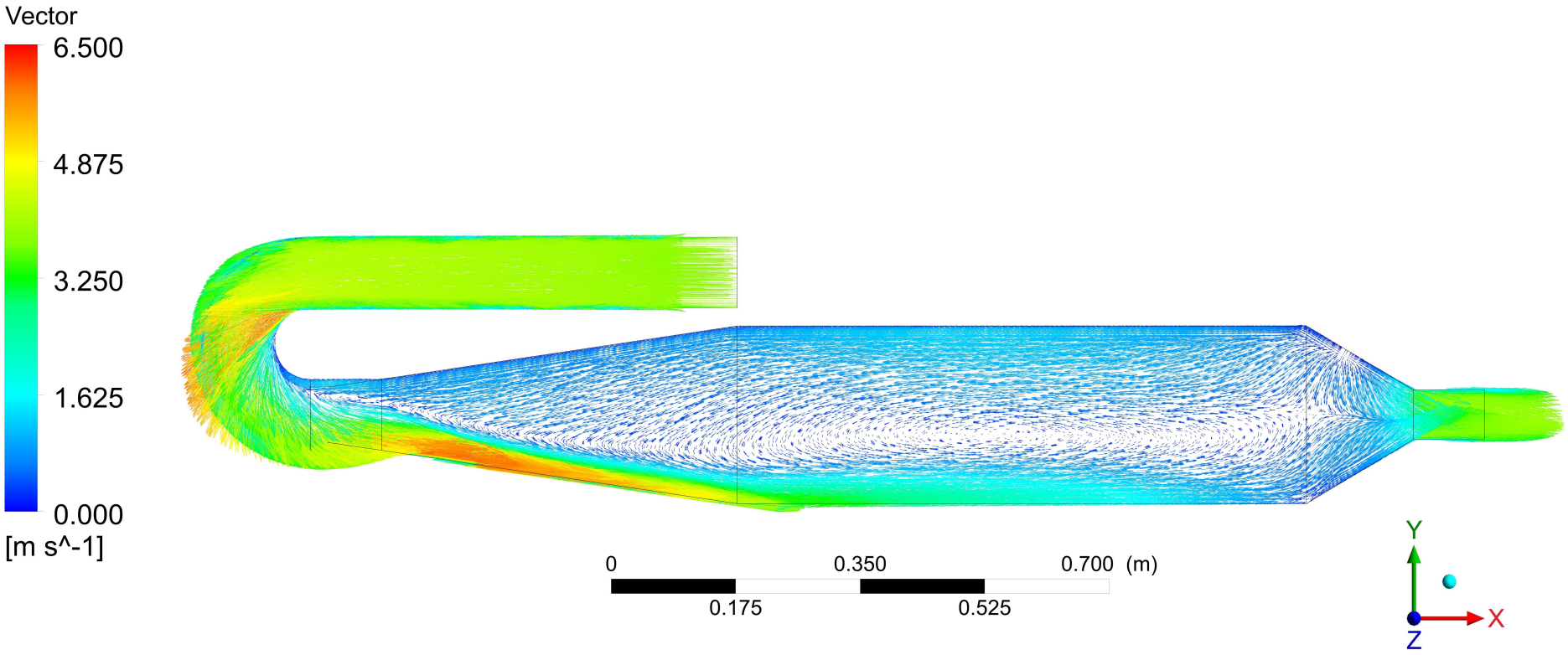
Vector
6.500
4.875
3.250
1.625
0.000
[m s^-1]
0
0.350
0.700 (m)
0.175
0.525
Y
X
Z

(c) $K_s = 0.0003\,m$

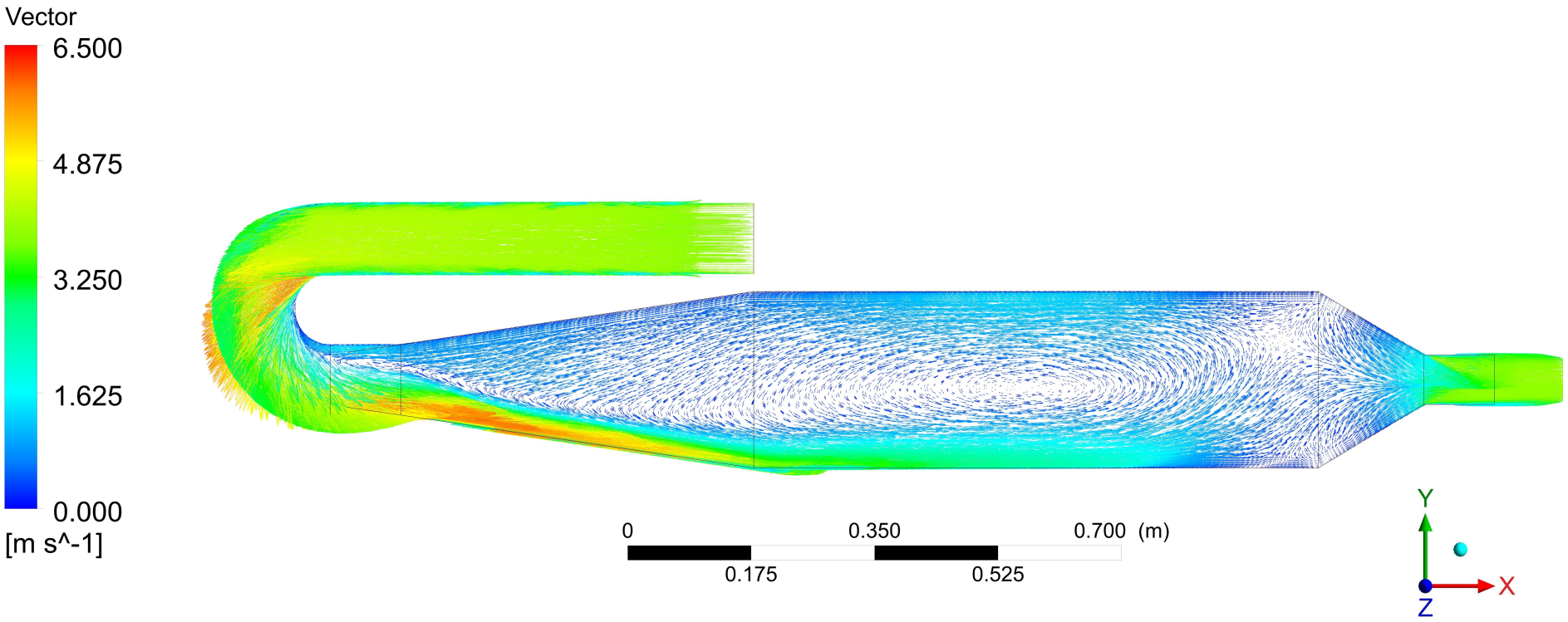

(d) $K_s = 0.0\,m$

Figure 25: Tunnel's side view of vectors for (a) $K_s = 0.03\,m$, (b) $K_s = 0.003\,m$, (c) $K_s = 0.0003\,m$ and (d) $K_s = 0.0\,m$.

Figure 26 shows the velocity vectors and the friction velocity at the bottom surface of the tunnel. The friction velocity mean values at Figure 26 are shown in Table 5. When comparing these values with the ones found by Argaín, Miranda and Teixeira (2009) over complex terrain (varying between 0.11 $m\ s^{-1}$ and 0.19 $m\ s^{-1}$), it's possible to notice that the values found for $K_s = 0.003m$ and $K_s = 0.03m$ are a little higher than the experimental ones. However, the friction velocities found in the numerical simulations presented here are a constant average, differently from the friction velocity found in atmospheric flows, that is not homogeneous. Therefore, the mean friction velocity might not be the best approach when comparing with atmospheric flows.

Table 5 – Friction velocity values for different roughness.

Roughness height (m)	**Friction velocity** ($m\ s^{-1}$)
K_s = 0.03	$\overline{u^*}$ = 0.23
K_s = 0.003	$\overline{u^*}$ = 0.20
K_s = 0.0003	$\overline{u^*}$ = 0.17
K_s = 0.0	$\overline{u^*}$ = 0.14

In Figure 26, there is a recirculation area on the center of the tunnel and it gets longer as the surface gets smother. At the beginning of the main section, the friction velocity is higher than at the end, as the flow develops. This is caused by the acceleration that comes from the inlet tube and, once the flow faces big resistance when it encounters surfaces with higher roughness values, it is slowed down at the bottom surface, which makes the recirculation zone shorter and more intense. Therefore, the friction velocity is directly related to the roughness height: the higher the roughness, the bigger the friction velocity. The friction velocity values increase as the roughness increases, but the difference between the values is not so big, as we could see in Table 5.

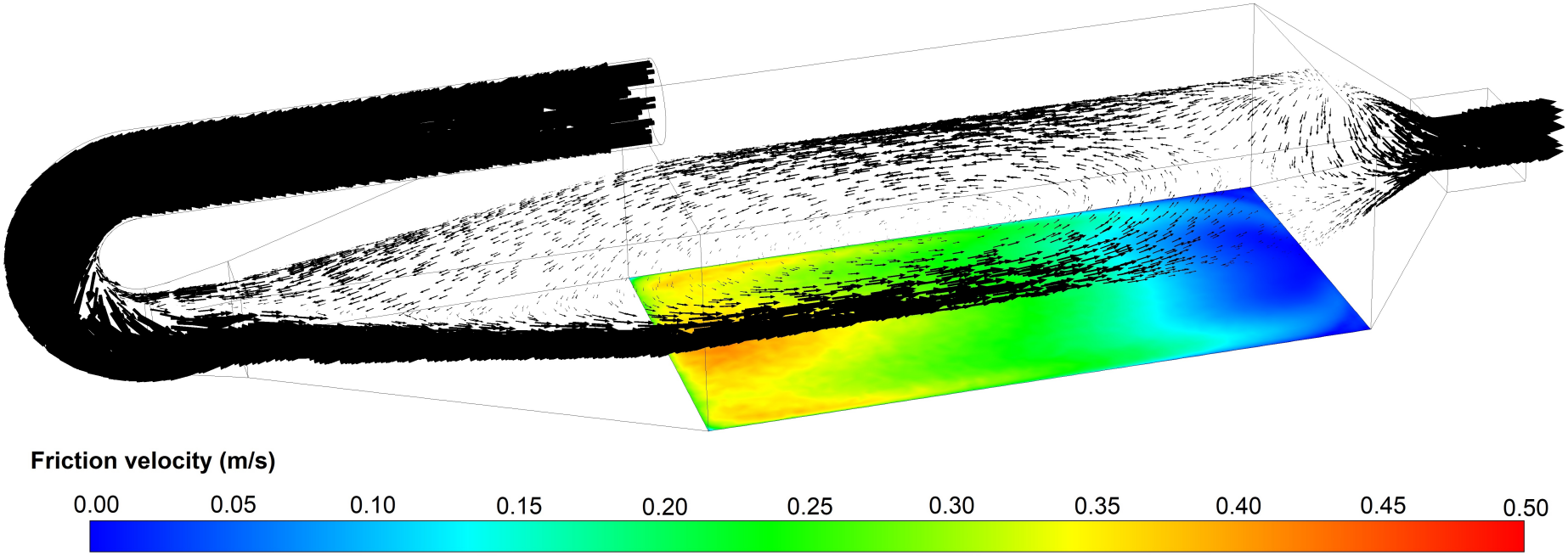
Friction velocity (m/s)
0.00
0.05
0.10
0.15
0.20
0.25
0.30
0.35
0.40
0.45
0.50

(a) $K_s = 0.03\ m$

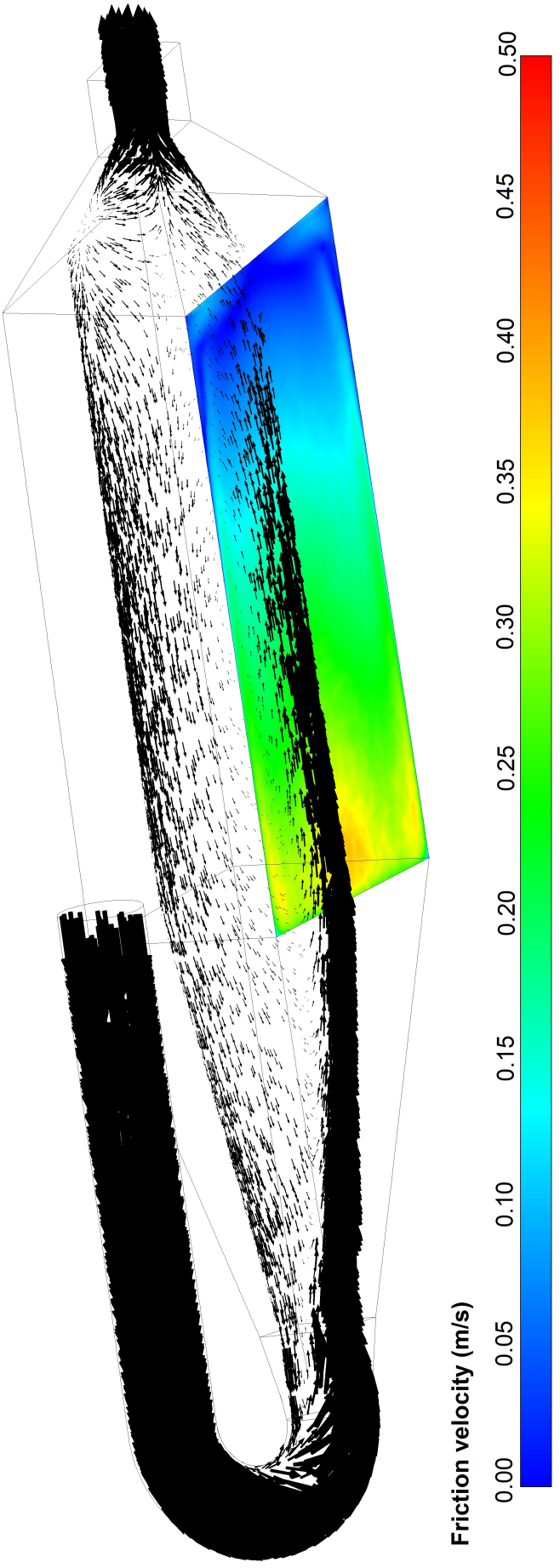
Friction velocity (m/s)
0.00
0.05
0.10
0.15
0.20
0.25
0.30
0.35
0.40
0.45
0.50

(b) $K_s = 0.003\,m$

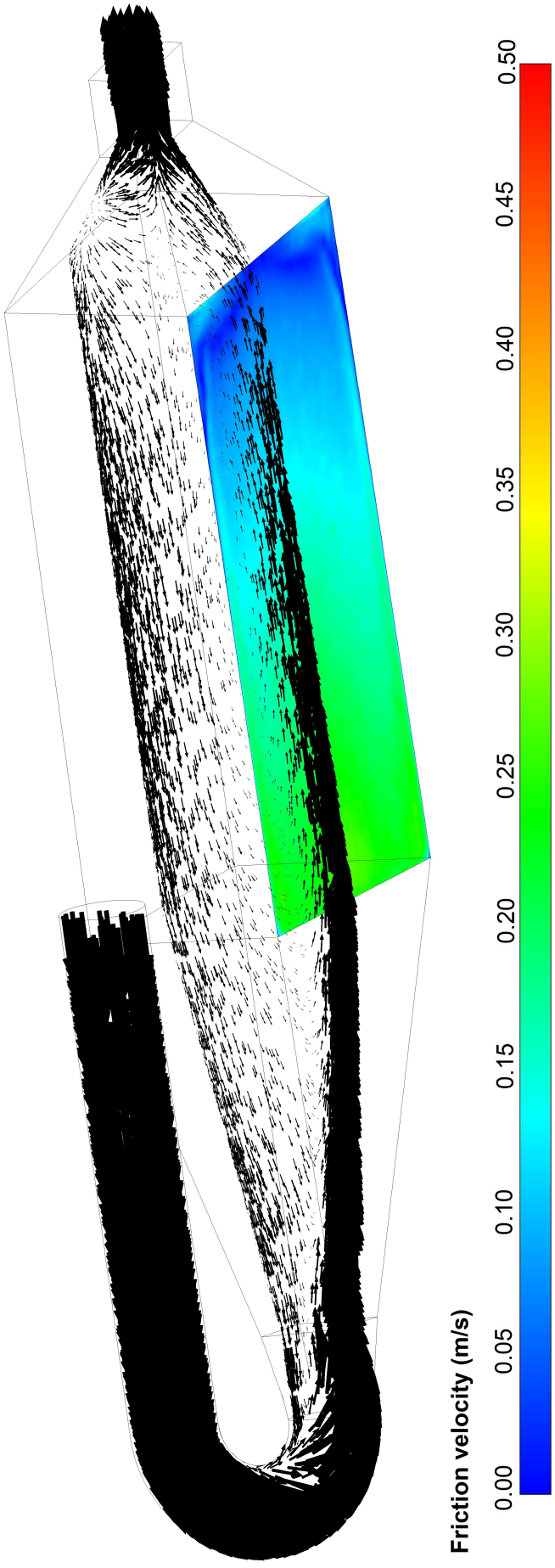
Friction velocity (m/s)
0.00
0.05
0.10
0.15
0.20
0.25
0.30
0.35
0.40
0.45
0.50

(c) $K_s = 0.0003\,m$

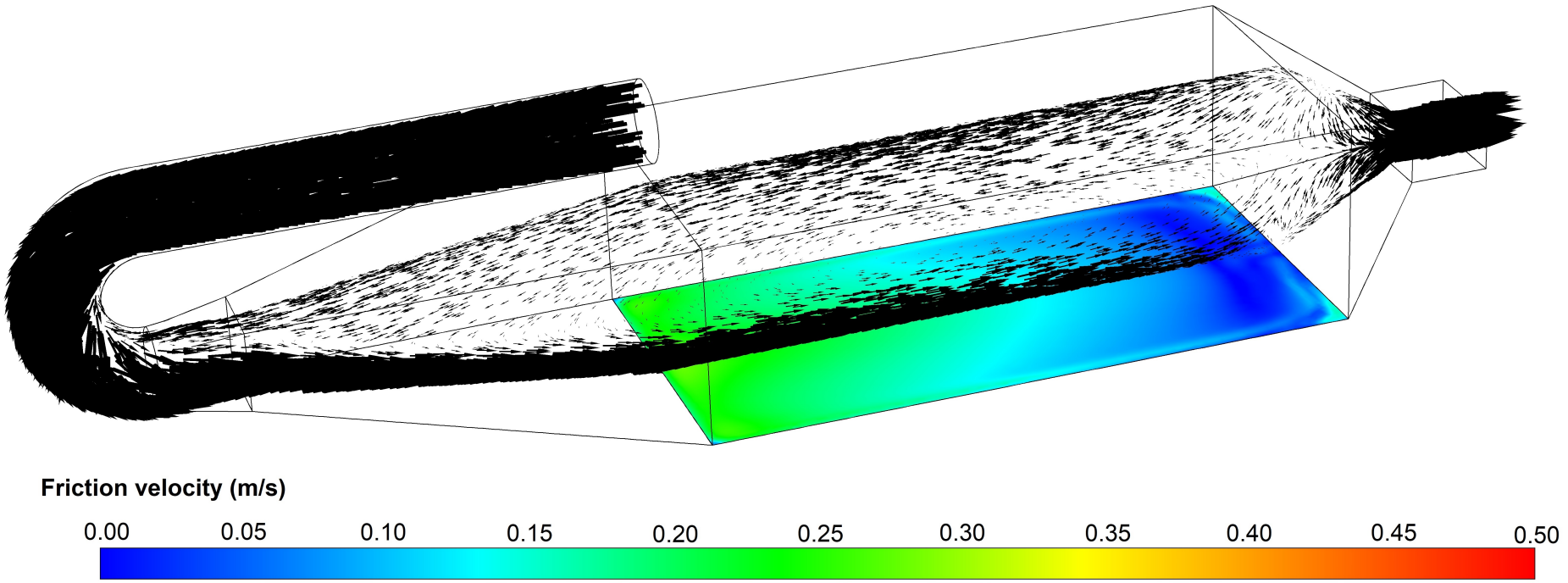

(d) $K_s = 0.0\,m$

Figure 26: Velocity vectors and friction velocity at the tunnel's bottom surface for (a) $K_s = 0.03\,m$, (b) $K_s = 0.003\,m$, (c) $K_s = 0.0003\,m$ and (d) $K_s = 0.0\,m$.

The turbulent kinetic energy (TKE) is presented in planes at the positions $x = 0.2\ m$, $x = 0.4\ m$ and $x = 0.6\ m$ in the main section of the tunnel (Figure 27). At small scales, the turbulent kinetic energy dissipates due to viscous forces. The results showed in Figure 27 presented higher dissipation of the TKE for higher roughness heights. This indicates that a dissipation of the turbulence occurs due to friction, as the flow encounters resistance in the rough surfaces. It means that, for smooth surfaces, the TKE is higher because there is less friction to dissipate it. Also, the TKE is more intense at the beginning of the tunnel, at the bottom surface, and dissipates as the flow develops through the tunnel.

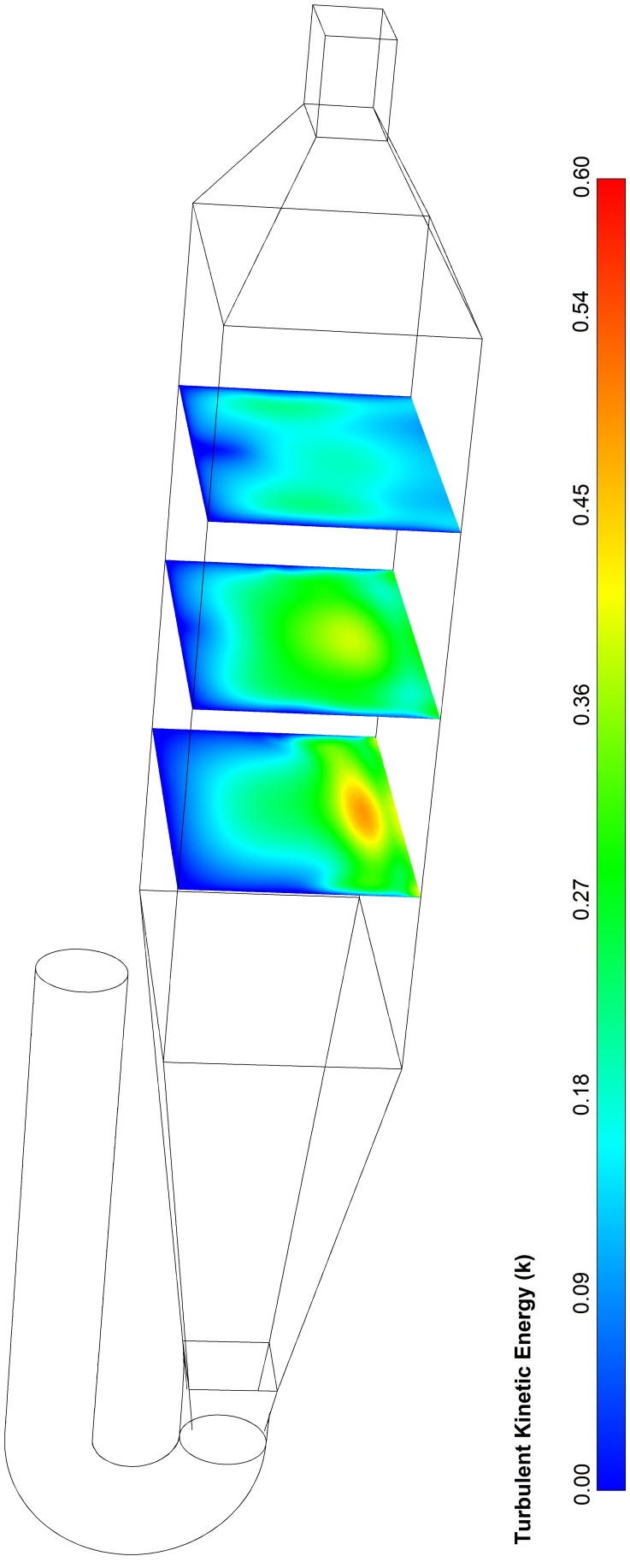

(a) $K_s = 0.03\ m$

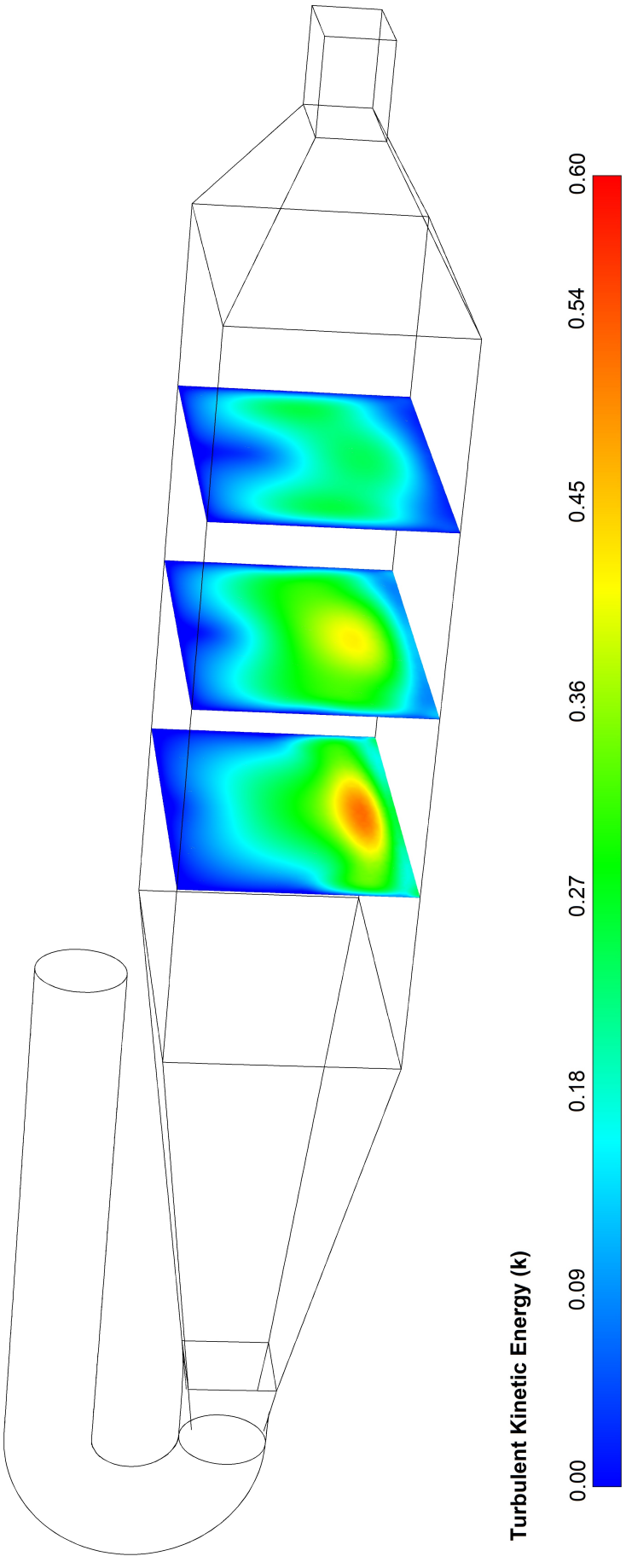

(b) $K_s = 0.003\,m$

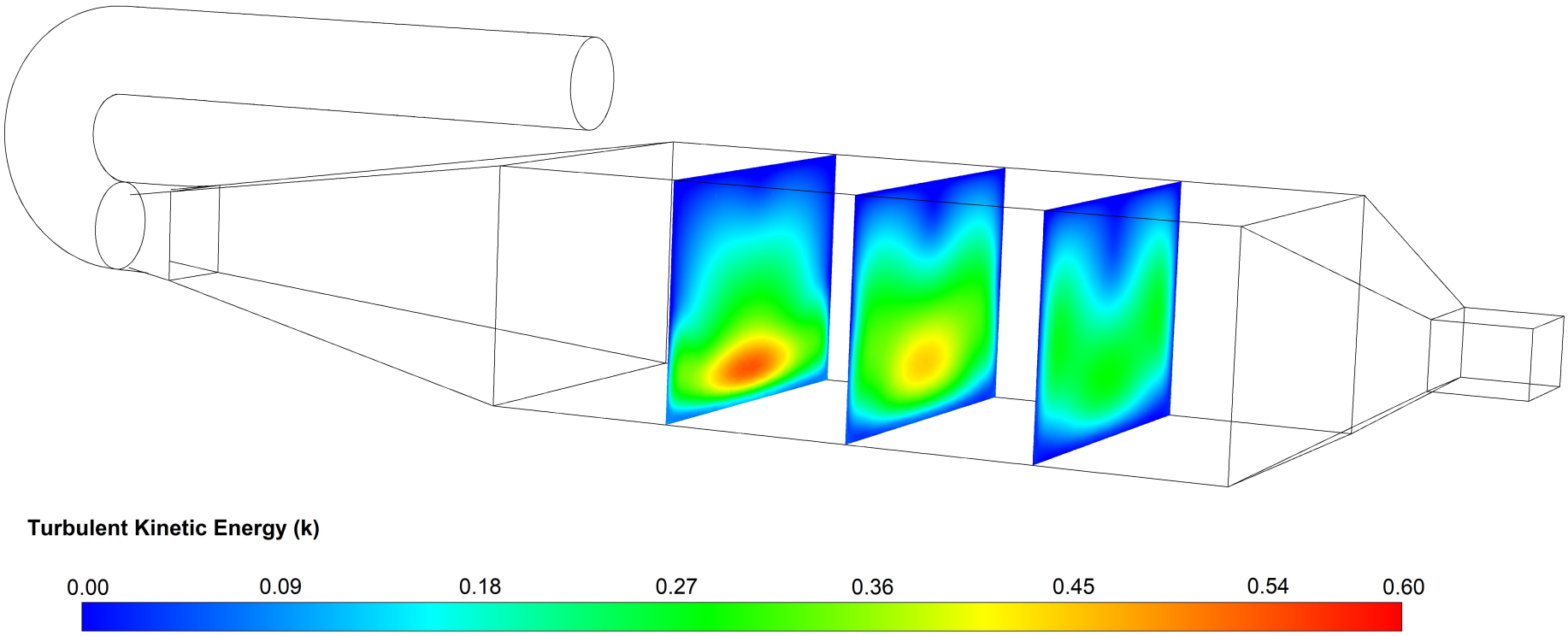

(c) $K_s = 0.0003\,m$

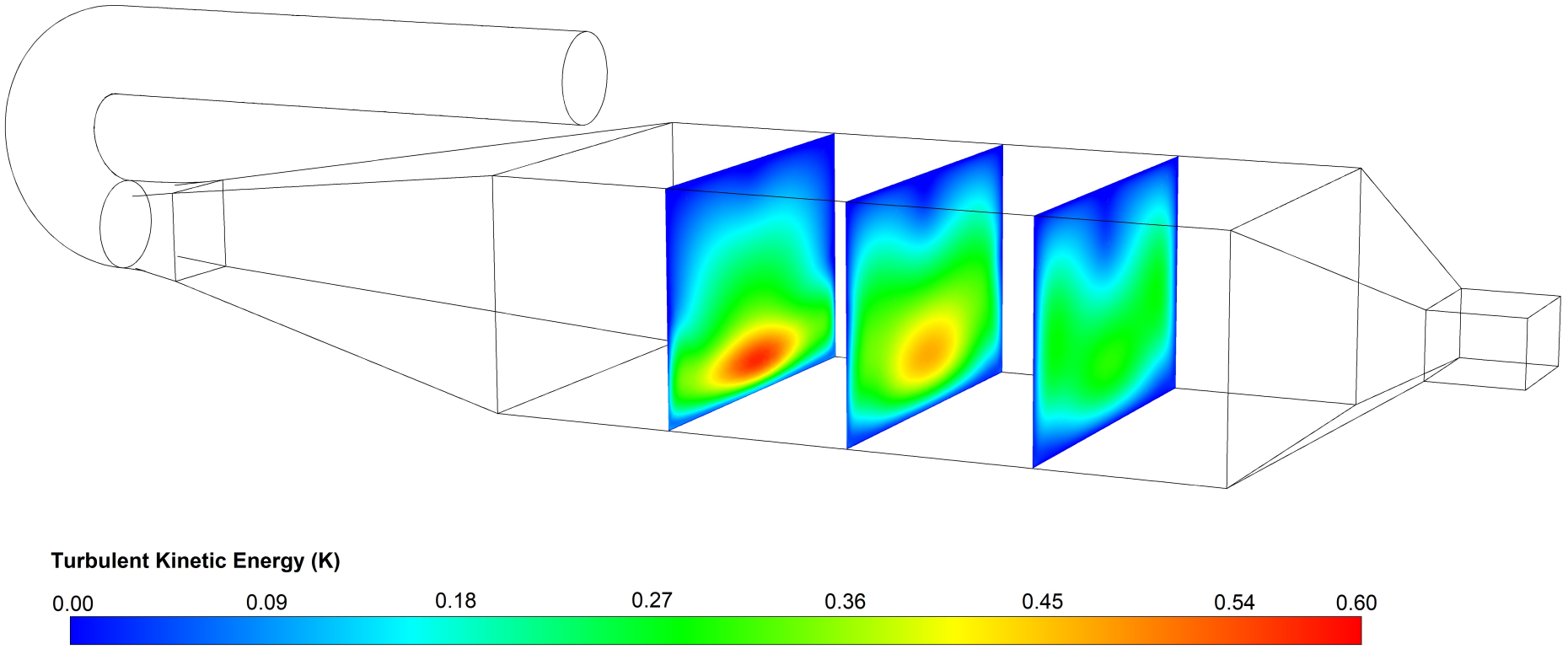

(d) $K_s = 0.0\,m$

Figure 27: Turbulent kinetic energy at positions $x = 0.2\,m$, $x = 0.4\,m$ and $x = 0.6\,m$ for (a) $K_s = 0.03\,m$, (b) $K_s = 0.003\,m$, (c) $K_s = 0.0003\,m$ and (d) $K_s = 0.0\,m$.

5.4 Influence of different inlet velocities on the flow inside the tunnel

Jiang, Bliss and Schulz (1995) studied the wind tunnel experimentally with the objective to understand the aerodynamic performance of the device. They carried out experiments with the mean air velocity of 0.33, 0.43, 0.54 and 0.78 $m\ s^{-1}$ in the central part of the tunnel. The minimum velocity was limited to 0.33 $m\ s^{-1}$ due to the sensitivity of the anemometer used. During the experiments, the tunnel became unstable due to wave action with velocities higher than 0.6 $m\ s^{-1}$. After the tests, they found that the lower the mean velocity, the better the aerodynamic performance of the tunnel and they concluded that the optimum velocity to work with the tunnel was 0.33 $m\ s^{-1}$.

Balsari et al. (2007) performed experimental tests using a tunnel very similar to the one designed by Jiang, Bliss and Schulz (1995). They measured NH_3 emissions from pig and cattle slurry. The air velocity used to perform the tests was 0.5 $m\ s^{-1}$. Perta et al. (2016) performed numerical simulations also with a wind tunnel similar to the one designed by Jiang, Bliss and Schulz (1995). They chose the velocity of 0.33 $m\ s^{-1}$ to perform the tests.

Since many authors performed numerical and/or experimental tests using the velocity of 0.33 $m\ s^{-1}$, or higher, in the present study, velocities of 0.3, 0.2 and 0.1 $m\ s^{-1}$ were tested with the objective of understanding the flow behavior under lower velocities. It is important to notice that these mean velocities are encountered in the main section of the tunnel. The inlet uniform air velocities are 1.27, 2.55 and 3.82 $m\ s^{-1}$. The numerical simulations were performed with smooth surface ($K_s = 0\ m$) and no-slip condition.

Figures 28, 29 and 30 show the vectors of the flow in planes for the three velocities. They present a very similar and symmetrical behavior. As noticed before, recirculation zones can be seen in the expansion section, although for the lowest velocity (0.1 $m\ s^{-1}$) they are almost nonexistent. Figure 30 shows the side view of the tunnel and the recirculation zone in the center of the tunnel gets more intense as the velocity increases.

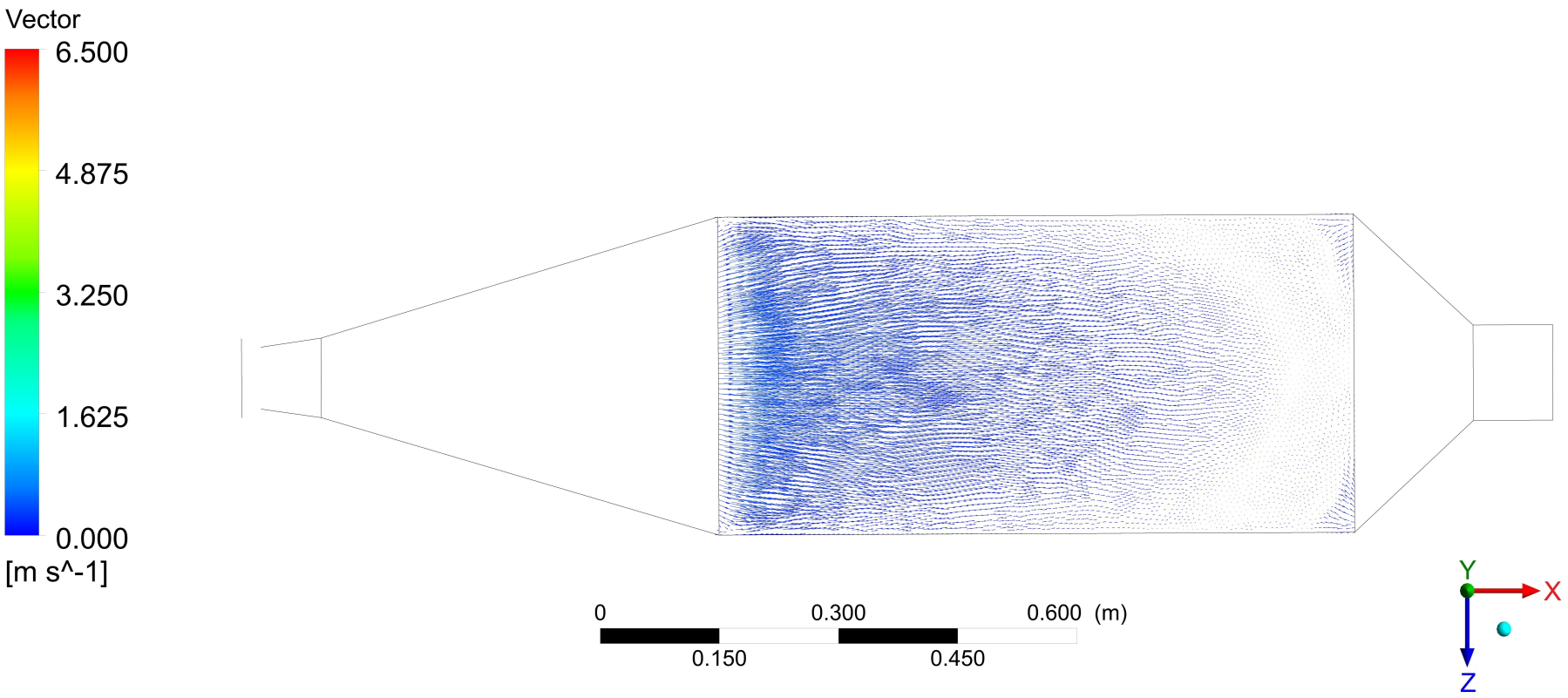
Vector
6.500
4.875
3.250
1.625
0.000
[m s^-1]
0
0.300
0.600 (m)
0.150
0.450
Y
X
Z

(a) vel = 0.1 $m\ s^{-1}$

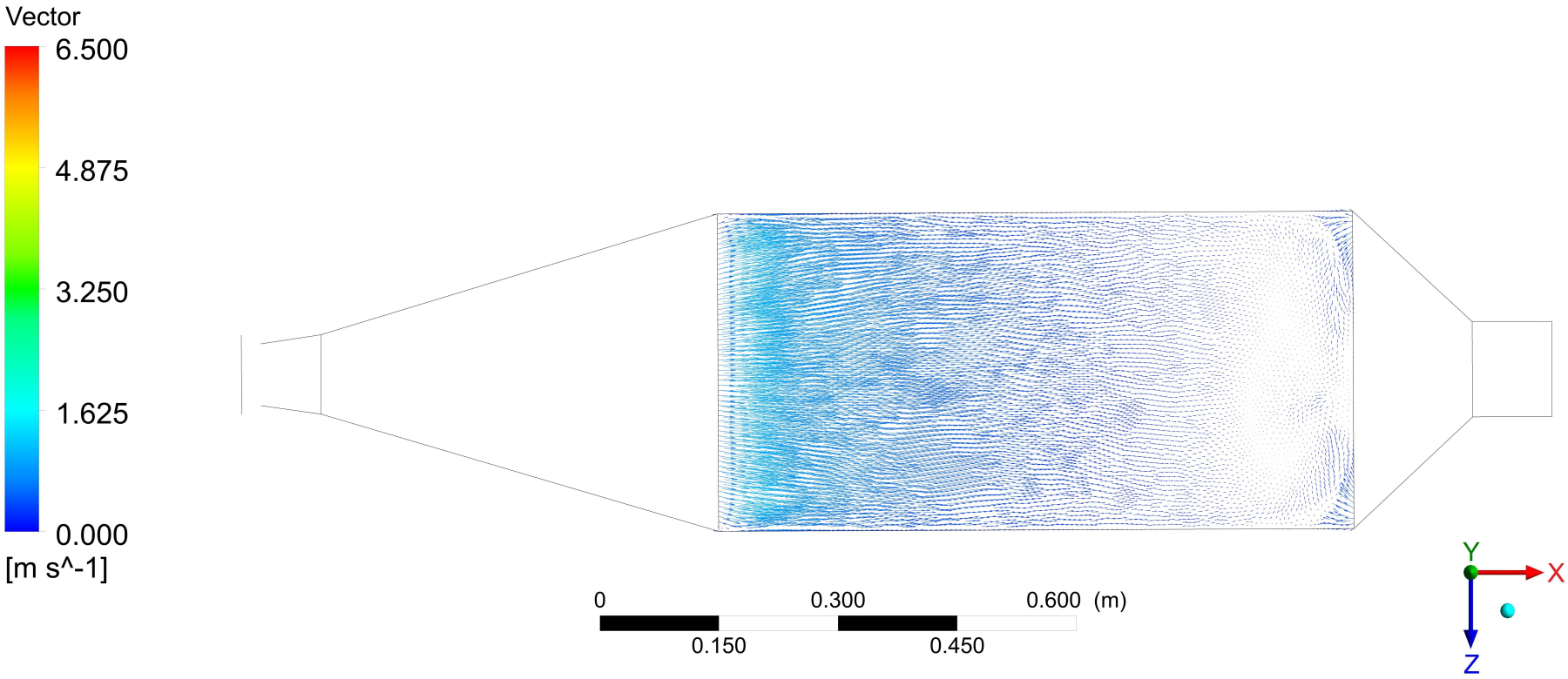
Vector
6.500
4.875
3.250
1.625
0.000
[m s^-1]
0
0.300
0.600 (m)
0.150
0.450
Y
X
Z

(b) vel = 0.2 $m\ s^{-1}$

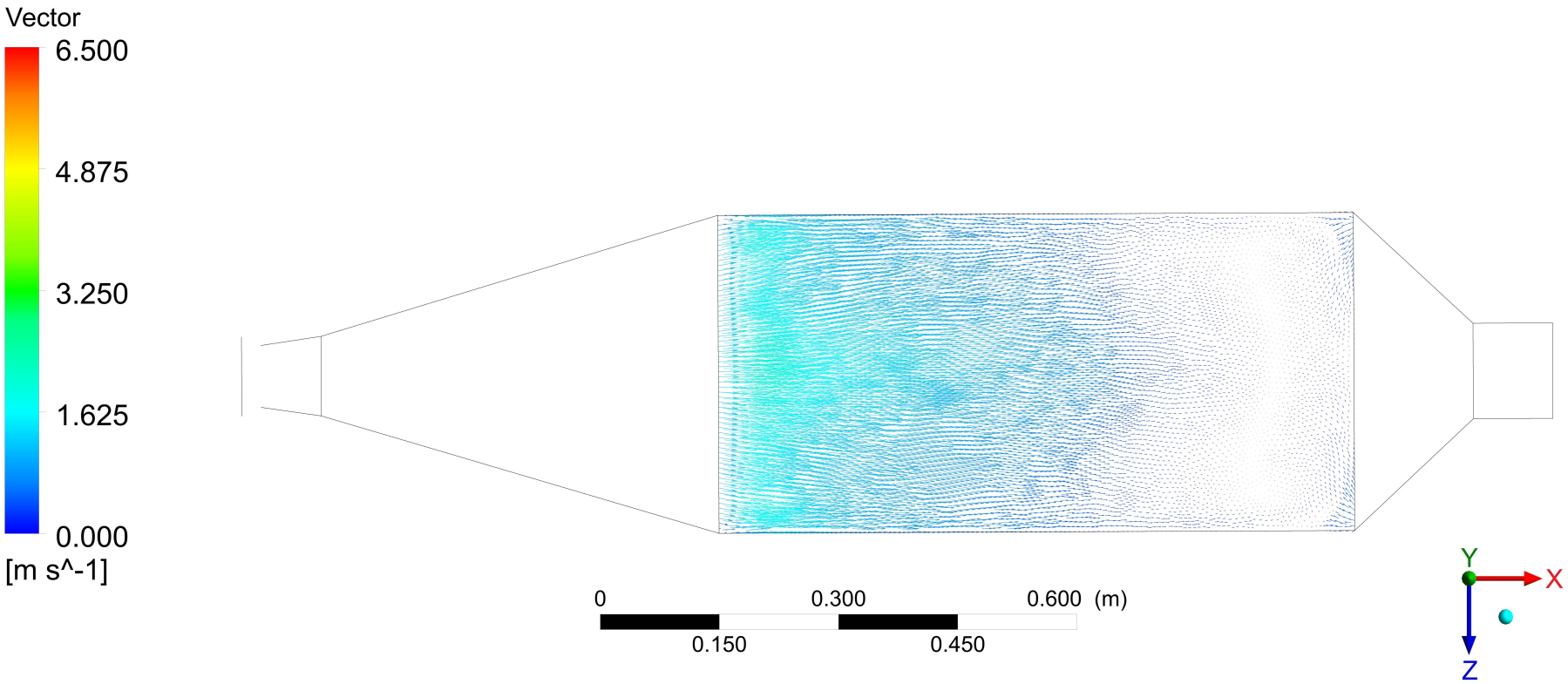

(c) vel = 0.3 $m\ s^{-1}$

Figure 28: Tunnel's upper view of vectors for (a) vel = 0.1 $m\ s^{-1}$, (b) vel = 0.2 $m\ s^{-1}$ and (c) vel = 0.3 $m\ s^{-1}$.

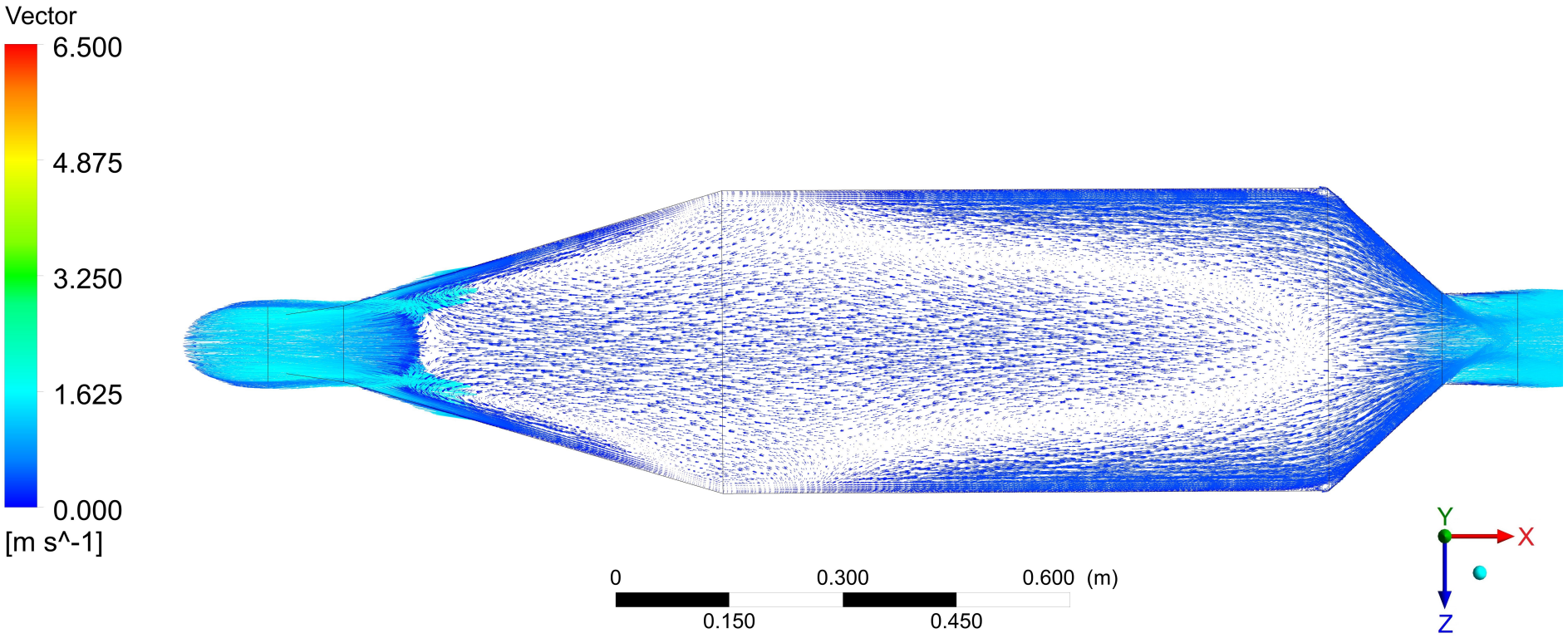
Vector
6.500
4.875
3.250
1.625
0.000
[m s^-1]
0
0.300
0.600 (m)
0.150
0.450
Y
X
Z

(a) vel = 0.1 $m\ s^{-1}$

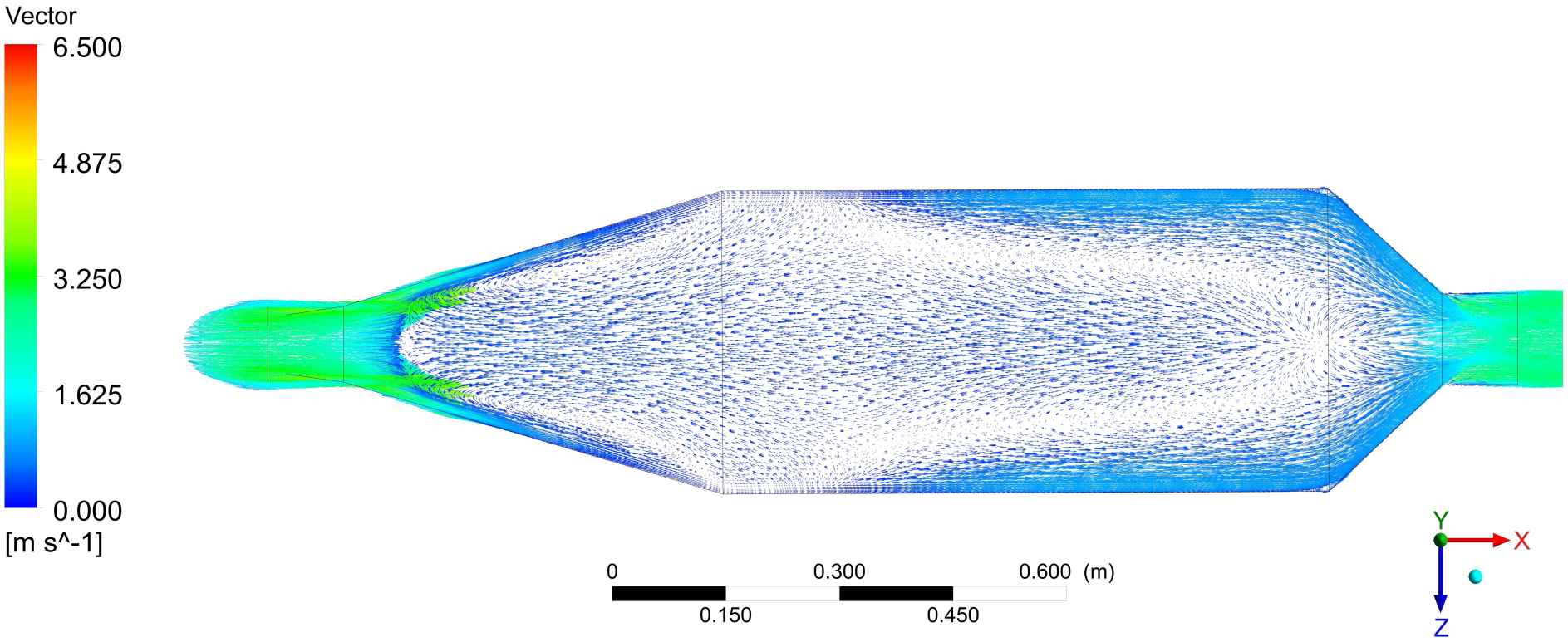
Vector
6.500
4.875
3.250
1.625
0.000
[m s^-1]
0
0.300
0.600 (m)
0.150
0.450
Y
X
Z

(b) vel = 0.2 $m\ s^{-1}$

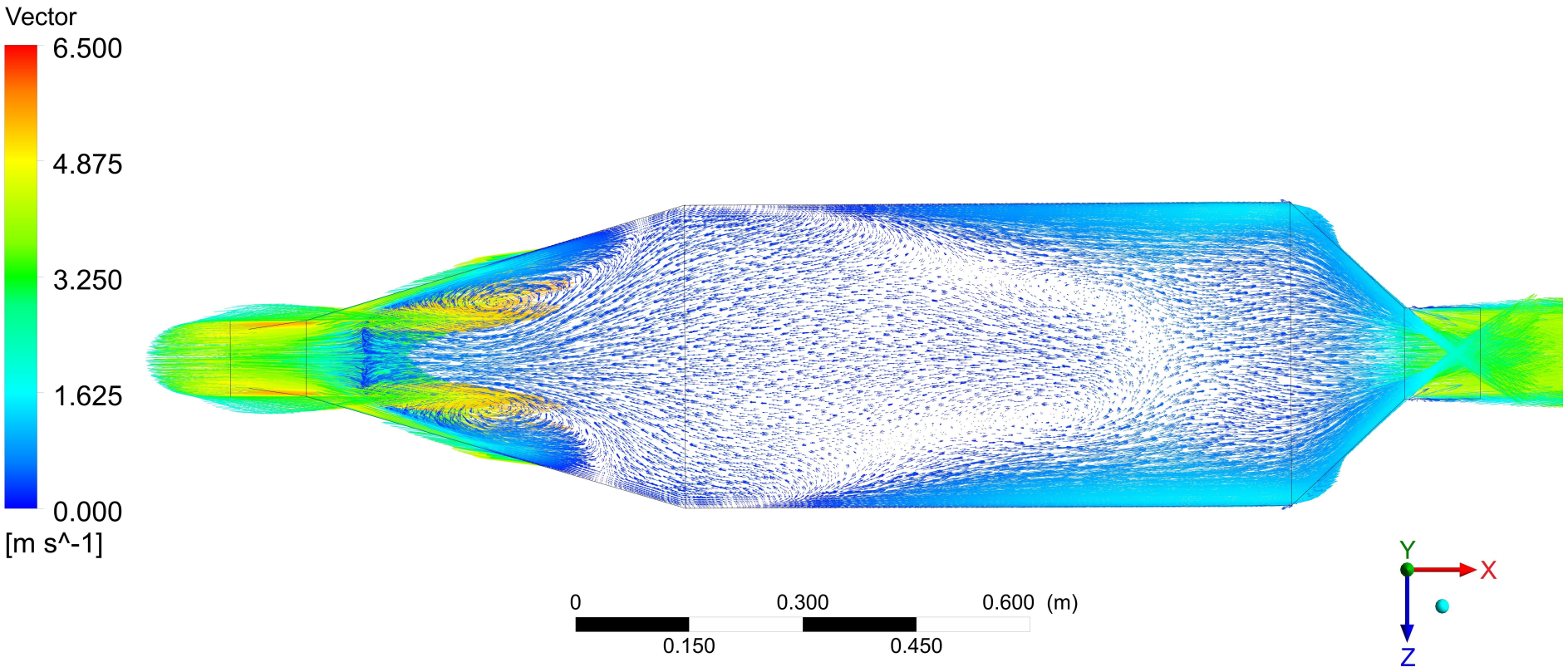

(c) vel = 0.3 $m\ s^{-1}$

Figure 29: Tunnel's upper view of vectors for (a) vel = 0.1 $m\ s^{-1}$, (b) vel = 0.2 $m\ s^{-1}$ and (c) vel = 0.3 $m\ s^{-1}$.

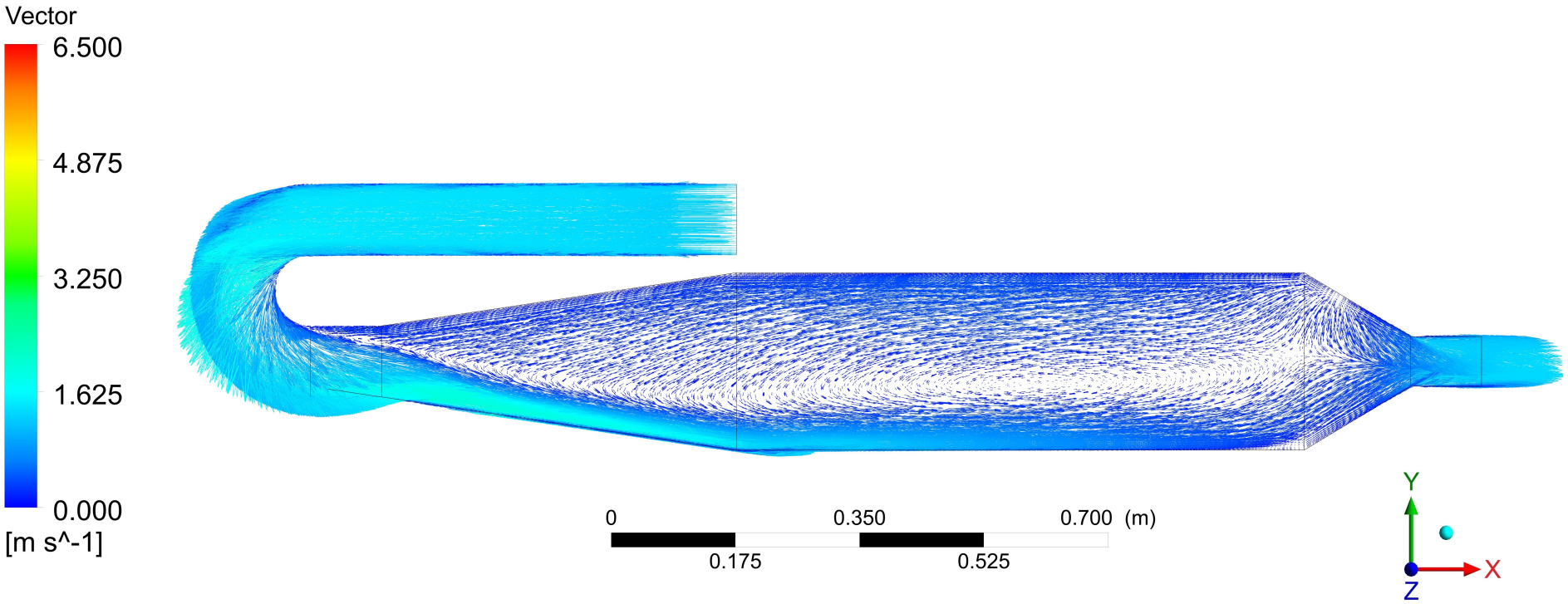
Vector
6.500
4.875
3.250
1.625
0.000
[m s^-1]
0
0.350
0.700 (m)
0.175
0.525
Y
X
Z

(a) vel = 0.1 $m\ s^{-1}$

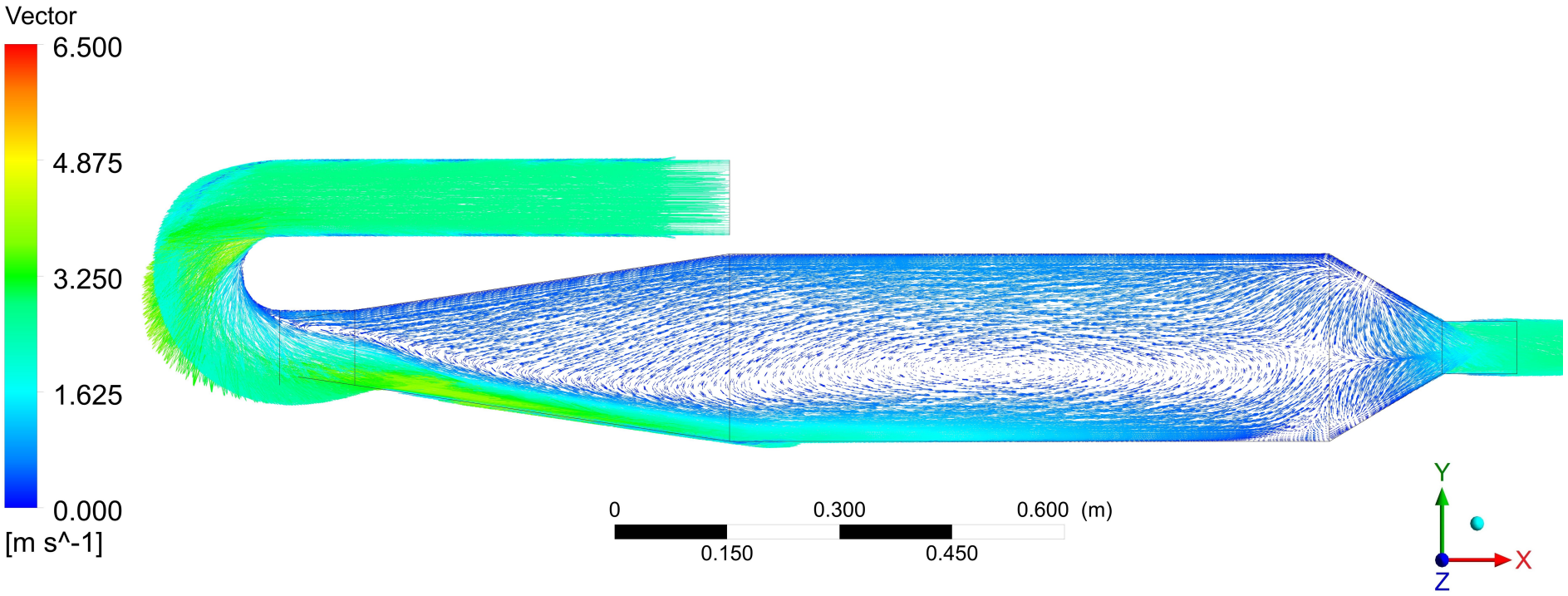
Vector
6.500
4.875
3.250
1.625
0.000
[m s^-1]
0
0.300
0.600 (m)
0.150
0.450
Y
X
Z

(b) vel = 0.2 $m\ s^{-1}$

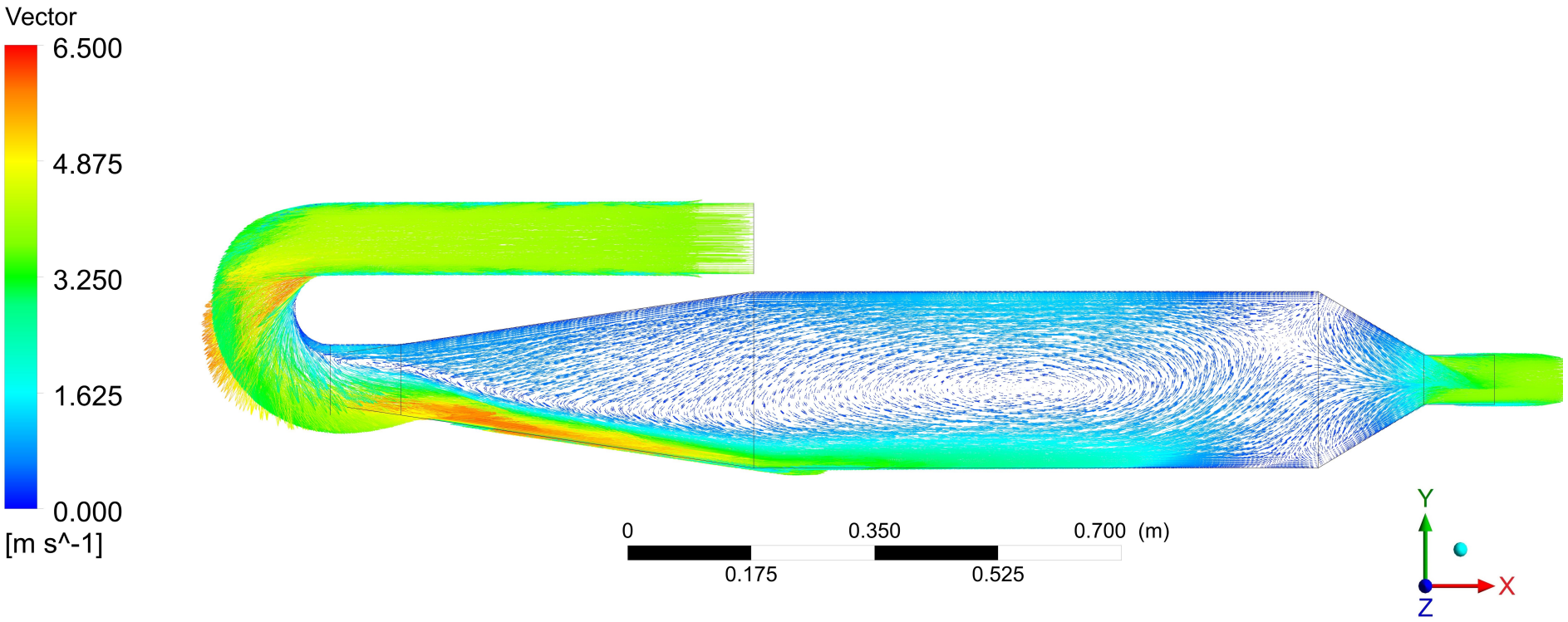

(c) vel = 0.3 $m\ s^{-1}$

Figure 30: Tunnel's side view of vectors for (a) vel = 0.1 $m\ s^{-1}$, (b) vel = 0.2 $m\ s^{-1}$ and (c) vel = 0.3 $m\ s^{-1}$.

Figure 32 shows the velocity vectors and the friction velocity at the bottom surface of the tunnel. The friction velocity values found for these velocities are shown in Table 6. Just to remember, the uniform inlet velocities of 1.27, 2.55 and 3.82 $m\ s^{-1}$ correspond to the mean velocities of 0.1, 0.2 and 0.3 $m\ s^{-1}$ in the main section of the tunnel, respectively.

Table 6 – Friction velocity values for different inlet velocities.

Mean velocity ($m\ s^{-1}$)	**Friction velocity** ($m\ s^{-1}$)
u = 0.1	$\overline{u^*}$ = 0.06
u = 0.2	$\overline{u^*}$ = 0.10
u = 0.3	$\overline{u^*}$ = 0.14

Figure 31 shows the friction velocity values found for wind speeds (U_{10}) measured at the height Z = 10 m. The experimental data obtained by VIERS-1 Delft experiment (VAN HALSEMA et al., 1989) (identified as green diamonds) are compared against the modeled data obtained by Caulliez, Makin and Kudryavtsev (2008) (identified as red triangles), Grare et al. (2013) (identified as blue squares), and the combined approach (a model proposed by Prata Jr. et al. (2017) to estimate the friction velocities - identified as hollow circles). Comparing these data presented in Figure 31 with the friction velocities presented in Table 6, it is possible to see that the values found using the wind tunnel (varying between 0.06 and 0.14 $m\ s^{-1}$) represent a range of the values found in atmospheric flows. Therefore, the wind tunnel reproduces a range of the friction velocity found in atmospheric flows, but there is still a wide range of it (from 0.15 to 0.7 $m\ s^{-1}$, approximately) that may occur in natural conditions and will not be represented by the wind tunnel.

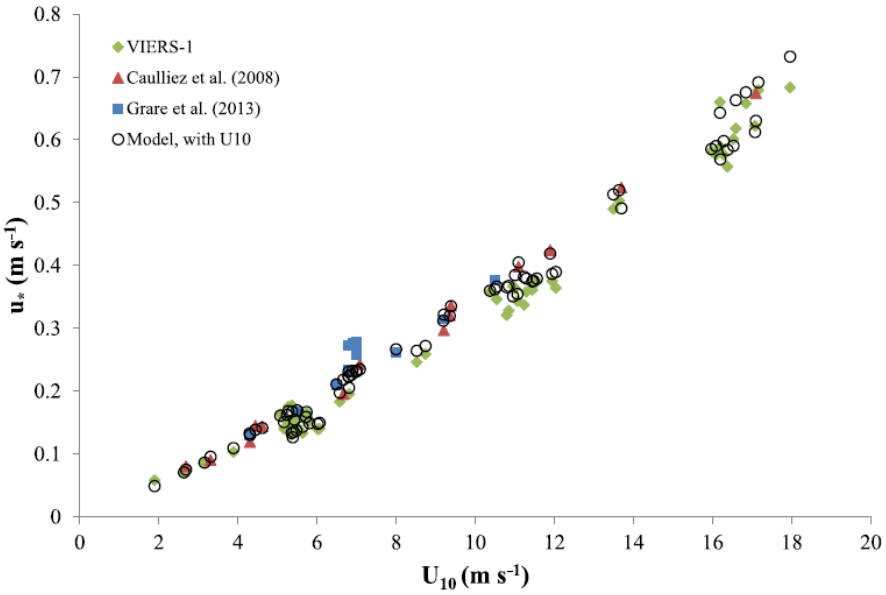

Figure 31: Comparison of the friction velocities estimated against experimental results from wind-wave tanks. From Prata Jr. et al. (2017).

The velocity vectors show the big recirculation in the main section as noticed before in Figure 30. The distribution of the friction velocity over the emitting surface is similar for all three velocities. The same behavior observed for the different roughness values can be observed here, that is, at the beginning of the main section, the friction velocity is higher than at the end, as the flow develops through the tunnel's length. It is also observed that the friction velocities increase along with the increase of the inlet velocity. For the inlet velocity of 1.27 $m\ s^{-1}$, the distribution of the friction velocity is concentrated at the center of the bottom surface.

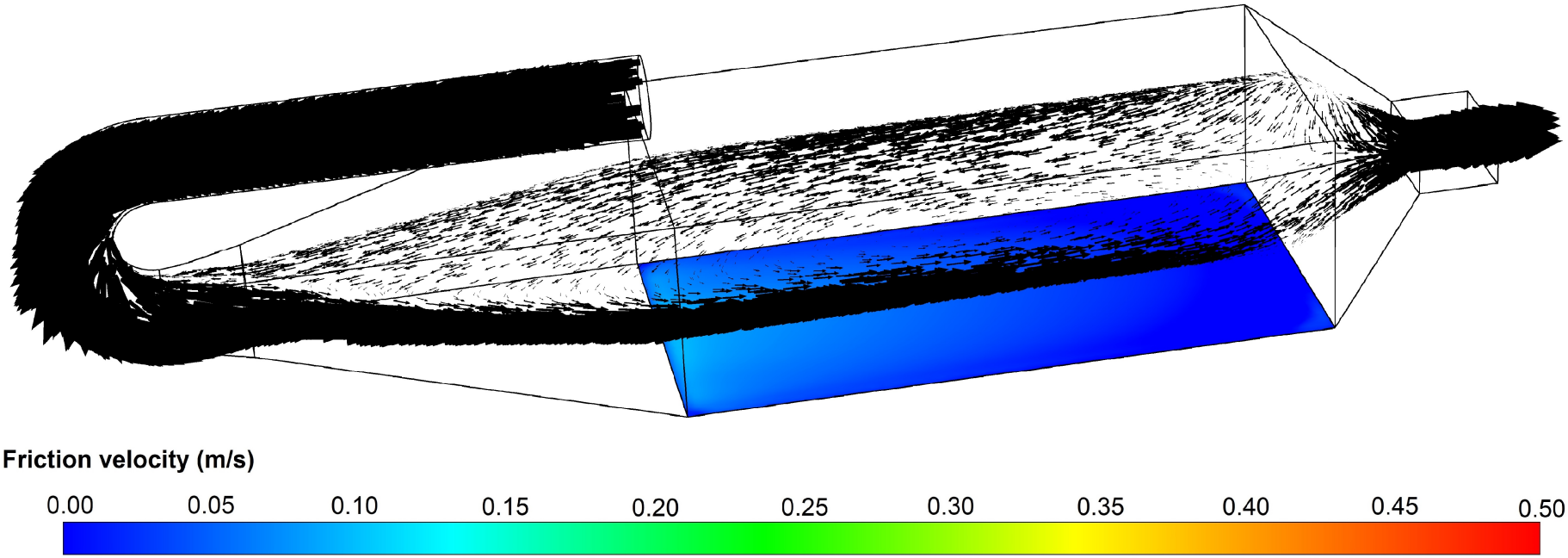
Friction velocity (m/s)
0.00
0.05
0.10
0.15
0.20
0.25
0.30
0.35
0.40
0.45
0.50

(a) vel = 0.1 $m\ s^{-1}$

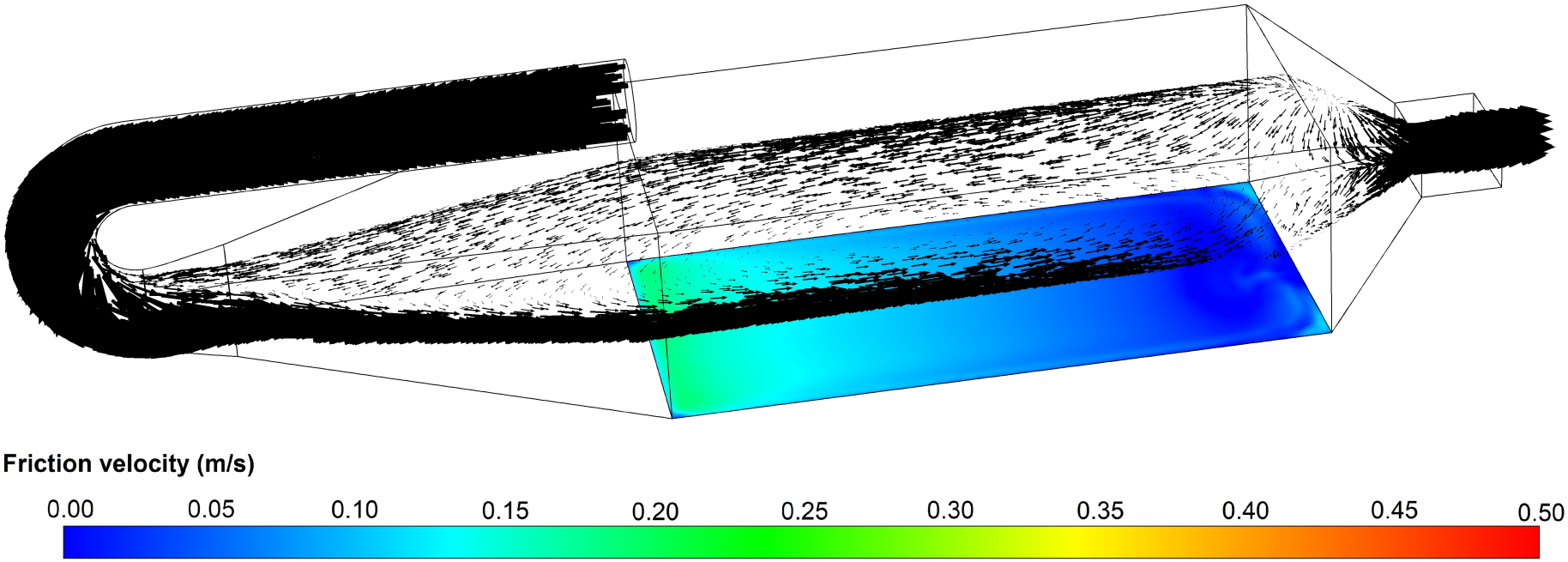
Friction velocity (m/s)
0.00
0.05
0.10
0.15
0.20
0.25
0.30
0.35
0.40
0.45
0.50

(b) vel = 0.2 $m\ s^{-1}$

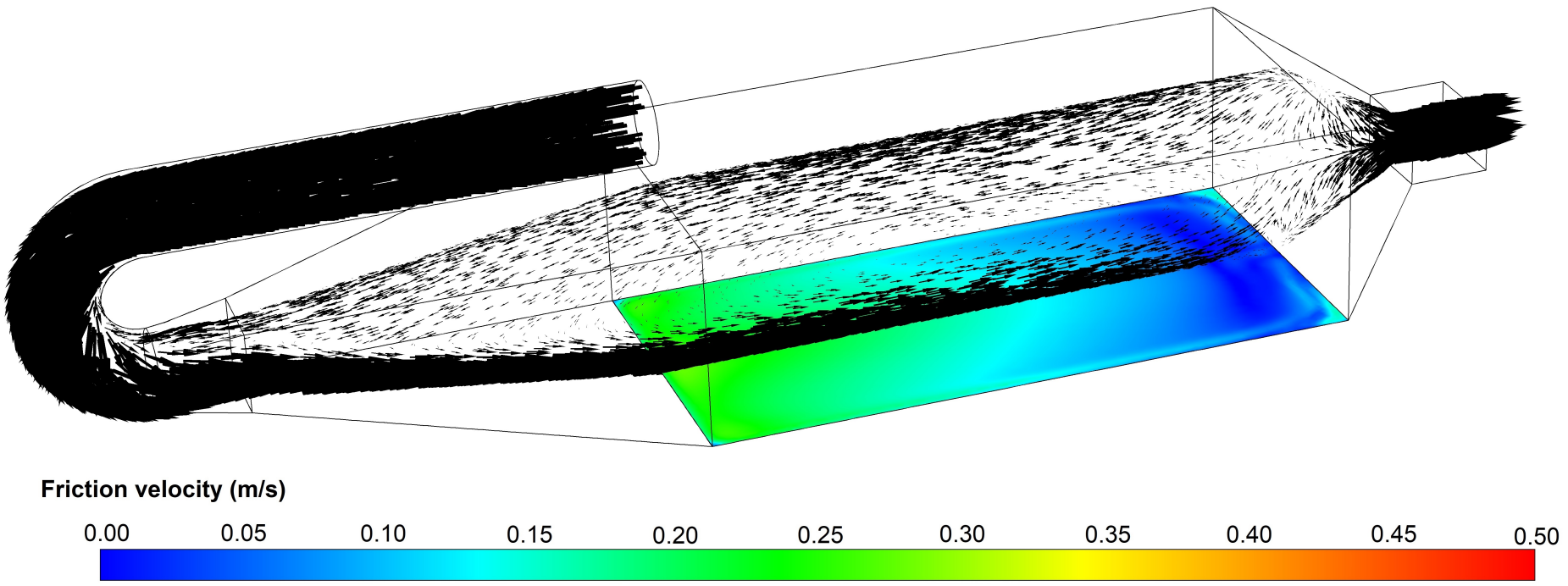

(c) vel = 0.3 $m\ s^{-1}$

Figure 32: Velocity vectors and friction velocity at the tunnel's bottom surface for (a) vel = 0.1 $m\ s^{-1}$, (b) vel = 0.2 $m\ s^{-1}$ and (c) vel = 0.3 $m\ s^{-1}$.

The turbulent kinetic energy is presented in planes at the positions $x = 0.2\ m$, $x = 0.4\ m$ and $x = 0.6\ m$ in the main section of the tunnel (Figure 33). In this case, the TKE is directly related to the inlet velocity: the lower the velocity, the less intense is the TKE. The turbulence intensity for the inlet velocity of 1.27 $m\ s^{-1}$ is very close to zero. The dissipation of the turbulence still occurs due to friction, however, once the inlet velocity is lower, the intensity of the TKE is also lower, as the dissipation.

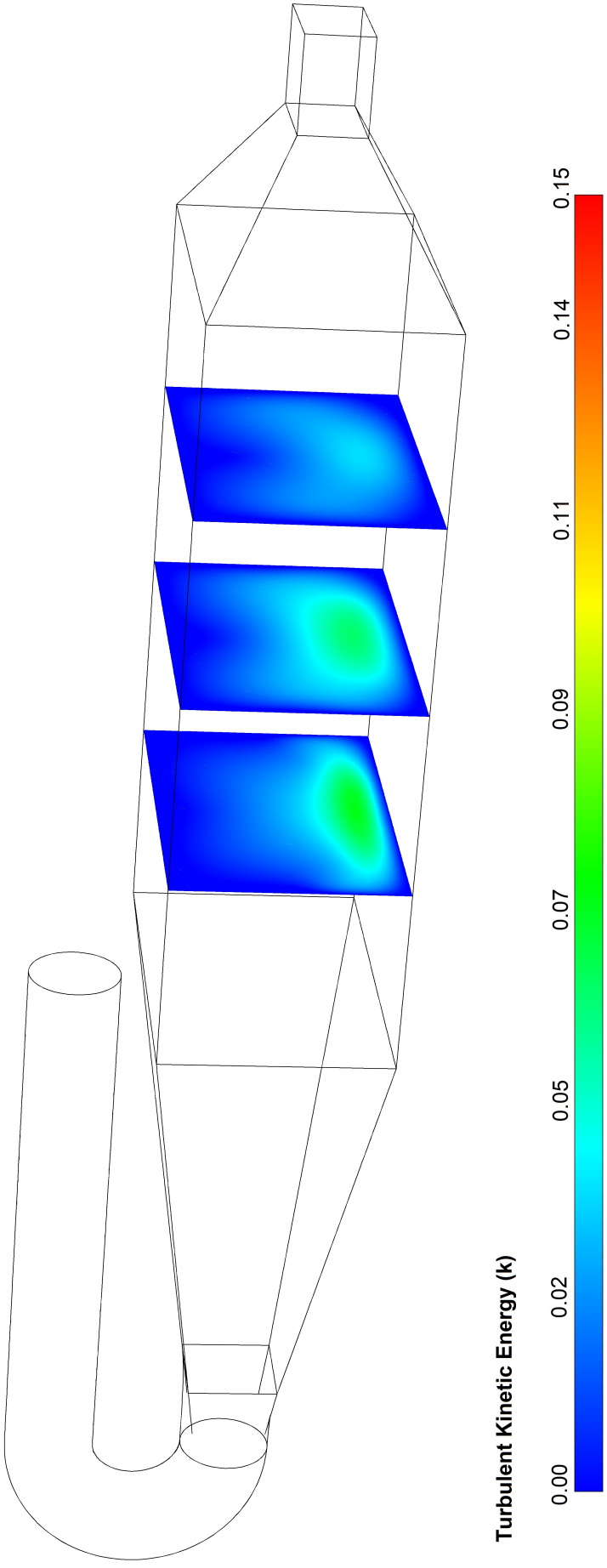

(a) vel = 0.1 $m\ s^{-1}$

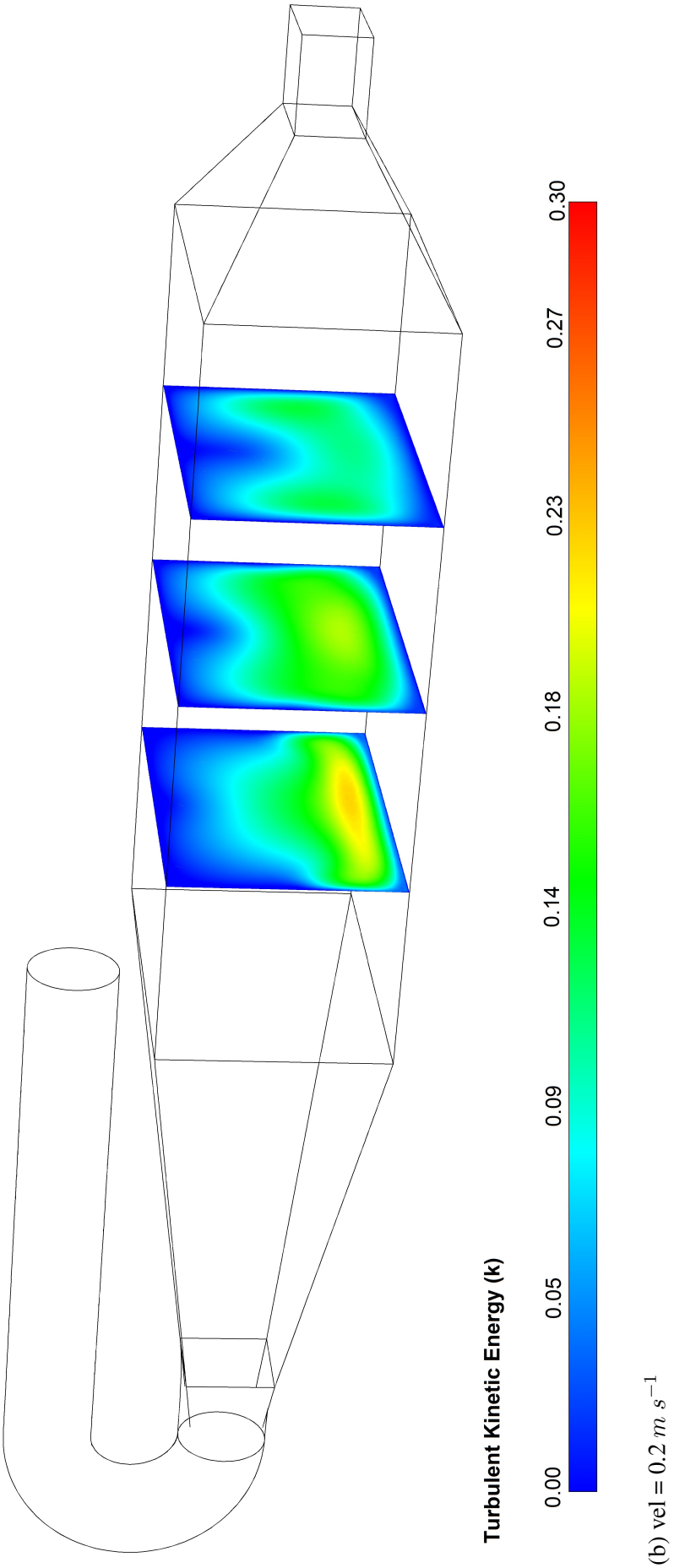

(b) vel = 0.2 $m\ s^{-1}$

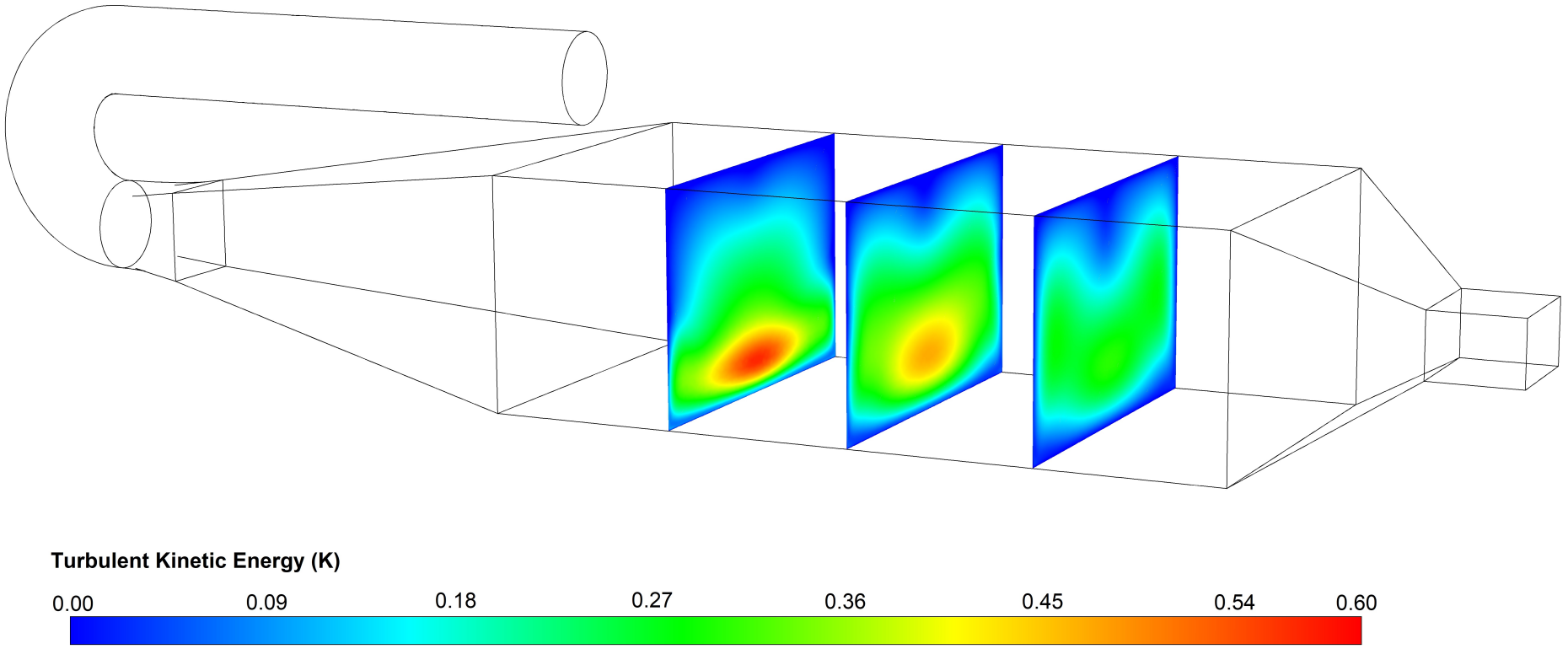

(c) vel = 0.3 $m\ s^{-1}$

Figure 33: Turbulent kinetic energy at positions $x = 0.2\ m$, $x = 0.4\ m$ and $x = 0.6\ m$ for (a) vel = 0.1 $m\ s^{-1}$, (b) vel = 0.2 $m\ s^{-1}$ and (c) vel = 0.3 $m\ s^{-1}$.

6 Conclusions and recommendations

6.1 Conclusions

The main objective of this work consists in investigating the air flow inside the portable wind tunnel developed by the UNSW. The numerical results showed various vortices inside the tunnel. This can be a good indication that the flow inside the tunnel is well mixed. However, an acceleration at the bottom surface after the inlet curve could cause an overestimation when measuring odor components; since higher flow velocities cause a low resistance to the mass transfer at the surface, consequently increasing the odor emission. So, further investigation is necessary to understand the volatilization process inside the tunnel.

According to the results, the smother the surface, the longer and with less intensity are the vortices inside the tunnel. A different behavior is seen with turbulence intensity; the smother the surface, the more intense the turbulence gets. Considering the non-homogeneity characteristic of the friction velocities found in atmospheric flows, comparing it with the data found using the wind tunnel might not be the best approach. The friction velocities found using the wind tunnel are mean and constant values and they may not fully represent the friction velocities of atmospheric flows. When analyzing the different inlet velocities and their respective friction velocities, it was noticed that it only represents a small range of the friction velocities found in atmospheric flows. Therefore, the wind tunnel might reproduce some of the conditions found in atmospheric flows, but not all of them. The comparison of the data obtained by an enclosure device with the real emission that occurs in the open field involves several factors that might differ. For liquid compounds, things like waves and currents in the water will certainly differ among the enclosure device and the open field. These conditions happen all the time and cannot be controlled at the source in the open field and will interfere in the emission rate of the compounds. Currently, The enclosure device is not capable of fully reproducing these conditions.

6.2 Recommendations for future works

- Performing experimental work with detail velocity and turbulence measurements in order to allow validation of numerical simulations.
- Analyzing different wind tunnel configurations in order to eliminate the acceleration caused by the inlet curve.
- Studying the volatilization of odorous compounds using the wind tunnel for comparison with results from theoretical models for odor emissions.

- Conducting numerical simulation of the fluid flow inside the wind tunnel using other turbulence models than RANS models.

References

ANDREÃO, W. L. *Análise da influência do escoamento no interior de uma câmara de fluxo dinâmica na taxa de emissão de sulfeto de hidrogênio*. Dissertation (Master) — Universidade Federal do Espírito Santo, 2016.

ANDREÃO, W. L. et al. Effects of flux chamber configuration on the sampling of odorous gases emissions. *International Journal of Heat and Mass Transfer*, v. 140, p. 918 – 930, 2019.

ANSYS. Ansys fluent user's guide. Release 19.1, 2019.

ARGAÍN, J. L.; MIRANDA, P. M. A.; TEIXEIRA, M. A. C. Estimation of the friction velocity in stably stratified boundary-layer flows over hills. *Boundary-Layer Meteorology*, v. 130, n. 1, p. 15–28, 2009.

BALSARI, P. et al. Ammonia emissions from farmyard manure heaps and slurry stores—effect of environmental conditions and measuring methods. *Biosystems Engineering*, v. 97, n. 4, p. 456 – 463, 2007. Gaseous emissions from Agricultural Systems.

BLISS, P. J.; JIANG, K.; SCHULZ, T. J. The development of a sampling system for the determination of odor emission rates from areal surfaces: Part ii. mathematical model. *Journal of the Air & Waste Management Association*, Taylor & Francis, v. 45, n. 12, p. 989–994, 1995.

CAPELLI, L. et al. Validation of a method for odor sampling on solid area sources. *Water Science and Technology*, IWA Publishing, v. 66, n. 8, p. 1607–1613, 2012.

CAPELLI, L.; SIRONI, S.; ROSSO, R. D. Odor sampling: Techniques and strategies for the estimation of odor emission rates from different source types. *Sensors*, v. 13, n. 1, p. 938–955, 2013b.

CAPELLI, L. et al. A comparative and critical evaluation of odour assessment methods on a landfill site. *Atmospheric Environment*, v. 42, n. 30, p. 7050 – 7058, 2008b.

CAPELLI, L. et al. Design and validation of a wind tunnel system for odour sampling on liquid area sources. *Water Science and Technology*, IWA Publishing, v. 59, n. 8, p. 1611–1620, 2009b.

CAULLIEZ, G.; MAKIN, V.; KUDRYAVTSEV, V. Drag of the water surface at very short fetches: observations and modeling. *J. Phys. Oceanogr.*, v. 38, p. 2038–2055, 2008.

COPPIN, P. A.; BRADLEY, E. F.; FINNIGAN, J. J. Measurements of flow over an elongated ridge and its thermal stability dependence: The mean field. *Boundary-Layer Meteorology*, v. 69, n. 1, p. 173–199, 1994.

DAVIDSON, P. A. Turbulence: An introduction for scientists and engineers. Oxford University Press, 2009.

EKLUND, B. Practical guidance for flux chamber measurements of fugitive volatile organic emission rates. *Journal of the Air & Waste Management Association*, Taylor & Francis, v. 42, n. 12, p. 1583–1591, 1992.

EL-FADEL, M.; FINDIKAKIS, A. N.; LECKIE, J. O. Environmental impacts of solid waste landfilling. *Journal of Environmental Management*, v. 50, n. 1, p. 1 – 25, 1997.

FERZIGER, J. H.; PERIC, M. Computational methods for fluid dynamics. Springer Berlin Heidelberg, 2001.

GALVIN, G. et al. The effect of loading rate on odour emissions from anaerobic effluent ponds in souht-east Queensland. *Proceedings of 4th Queensland environmental conference "Environmental solutions - meeting the challenge in 2002"*, p. 77–82, 2002.

GHOLSON, A. R. et al. Evaluation of an enclosure method for measuring emissions of volatile organic compounds from quiescent liquid surfaces. *Environmental Science & Technology*, v. 25, n. 3, p. 519–524, 1991.

GOSTELOW, P. *The modelling of odours from sewage treatment works*. Thesis (PhD) — Cranfiel Univerty, 2002.

GOSTELOW, P. et al. Sampling for the measurement of odours. *Scientific and Technical Report*, IWA Publishing, n. 17, 2003.

GOSTELOW, P.; PARSONS, S.; STUETZ, R. Odour measurements for sewage treatment works. *Water Research*, v. 35, n. 3, p. 579 – 597, 2001.

GRARE, L. et al. Growth and dissipation of wind-forced, deep-water waves. *J. Fluid Mech.*, n. 722, p. 5–50, 2013.

HUDSON, N.; AYOKO, G. Odour sampling 1: Physical chemistry considerations. *Bioresource Technology*, v. 99, n. 10, p. 3982 – 3992, 2008a.

HUDSON, N.; AYOKO, G. Odour sampling. 2. comparison of physical and aerodynamic characteristics of sampling devices: A review. *Bioresource Technology*, v. 99, n. 10, p. 3993 – 4007, 2008b.

HUDSON, N.; AYOKO, G. Comparison of emission rate values for odour and odorous chemicals derived from two sampling devices. *Atmospheric Environment*, v. 43, n. 20, p. 3175 – 3181, 2009a.

HUDSON, N. et al. Comparison of odour emission rates measured from various sources using two sampling devices. *Bioresource Technology*, v. 100, n. 1, p. 118 – 124, 2009b.

JASAK, H. *Error analysis and estimation for the finite volume method with applications to fluid flows*. Thesis (PhD) — University of London, 1996.

JIANG, K. *A Developed and Improved Odour Sampling System*. Dissertation (Master) — University of New South Wales, 1993.

JIANG, K.; BLISS, P. J.; SCHULZ, T. J. The development of a sampling system for determining odor emission rates from areal surfaces: Part i. aerodynamic performance. *Journal of the Air & Waste Management Association*, Taylor & Francis, v. 45, n. 11, p. 917–922, 1995.

JIANG, K.; KAYE, R. Comparison study on portable wind tunnel system and isolation chamber for determination of vocs from areal sources. *Water Science and Technology*, v. 34, n. 3, p. 583 – 589, 1996.

KAPADIA, S. et al. Detached-eddy simulation over a reference ahmed car model. Springer Netherlands, Dordrecht, p. 481–488, 2004.

LAOR, Y.; PARKER, D.; PAGÉ, T. Measurement, prediction, and monitoring of odors in the environment: a critical review. *Reviews in Chemical Engineering*, De Gruyter, v. 30, p. 139–166, 2014.

LEWIS, W. K.; WHITMAN, W. G. Principles of gas absorption. *Industrial and Engineering Chemistry*, v. 16, n. 12, p. 1215–1220, 1924.

LINDVALL, T. On sensory evaluation of odorous air pollutant intensities. *Nordisk Hygienisk Tidskrift. Supplementum.*, Svenska Arbetsgwarefoereningen, v. 2, 1970.

LIU, Y. et al. Estimation of volatile compounds emission rates from the working face of a large anaerobic landfill in china using a wind tunnel system. *Atmospheric Environment*, v. 111, n. Supplement C, p. 213 – 221, 2015.

MARTINS, R. S. et al. Evaluating the flow inside of portable wind tunnels for odour measurements. *Chemical Engineering Transactions*, v. 68, p. 55 – 60, 2018.

MENTER, F. R. Performance of popular turbulence models for attached and separated adverse pressure gradient flow. *AIAA Journal*, v. 30, p. 2066 – 2072, 1992.

NAVARATNASAMY, M.; EDEOGU, I.; FEDDES, J. Comparison of a wind tunnel and vented flux chamber in measuring odour emission rates. *Canadian Biosystems Engineering*, v. 51, p. 6.1 – 6.8, 2009.

NIKURADSE, J. Laws of flow in rough pipes. In VDI Forschungsheft, 1933.

PARKER, D. et al. Standardization of flux chamber and wind tunnel flux measurements for quantifying volatile organic compound and ammonia emissions from area sources at animal feeding operations. *Atmospheric Environment*, v. 66, n. Supplement C, p. 72 – 83, 2013.

PARKER, T.; DOTTRIDGE, J.; KELLY, S. Investigation of the composition and emissions of trace components in landfill gas. *Environment Agency, Bristol, UK*, p. 146, 2002.

PERTA, E. S. di et al. Study of aerodynamic performances of different wind tunnel configurations and air inlet velocities, using computational fluid dynamics (cfd). *Computers and Electronics in Agriculture*, v. 125, n. Supplement C, p. 137 – 148, 2016.

POPE, S. B. Turbulent flows. Cambridge University Press, 2000.

PRATA JR., A. A. et al. Use of computational fluid dynamics in the analysis of a portable wind tunnel for sampling of odorous emissions at liquid surfaces. *Chemical Engineering Transactions*, The Italian Association of Chemical Engineering, v. 40, p. 145–150, 2014.

PRATA JR., A. A. et al. Wind friction parametrisation used in emission models for wastewater treatment plants: A critical review. *Water Research*, v. 124, p. 49–66, 2017.

PRATA JR., A. A. et al. A critical review on liquid-gas mass transfer models for estimating gaseous emissions from passive liquid surfaces in wastewater treatment plants. *Water Research*, v. 130, p. 388 – 406, 2018.

SANTOS, J. M. et al. An experimental determination of the H_2S overall mass transfer coefficient from quiescent surfaces at wastewater treatment plants. *Atmospheric Environment*, v. 60, n. Supplement C, p. 18 – 24, 2012.

SCHÄFER, M. Computational engineering - introduction to numerical methods. Springer-Verlag Berlin Heidelberg, 2006.

SCHIFFMAN, S. S.; WILLIAMS, C. M. Science of odor as a potential health issue. *Journal of environmental quality*, v. 34, p. 129–138, 2005.

SCHLICHTING, H. Boundary-layer theory. Mcgraw-Hill Book Company, 1979.

SCHMIDT, D. R.; BICUDO, J. R.; JANNI, K. *Determining odor emissions from manure surfaces using a wing tunnel*. 1999.

SEINFELD, J. H.; PANDIS, S. N. Atmospheric chemistry and physics: from air pollution to climate change. John Wiley & Sons, Inc.; Second edition, 2006.

SHAO, Y. Physics and modelling of wind erosion. Springer, 2008.

SMITH, R.; WATTS, P. Determination of odour emission rates from cattle feedlots: Part 1, a review. *Journal of Agricultural Engineering Research*, v. 57, n. 3, p. 145 – 155, 1994a.

VAN HALSEMA, D. et al. Progress report on the viers-1 project part 1: The delft wind/wave experiment: Experiment and first results (no. bcrs-89-24). BCRS, 1989.

VERSTEEG, H. K.; MALALASEKERA, W. An introduction to computational fluid dynamics: the finite volume method. Harlow: Pearson Education, 2007.

WANG, X.; JIANG, J.; KAYE, R. Improvement of a wind-tunnel sampling system for odour and vocs. *Water Science and Technology*, IWA Publishing, v. 44, n. 9, p. 71–77, 2001.

WILCOX, D. C. Turbulence Modelling for CFD. DCW Industries Inc., 1993b.

WU, W. *Evaluation of a wind tunnel for measurement of odour emission from area sources*. Dissertation (Master) — University of Manitoba, 2007.

A Appendix

To evaluate the sensitivity of the mesh, three meshes with different resolutions were selected to simulate the flow. The coarse mesh was made with 1,720,780 elements, the medium mesh with 3,525,668 elements and the fine mesh with 7,278,104 elements. Figures 34a, 34b and 34c show the coarse, medium and fine meshes, respectively.

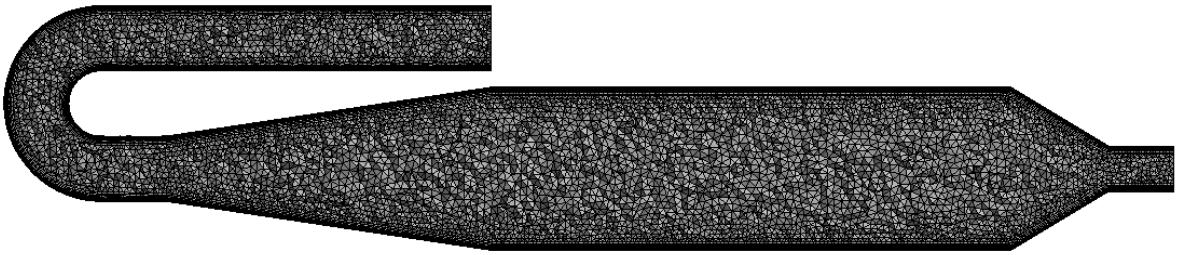

(a) Coarse mesh

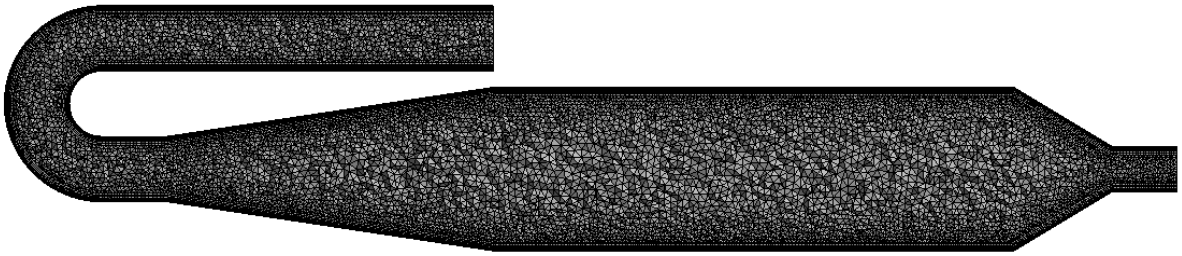

(b) Medium mesh

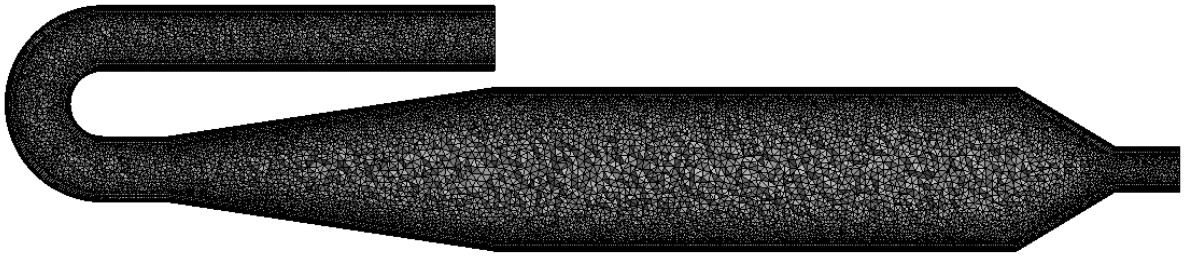

(c) Fine mesh

Figure 34: The coarse, medium and fine meshes

From one mesh to another, it was changed the size of the smallest element in the option *Face Sizing* (on *Meshing*). The influence of the different mesh sizes on the results were analyzed based on profiles of the velocity components (*u*, *v* and *w*), sampled on seven vertical lines inside the tunnel's main section (same positions as showed in Figure 18), and the friction velocity at the bottom surface of the tunnel.

Figure 35 shows the results of the friction velocity. The friction velocity value was 0.14 $m\ s^{-1}$ for all the three meshes. Figures from 36 to 42 show the graphics (velocity profiles)

comparing the meshes. It is possible to see that there was no significant modification on the results for the profiles obtained when the mesh in the study was more refined, so, the results could be considered independent of the mesh size. Thus, the coarse mesh was chosen to run the simulations because it takes less computational effort.

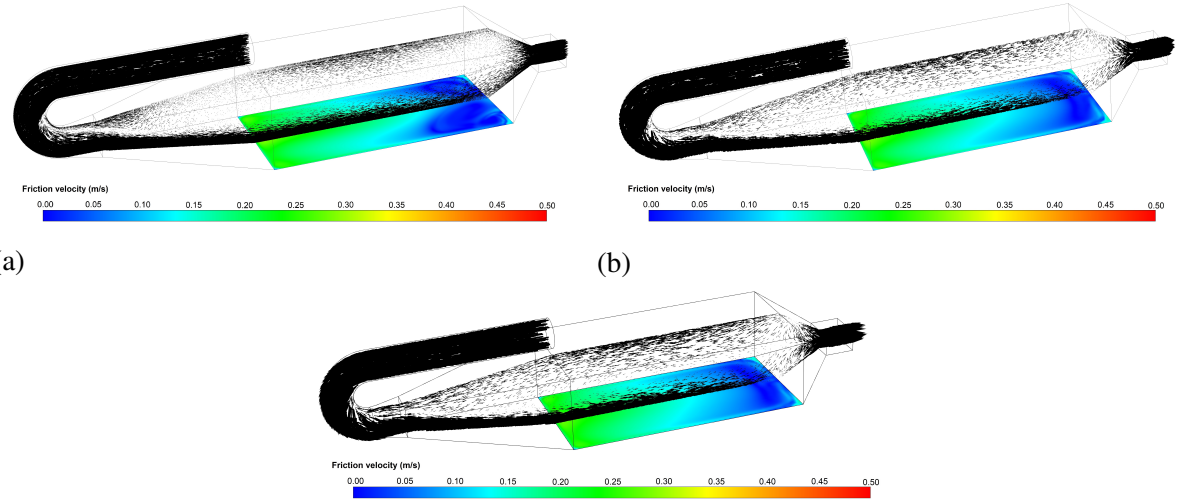

(a) (b)

(c)

Figure 35: Velocity vectors and friction velocity at the tunnel's bottom surface for (a) fine mesh, (b) medium mesh and (c) coarse mesh.

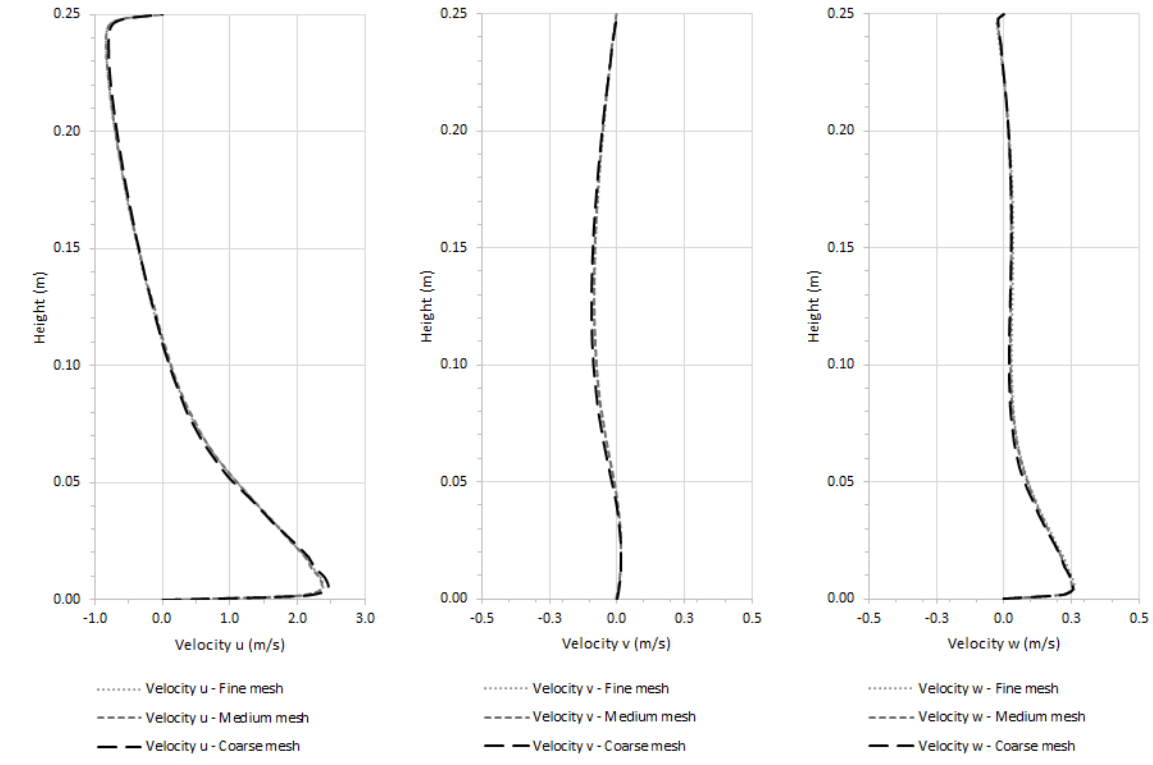

(a) (b) (c)

Figure 36: Velocity profile at position 1 (x = 0.2 m, z = 0.1 m).

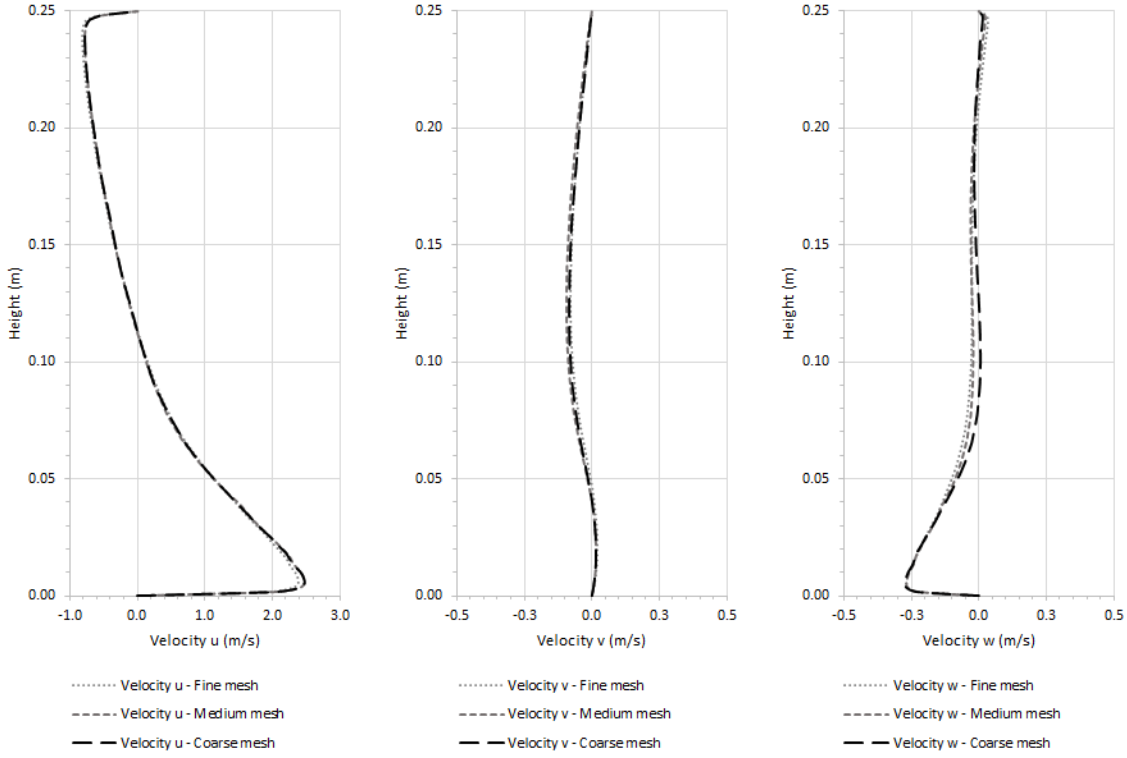

(a) (b) (c)

Figure 37: Velocity profile at position 2 (x = 0.2 m, z = 0.3 m).

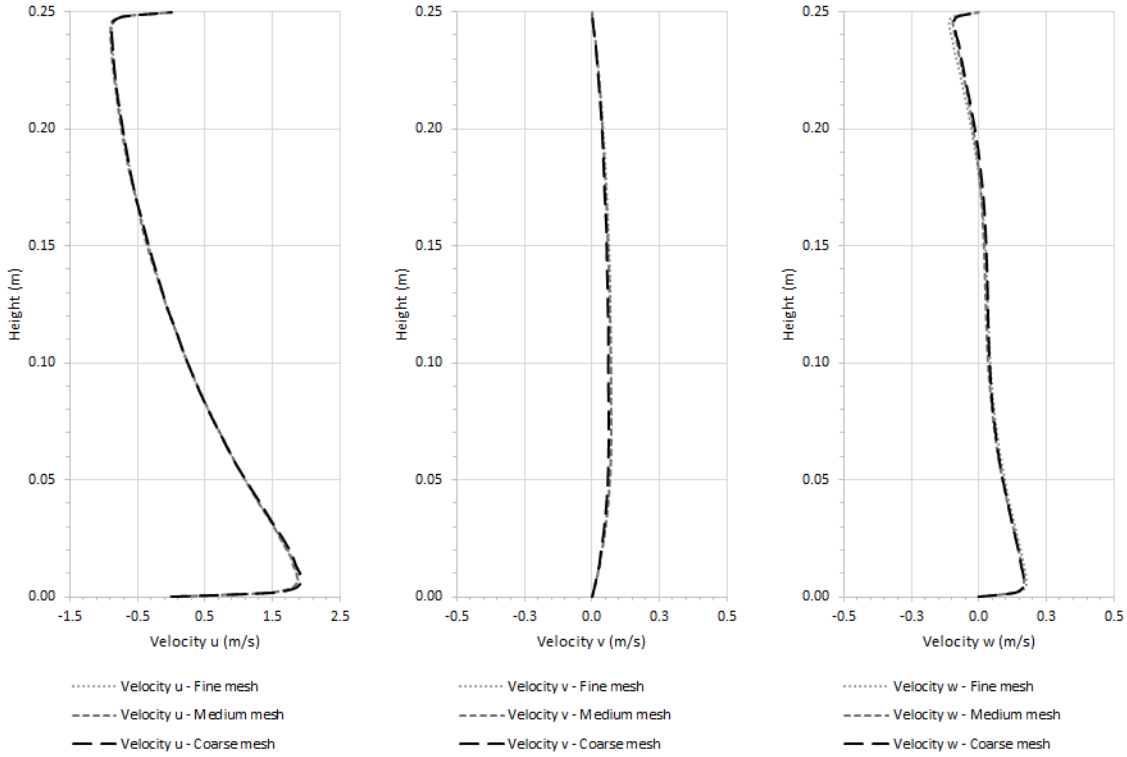

(a) (b) (c)

Figure 38: Velocity profile at position 3 (x = 0.4 m, z = 0.1 m).

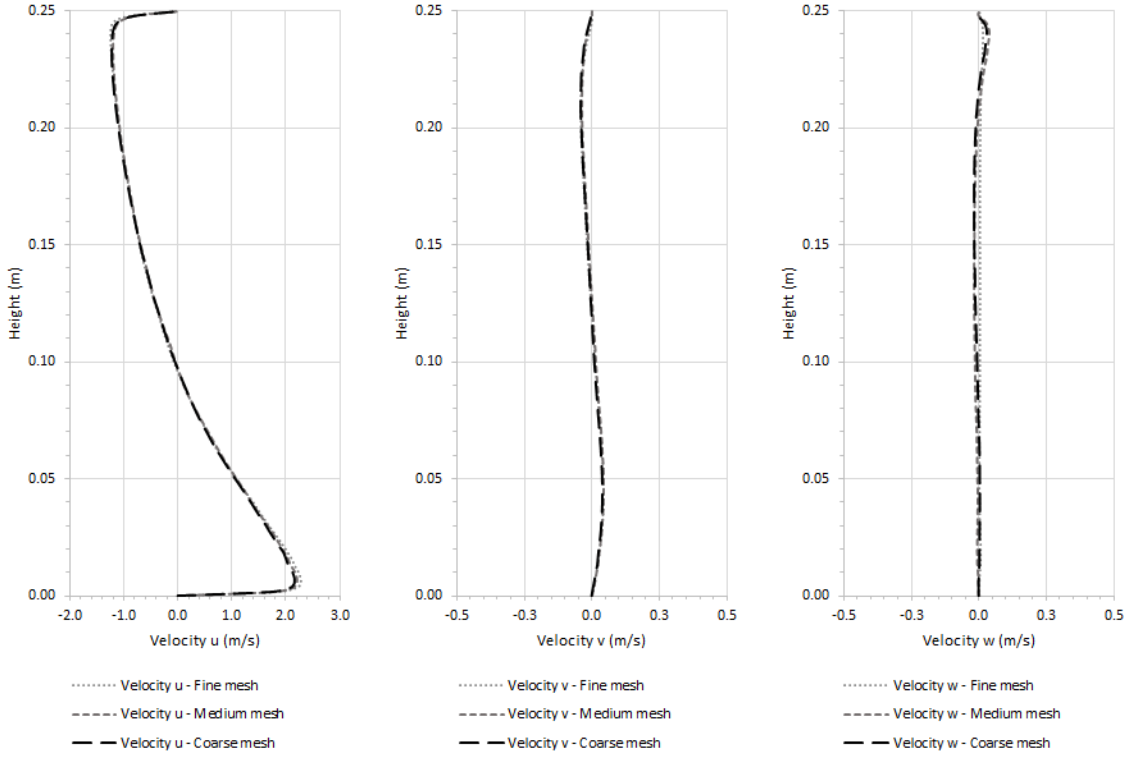

(a) (b) (c)

Figure 39: Velocity profile at position 4 (x = 0.4 m, z = 0.2 m).

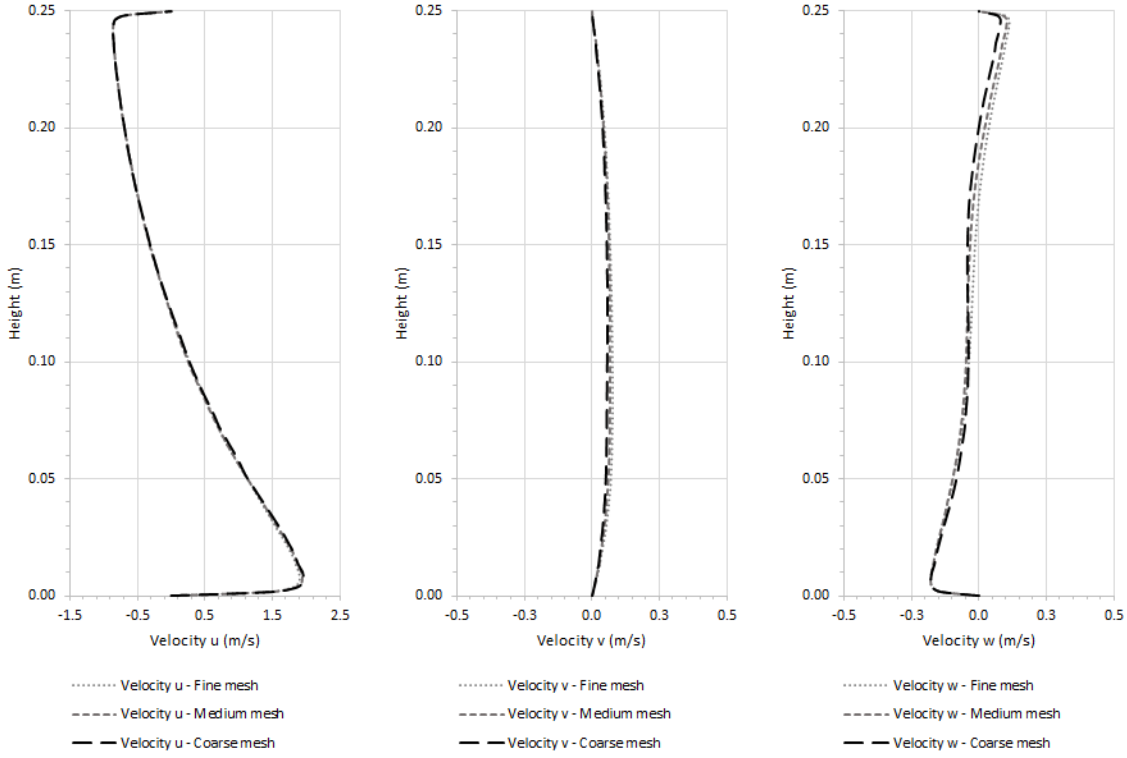

(a) (b) (c)

Figure 40: Velocity profile at position 5 (x = 0.4 m, z = 0.3 m).

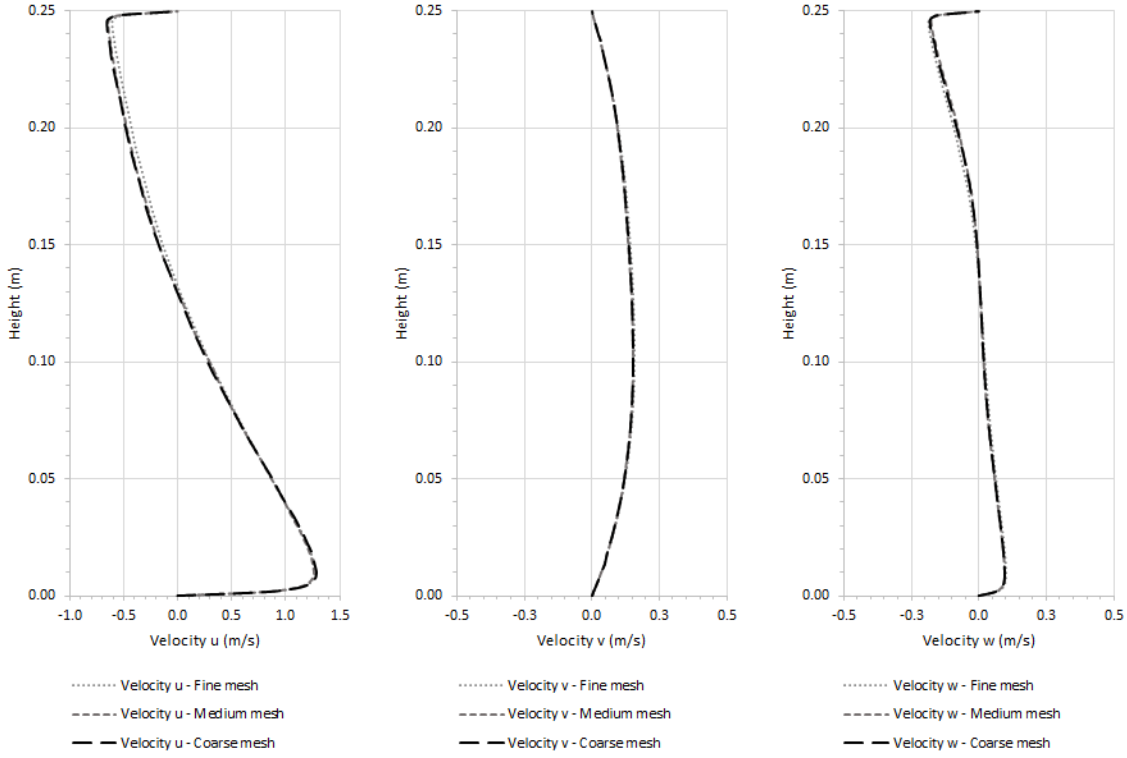

(a) (b) (c)

Figure 41: Velocity profile at position 6 (x = 0.6 m, z = 0.1 m).

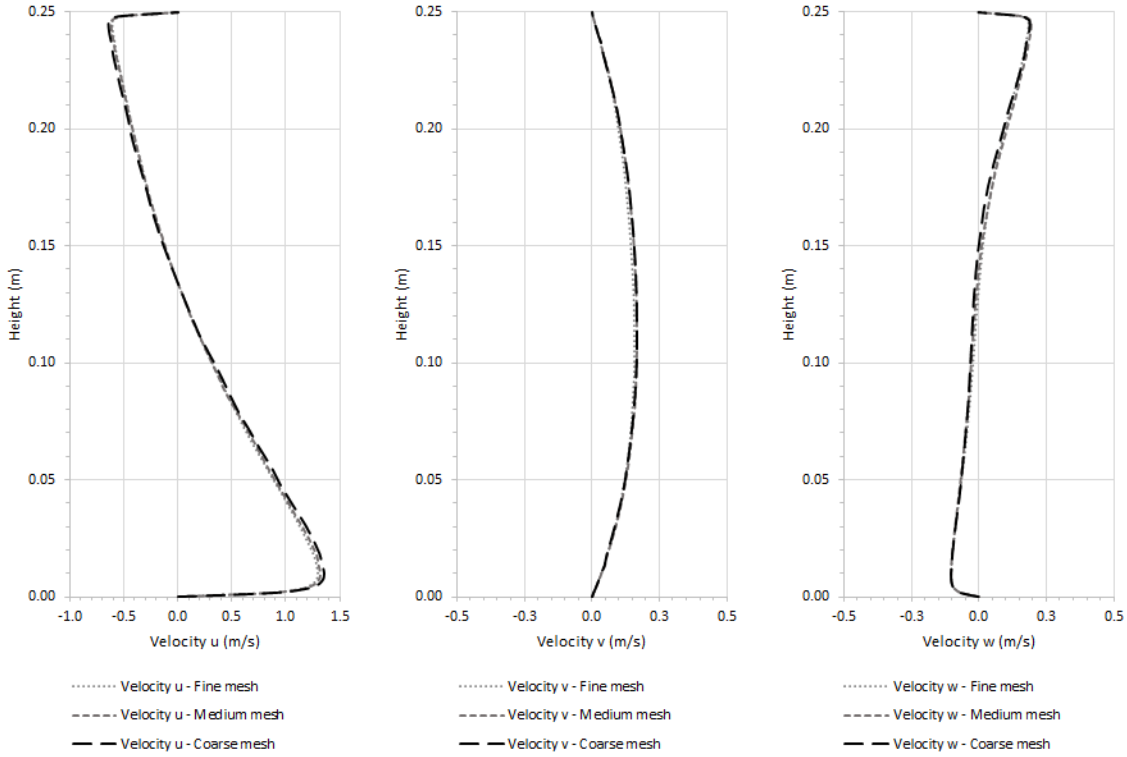

(a) (b) (c)

Figure 42: Velocity profile at position 7 (x = 0.6 m, z = 0.3 m).